The Abdus Salam
International Centre for Theoretical Physics

Minischool and Workshop on Mulitple Time Scale in the
Dynamics of the Nervous System
16 to 29 June 2008, ICTP, Trieste, Italy

VARIOUS BACKGROUND NOTES FOR TALK ON

"Fast and Slow Dynamics in Neural Networks with Small-World Connectivity"

by Prof. Sara SOLLA
Physiology, Dept. of Physics & Astronomy
Northwestern University, Chicago, U.S.A.

1) Self-Sustained Activity in a Small-World Network of Excitable Neurons

2) Multiple attractors, long chaotic transients, and failure in small-world networks of excitable neurons

3) Epilepsy in Small-World Networks

4) Topological Determinants of Epileptogenesis in Large-Scale Structural and Functional Models of the Dentate Gyrus Derived From Experimental Data

5) Internetwork and intranetwork communications during bursting dynamics: Applications to seizure prediction

SOLLA SARA
Background Information 1

Self-Sustained Activity in a Small-World Network of Excitable Neurons

Alex Roxin,[1,*] Hermann Riecke,[1] and Sara A. Solla[2]

[1]*Engineering Science and Applied Mathematics, Northwestern University, Evanston, Illinois 60208, USA*
[2]*Department of Physiology and Department of Physics and Astronomy, Northwestern University, Evanston, Illinois 60208, USA*

(Received 9 June 2003; revised manuscript received 17 February 2004; published 11 May 2004)

We study the dynamics of excitable integrate-and-fire neurons in a small-world network. At low densities p of directed random connections, a localized transient stimulus results either in self-sustained persistent activity or in a brief transient followed by failure. Averages over the quenched ensemble reveal that the probability of failure changes from 0 to 1 over a narrow range in p; this failure transition can be described analytically through an extension of an existing mean-field result. Exceedingly long transients emerge at higher densities p; their activity patterns are disordered, in contrast to the mostly periodic persistent patterns observed at low p. The times at which such patterns die out follow a stretched-exponential distribution, which depends sensitively on the propagation velocity of the excitation.

DOI: 10.1103/PhysRevLett.92.198101 PACS numbers: 87.18.Sn, 82.40.Bj, 89.75.Hc

Recent research in complex networks has provided increasing evidence for their relevance to a variety of physical, biological, and social phenomena [1–3]. Two distinct types of topology have been particularly useful in providing insights into the implications of complex connectivity: scale-free networks [3], characterized by the existence of a small number of hubs with high coordination number, and small-world networks [1], characterized by the presence of shortcuts that link two randomly chosen sites regardless of the distance between them.

So far, most work on complex networks has focused on their topological and geometrical properties; less attention has been given to the properties of dynamical systems defined on such networks. The interplay between the intrinsic dynamics of the constituent elements and their complex pattern of connectivity strongly affects the collective dynamics of the resulting system. For instance, the addition of shortcuts induces a finite-temperature phase transition even in the one-dimensional Ising model [4], and the introduction of unidirectional shortcuts can change the second-order phase transition in the two-dimensional Ising model into a first-order one [5]. In a system of coupled oscillatory elements, the introduction of shortcuts enhances synchronization [6], while the introduction of hubs eliminates the threshold for epidemic propagation [7].

The coexistence of shortcuts and regular local connections characteristic of small-world networks (SWNs) mimics a salient feature of the circuitry in the cortex [8–13], where experimental observations of excitatory traveling waves [11] provide evidence of some degree of local connectivity, while it is also recognized that long-range excitatory connections are present [10,12]. Our goal is to explore the influence of this complex connectivity on the dynamics of neuronal circuits; to this purpose, we choose a minimal model. The underlying network is modeled as a SWN with unidirectional shortcuts that reflect the nonreciprocal character of synaptic connections, and the excitable neurons are modeled as leaky integrate-and-fire units. We find that even this simple model exhibits a rich repertoire of distinct dynamical behaviors as a function of the density p of added shortcuts: a low p regime characterized by persistent periodic activity that is bistable with the quiescent state, a transition to failure with increasing p, followed by a reemergence of long-lasting disordered activity. We note that a SWN with unidirectional shortcuts has been considered in a different regime by Lago-Fernández *et al.* [14,15] to address the possibility of rapid synchronization among conductance-based neurons of the Hodgkin-Huxley type.

The model considered here consists of a one-dimensional array of N integrate-and-fire neurons (IFNs) in which a SWN topology is created through the addition of a density p of unidirectional long-range couplings. The membrane potential of the IFNs is determined by

$$\tau_m \frac{dV_i}{dt} = -V_i + I_{\text{ext}} + g_{\text{syn}} \sum_{j,m} w_{ij} \delta(t - t_j^{(m)} - \tau_D). \quad (1)$$

A neuron fires whenever its voltage exceeds 1; the voltage is then reset to 0. The external current is chosen to satisfy $I_{\text{ext}} < 1$; in this regime the IFNs are not oscillatory, but excitable. The last term models input currents due to presynaptic firing as a delayed impulse: if w_{ij} is nonzero, then neuron i receives a pulse input of amplitude g_{syn} with a delay τ_D after neuron j has fired its mth spike at time $t_j^{(m)}$. The synaptic conductance is chosen to satisfy $I_{\text{ext}} + g_{\text{syn}} > 1$, so that a single input suffices to sustain firing activity. The local connections are modeled here as nearest-neighbor couplings ($w_{i,i\pm1} = 1$) that define an underlying regular lattice. The long-range connections result from randomly *adding* rather than rerouting [1] a fixed fraction pN of unidirectional couplings $w_{ij} = 1$ to generate a SWN topology.

At $p = 0$, any excitation sufficient to cause a neuron to fire will generate two pulses that propagate through the

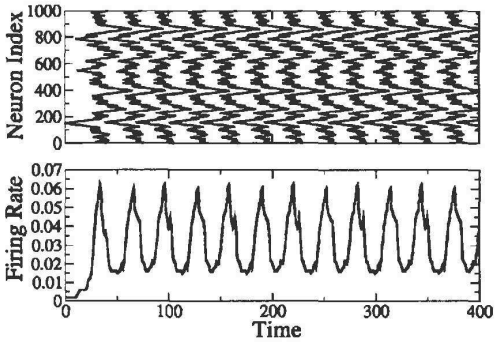

FIG. 1. Raster plot (top) and instantaneous firing rate (bottom) for a system with $N = 1000$, $I_{ext} = 0.85$, $g_{syn} = 0.2$, $\tau_m = 10$, $\tau_D = 1$, $p = 0.1$. Same parameter values are used in subsequent figures unless noted otherwise.

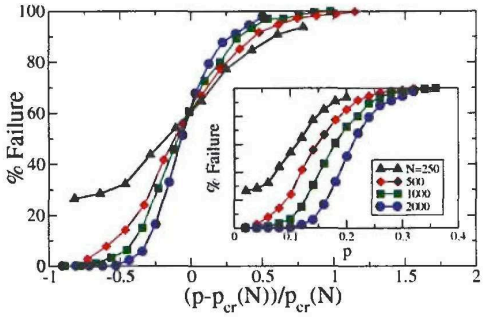

FIG. 2 (color online). Inset: Failure rates for $\tau_D = 1.0$ and different system sizes N. Main: Failure rates normalized by $p_{cr}(N)$ [cf. (3) and (4)].

regular lattice in opposite directions with velocity $v = 1/\tau_D$, and either exit the system or annihilate each other, depending on boundary conditions. No persistent activity results in either case. However, self-sustained activity may arise for nonzero p, as shown in Fig. 1. Persistence relies on the reinjection of activity via a shortcut into a previously active domain that has by then recovered; this reinjection can occur only if the shortcuts are unidirectional. For a fixed value of p, any particular network realization has a different connectivity graph that may or may not sustain persistent activity. We typically average over 2000 realizations to calculate the probability of persistent activity; the complementary probability of *failure* to sustain activity is shown in Fig. 2 (inset) as a function of the density p of random connections for four different system sizes. In this regime, the probability of failure is an increasing function of p that crosses over from 0 to 1 with increasing steepness as the size N of the system increases.

Failure to sustain activity is a simple consequence of the intrinsic dynamics of the neurons. Pulses travel outwards from an initial activity seed and spawn new pulses at a rate that increases with p. A currently inactive neuron can fire again only if enough time has elapsed from its preceding firing to allow for a recovery to $V \geq 1 - g_{syn}$. A single input will be able to elicit a spike only if the elapsed time exceeds $T_R^{(1)}$, with

$$T_R^{(n)} = \tau_m \ln\left(\frac{I_{ext}}{I_{ext} + ng_{syn} - 1}\right). \quad (2)$$

If activity recurs to a given site too rapidly, the neuron will fail to produce a spike, and the pulse of activity will die out. A critical density p_{cr} for the transition from self-sustained activity to failure can be estimated from

$$T_A(p_{cr}) = T_R^{(1)}, \quad (3)$$

where $T_A(p)$ is the time needed for the activity to spread across the whole network. At a fixed velocity for pulse propagation, this time corresponds to the largest distance across the network. This distance has been calculated for bidirectional shortcuts using a mean-field approach [16]; when extended to the case of unidirectional shortcuts it results in

$$\sqrt{\left(1 + \frac{4}{pN}\right)} \tanh\left[\sqrt{\left(1 + \frac{4}{pN}\right)} \frac{pT_A(p)}{2\tau_D}\right] = 1. \quad (4)$$

An implicit expression for p_{cr} and its dependence on the system size N and the propagation velocity v follows from combining Eqs. (3) and (4); for large N, $p_{cr}(N) \propto \ln N$. Failure rate curves as a function of $[p - p_{cr}(N)]/p_{cr}(N)$, shown in Fig. 2, cross at the theoretically predicted value. This observation, together with the increased steepness of these curves with increasing N, indicates that a well-defined transition to failure occurs in the thermodynamic limit.

This well-defined transition to failure occurs only for sufficiently fast waves, i.e., for short delay τ_D. For larger τ_D the dynamics of the system become quite more complex, and the fraction of realizations that fail before a fixed time ($t_{max} = 2000$ in Fig. 3) becomes a nonmonotonic function of p. While at low p the firing patterns are highly regular (cf. Fig. 1) and all failures occur within one or two cycles of the initial activity, for higher p the patterns are more disordered (cf. Fig. 4) and the activity can persist for a very long time before failure.

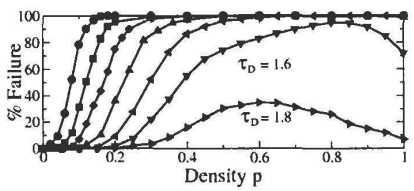

FIG. 3. Failure rates after $t_{max} = 2000$ for $\tau_D = 0.6$, 0.8, 1.0, 1.2, 1.4, 1.6, 1.8 (left to right); $N = 1000$.

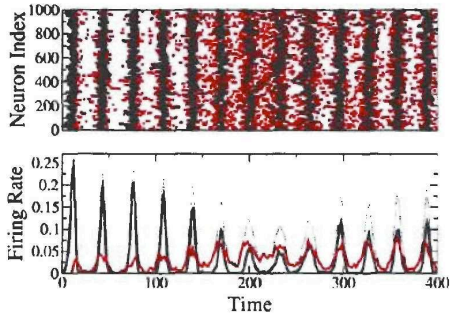

FIG. 4 (color online). Raster plot (top) and instantaneous firing rate (bottom) of neurons with ISI $> T_R^{(1)}$ (black) and ISI $< T_R^{(1)}$ [gray (red online)] for $\tau_D = 1.5$ and $p = 1.0$. Dotted line is the total firing rate.

Consequently, the distribution of failure times, shown in Fig. 5, exhibits an increasingly long tail for longer delay times.

To understand the persistence of activity beyond p_{cr}, it is important to recognize that the result for the critical density $p_{cr}(N)$ hinges on the assumption that each neuron receives but a single excitatory input during each cycle of network activity. Its recovery time is therefore given by $T_R^{(1)}$, which sets a lower bound for the interspike interval (ISI). While this assumption is well satisfied for small p, it does not hold for $p = O(1)$. In fact, the likelihood that a neuron has n incoming shortcuts follows a multinomial distribution such that the fraction of neurons receiving two incoming connections grows from about 0.05% at $p = 0.1$ to about 30% at $p = 1$. Neurons that receive n inputs can have a recovery time as short as $T_R^{(n)}$. Figure 4 reveals that such neurons, with ISIs lower than $T_R^{(1)}$, play a crucial role in maintaining network activity in the regime $p \approx 1$. While neurons with ISIs greater than $T_R^{(1)}$ (shown black in Fig. 4) can go through silent epochs with near-zero activity, neurons with shorter ISIs [gray (red online) in Fig. 4] may fire 2 or 3 times during a network cycle and carry over the network activity across these silent epochs.

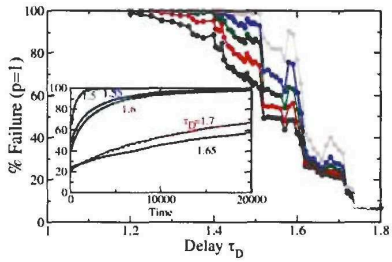

FIG. 5 (color online). Failure-time distribution. Inset: Cumulative distribution of failure times at $p = 1$ for $1.5 \leq \tau_D \leq 1.7$. Main: Failure rates at 5, 10, 20, 40, and 100 multiples of $T_R^{(1)} = 28.3$ (bottom to top). Symbols are averages over 2000 realizations.

The persistence of activity beyond p_{cr} depends sensitively on τ_D; this reflects the fact that persistence at higher densities p is due to chains or trees of neurons that bridge the silent epochs due to their multiple inputs. Since activity propagates with a fixed speed, a chain of multiple-input neurons of given length can bridge a time interval proportional to τ_D. Thus, as τ_D increases, ever shorter chains can contribute to bridging a silent epoch of given duration; the likelihood for failure will decrease accordingly. This picture is, of course, overly simplistic: whether a *topological* chain can be utilized as a *dynamical* bridge over a given silent epoch depends on the amount and timing of the inputs it receives, which in turn depend on the recent history of the entire network. Simulations reveal that the identity of the neurons that form the "bridging" dynamical chains varies from cycle to cycle in an irregular way. This implies that the effective utilization of a dynamical chain over one cycle does not guarantee its availability on the next cycle. Therefore, even systems that persist for long times may still have a finite probability of failing.

The cumulative failure distribution function $F(t)$, shown in Fig. 5 for various values of τ_D, exhibits a long tail and is well fit with stretched exponentials: $F(t) = f_\infty(\tau_D) - Ce^{-\alpha t^\beta}$ with $\beta \approx 0.4$ (dotted lines). Even though the fits are based on runs up to $t = 300\,000$ for $\tau_D = 1.65$ and $\tau_D = 1.7$, they do not provide a value of $f_\infty(\tau_D)$ accurate enough for establishing whether true persistent activity exists for a small fraction of the network realizations [$0.97 \leq f_\infty(\tau_D = 1.65) \leq 1$]. Strikingly, the dependence of $F(t)$ on the delay time exhibits a high degree of structure, suggestive of "resonances" at values of τ_D for which some chains and trees can be optimally utilized.

One of the salient features of the emergent dynamics of the model is persistent *self-sustained* activity at low densities p of shortcuts. In this regime, the network is, in fact, bistable between "off" and "on" states, and can be switched between them with sufficiently large stimuli, as illustrated in Fig. 6. The synchronous stimulation of a sufficiently large number of neurons while the network is in the on state increases the level of activity and effectively pushes the network to the right of the failure transition (cf. Fig. 2), causing a transition into the off state.

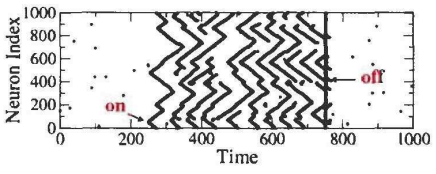

FIG. 6 (color online). Raster plot for $p = 0.10$ and $k = 5$. About 10 adjacent neurons are stimulated synchronously at $t = 250$; about 20% of the neurons are activated at $t = 750$.

To address the fact that real neuronal systems are noisy, the simulation shown in Fig. 6 includes Gaussian fluctuations in the membrane potential; their amplitude is chosen so as to cause the neurons to spike irregularly at a low rate. To keep the noisy spiking of a single neuron from generating a traveling pulse and initiating the on state, we adjust the synaptic conductance so that several adjacent neurons must fire in rapid succession in order to propagate a pulse of excitation. The network topology is modified accordingly: we extend the local coupling to include up to $2k$ neighbors ($w_{i,i\pm j} = 1$ for $j = 1, \ldots, k$) and model long-range connections via a population of intermediate excitatory neurons that both receive input from and project to multiple adjacent neurons. Under these conditions, spontaneous activity is highly unlikely to initiate traveling pulses. However, a sufficiently large stimulus, synchronous across several neurons, can again turn the state of elevated activity on and off (cf. Fig. 6); bistability is thus robust with respect to noise.

Network bistability has been hypothesized to be the neural correlate underlying the type of short-term memory known as working memory in the prefrontal cortex of monkeys and humans. Much more realistic and physiologically plausible models of cortical layers have been studied within the context of working memory (e.g., [17]). Yet, not much attention has been given to heterogeneities in network topology or to long-range excitatory connections. The work presented here suggests that closer attention be given to the role of connectivity as an additional factor that contributes to the generation of the persistent, active state associated with working memory.

In conclusion, we have investigated the effect of incorporating random unidirectional shortcuts to a one-dimensional network of locally coupled integrate-and-fire neurons. We find that even a very low density of shortcuts suffices to generate persistent activity from a local stimulus through the reinjection of activity into previously excited domains. As the density of shortcuts is increased, the substantial decrease in the effective system size characteristic of small-world networks causes a crossover into a regime characterized by failure to sustain activity for essentially all network configurations. For sufficiently slow propagation velocities of the activity and sufficiently high shortcut densities, an intriguing second crossover occurs into a regime in which the activity still fails but only after often exceedingly long and strongly chaotic transients.

The complex dynamical phenomena we find in this extremely simple model are based on a robust mechanism: propagating pulses of activity that are sustained by branching and reinjection. We therefore expect that more realistic models of neuronal networks, which may include multiple ion channels and continuous synaptic currents as well as inhibitory coupling, will show qualitatively the same behavior upon the addition of shortcuts if they originally support propagating pulses of activity [18] that annihilate upon collision. Preliminary computations show that the failure transition persists if the length of the shortcuts is limited by $L_{\max} > T_R^{(1)}/\tau_D$ [19]; this network is not truly a SWN. If the SWN is obtained by rerouting rather than adding connections, the transition is less pronounced [19]. Recently, similar networks have been used to simulate epileptic activity in hippocampus [20] and bursting in the pre-Bötzinger complex [21]. The phenomena reported here should also be accessible in excitable chemical systems [22], where shortcuts could be implemented using video feedback.

We gratefully acknowledge support by DOE (DE-FG02-92ER14303), by NSF Grant No. DMS-9804673, and by the NSF-IGERT program *Dynamics of Complex Systems in Science and Engineering* (DGE-9987577), as well as discussions with R. Clewley and R. J. Butera.

*Present address: Neurophysics and Physiology of the Motor System, Université René Descartes, Paris, France.

[1] D. J. Watts and S. H. Strogatz, Nature (London) **393**, 440 (1998).
[2] S. H. Strogatz, Nature (London) **410**, 268 (2001).
[3] R. Albert and A. L. Barabasi, Rev. Mod. Phys. **74**, 47 (2002).
[4] A. Pekalski, Phys. Rev. E **64**, 057104 (2001).
[5] A. D. Sánchez, J. M. López, and M. A. Rodríguez, Phys. Rev. Lett. **88**, 048701 (2002).
[6] M. Barahona and L. M. Pecora, Phys. Rev. Lett. **89**, 054101 (2002).
[7] R. Pastor-Satorras and A. Vespignani, Phys. Rev. Lett. **86**, 3200 (2001).
[8] V. B. Mountcastle, Brain **120**, 701 (1997).
[9] G. González-Burgos, G. Barrionuevo, and D. A. Lewis, Cereb. Cortex **10**, 82 (2000).
[10] D. A. McCormick and D. Contreras, Annu. Rev. Physiol. **63**, 815 (2001).
[11] J. Y. Wu, L. Guan, and Y. Tsau, J. Neurosci. **19**, 5005 (1999).
[12] R. Demir, L. B. Haberly, and M. B. Jackson, J. Neurophysiol. **86**, 2445 (2001).
[13] D. S. Melchitzky, G. González-Burgos, G. Barrionuevo, and D. A. Lewis, J. Comp. Neurol. **430**, 209 (2001).
[14] L. F. Lago-Fernández, R. Huerta, F. Corbacho, and J. A. Sigüenza, Phys. Rev. Lett. **84**, 2758 (2000).
[15] L. F. Lago-Fernández, F. J. Corbacho, and R. Huerta, Neural Networks **14**, 687 (2001).
[16] M. E. Newman, C. Moore, and D. J. Watts, Phys. Rev. Lett. **84**, 3201 (2000).
[17] A. Compte, N. Brunel, P. S. Goldman-Rakic, and X.-J. Wang, Cereb. Cortex **10**, 910 (2000).
[18] D. Golomb and G. B. Ermentrout, Phys. Rev. Lett. **86**, 4179 (2001).
[19] A. Roxin, H. Riecke, and S. A. Solla (unpublished).
[20] T. I. Netoff, R. Clewley, S. Arno, T. Keck, and J. A. White (to be published).
[21] W. C. Gerken, J. Shao, and R. J. Butera (unpublished).
[22] K. Martinez, A. L. Lin, R. Kharrazian, X. Sailer, and H. L. Swinney, Physica (Amsterdam) **168D**, 1 (2002).

Multiple attractors, long chaotic transients, and failure in small-world networks of excitable neurons

Hermann Riecke
Department of Engineering Sciences and Applied Mathematics, Northwestern University, Evanston, Illinois 60208

Alex Roxin
Computational Neuroscience, Departament de Tecnologia, Universitat Pompeu Fabra, 08003 Barcelona, Spain

Santiago Madruga
Max-Planck-Institute for Physics of Complex Systems, D-01187 Dresden, Germany

Sara A. Solla
Department of Physiology and Department of Physics and Astronomy, Northwestern University, Evanston, Illinois 60208

(Received 3 January 2007; accepted 2 May 2007; published online 28 June 2007)

We study the dynamical states of a small-world network of recurrently coupled excitable neurons, through both numerical and analytical methods. The dynamics of this system depend mostly on both the number of long-range connections or "shortcuts", and the delay associated with neuronal interactions. We find that persistent activity emerges at low density of shortcuts, and that the system undergoes a transition to failure as their density reaches a critical value. The state of persistent activity below this transition consists of multiple stable periodic attractors, whose number increases at least as fast as the number of neurons in the network. At large shortcut density and for long enough delays the network dynamics exhibit exceedingly long chaotic transients, whose failure times follow a stretched exponential distribution. We show that this functional form arises for the ensemble-averaged activity if the failure time for each individual network realization is exponentially distributed. © *2007 American Institute of Physics*. [DOI: 10.1063/1.2743611]

Many systems in nature can be described as a network of interconnected nodes. Networks in a growing list of systems, from social and ecological webs to the neural anatomy of simple organisms, have been shown to exhibit complex topological features that distinguish them from both ordered lattices and purely random networks. Beyond the investigation of the structural and geometrical properties of such networks, a new class of question arises when dynamical degrees of freedom are placed at their nodes. As the investigation of such dynamical complex networks proceeds, it has become increasingly clear that the network architecture can significantly influence the dynamics of the system. An understanding of emergent dynamics on complex networks requires investigating the interplay between the intrinsic dynamics of the node elements and the connectivity of the network in which they are embedded. In order to address some of these questions in a specific scenario of relevance to the dynamical states of neural ensembles, we study here the collective behavior of excitable model neurons in a network with small-world topology. The small-world network has local lattice order, but includes a number of randomly placed connections that may provide connectivity shortcuts. This topology bears a schematic resemblance to the connectivity of the cerebral cortex, in which neurons are most strongly coupled to nearby cells within 50–100 μm, but also make projections to cells millimeters away. We find that the dynamics of this small-world network of excitable neurons depend mostly on both the density of shortcuts and the delay associated with neuronal projections. In the regime of low shortcut density, the system exhibits persistent activity in the form of propagating waves, which annihilate upon collision and are spawned anew via the reinjection of activity through shortcut connections. As the density of shortcuts reaches a critical value, the system undergoes a transition to failure. The critical shortcut density results from matching the time associated with a recurrent path through the network to an intrinsic recovery time of the individual neurons. Furthermore, if the delay associated with neuronal interactions is sufficiently long, activity re-emerges above the critical density of shortcuts. The activity in this regime exhibits long, chaotic transients composed of noisy, large-amplitude population bursts. A numerical investigation of the interplay between network topology and interaction delays in this regime reveals a mechanism that underlies the observed stretched-exponential distribution of failure times for the chaotic network activity.

I. INTRODUCTION

It has been widely recognized that the connectivity of a network of active elements has a profound impact on its function. Substantial effort has therefore been devoted to the characterization of network connectivity,[1,2] leading to the identification of various measures that are significant in de-

termining the geometrical properties of the system. Particularly relevant among them are the average and maximal length of the minimal paths that connect two arbitrary nodes in the network, the clustering coefficient, which characterizes the propensity of all neighbors of a given node to be connected to each other, and the distribution for the degree, defined as the number of links that emanate from a node.

A large number of networks with complex topology fall into the class of small-world networks, characterized by short average path length and high clustering coefficient. A simple realization of such a small-world network consists of a regular lattice supplemented by a number of randomly placed connections that tend to provide connectivity shortcuts. This topology schematically resembles the connectivity of the cerebral cortex, in which neurons are most strongly coupled to nearby cells within 50–100 μm, but also project to distant cells, which can be millimeters away. Small-world properties of neuronal networks have been found in a comprehensive morphological characterization of *in vitro* two-dimensional networks,[3] and in a 1:1 network model of the rat dentate gyrus that incorporates known data about cell types, cell-specific connectivity, and axonal branch length.[4]

The dynamics of elements coupled through the connectivity of a complex network has been studied in detail for the case of oscillatory elements. The emphasis has been in determining the role of network topology in the ability to achieve synchronization in a system of coupled oscillators. The existence of long-range connections, which reduce the effective size of the network, has been found to substantially enhance synchronizability.[5,6] At the same time, the heterogeneity of the degree distribution found in many complex networks limits the ability of the oscillators to synchronize. Stable synchronization emerges from a balance between these two competing aspects of complex network topology.[7]

Excitable elements are the components of another important class of dynamical systems, whose emergent behavior is not characterized by synchronization. Locally coupled networks of excitable elements exhibit traveling waves (e.g., Refs. 8–10). If these waves annihilate upon collision, as is typically the case, persistent activity usually requires either an external drive or spontaneous excitation by noise. In models for neural systems driven by noise,[11–13] networks with nonlocal connections between their elements exhibit a tendency towards relatively ordered oscillations in the population activity. The spatial structure of such noise-induced waves becomes less coherent with an increase in the fraction of nonlocal connections.[14] The combination of local connectivity with a small number of nonlocal connections allows a time-periodic localized external input to entrain the whole system much faster than in a purely local network; at the same time, the oscillations are much more coherent than in a truly random network.[15,16] Oscillatory activity at the population level has also been observed in small-world networks of binary McCulloch-Pitts neurons connected through both excitatory and inhibitory synapses.[17]

The dynamics of networks of excitable elements depend very strongly on both the range of the coupling and on the length of the refractory period relative to the time scales associated with propagation. In Ref. 18, the authors consider both scale free and random networks of three-state excitable neurons, and find that short refractory periods enable the propagation of sustained activity through the activation of short loops. These short loops are frequently found in many types of complex and random networks. In the noiseless case, they can only be activated if the initial conditions capture the broken symmetry associated with a choice of direction for the propagation of activity.[18] A related model of three-state excitable elements on a small-world network has been proposed to study the propagation of infectious diseases. In this model, the introduction of nonlocal connections was found to induce a transition to a state with coherent population oscillations.[19]

Most studies of the dynamics of complex networks have assumed that the interaction between node elements is bidirectional. This is a very reasonable assumption in the context of epidemic models,[19] and it would also apply to ensembles of neurons connected via gap junctions.[12] In the absence of noise, activity that is initiated through the excitation of individual neurons in an otherwise quiescent state results in wave fronts that propagate symmetrically in both available directions; if both local and nonlocal connections are bidirectional, all wave fronts are generated as symmetric pairs that annihilate upon collision. In such a system, persistent activity can only arise from initial conditions that suitably break the symmetry between the two possible directions for the propagation of activity.

In the cortical neural ensembles that motivate this work, the coupling between neurons is predominantly not bidirectional; most connections involve chemical synapses that transmit information from the presynaptic axon to the postsynaptic dendrite. In this scenario, it is more appropriate to consider directed networks with unidirectional connections. In previous work,[20] we have investigated networks in which the local connections are bidirectional, based on the assumption that the probability for reciprocal axo-dendritic connections is quite high for neurons in close proximity, while the nonlocal connections that provide shortcuts are unidirectional. This network is a modification of the by now classical small-world network,[21] in that the added nonlocal connections are directed. We found that just a few unidirectional shortcuts suffice for sustaining persistent activity, even when activity arises from localized excitations that do not break the symmetry between the two possible directions of propagation. However, as the density of shortcuts is increased, an increasing number of network configurations support only a brief burst of population activity after which the activity dies out. When the speed associated with the propagation of activity is low, this failure of network activity was found to be delayed and to occur only after many cycles of chaotic population bursts. The simplicity of this model allowed for an analytic description of the failure transition and for detailed numerical analysis.

The properties of this simple model[20] provide important insight into the phenomena found in simulations of more elaborate models motivated by specific biological systems. In Ref. 22, the connection between the topology of a neural network and its tendency towards epileptic seizures has been studied and related to the degree of recurrent connectivity in

different parts of the hippocampus. The origin of bursting behavior was addressed in Ref. 23. The common view on bursting behavior is that it arises when fast spiking drives a slow process, typically associated with slow kinetics, that in turn can shut off the spiking activity. However, no such slow kinetics are needed if the network displays small-world connectivity.[23] Both the seizing activity described in Ref. 22 and the bursting activity described in Ref. 23 find a common interpretation in the mechanisms that underlie the failure transition found in the simple model analyzed in our earlier work.[20] A rapid spread of activity followed by persistent oscillations has also been observed in recent chemical experiments based on the Belousov-Zhabotinsky reaction; in this system, unidirectional shortcuts were implemented through the photosensitive properties of the reaction.[24,25]

Here we build on our previous results, and present a detailed characterization of the persistent states and the dependence of their properties on the density of shortcuts; we also investigate the long chaotic transients and provide an explanation for the stretched exponential that characterizes their eventual failure. In Sec. II we define the model: a network of excitable integrate-and-fire neurons coupled via excitatory pulses in a small-world topology with unidirectional shortcuts. In Sec. III we discuss the persistent states and the crossover from persistent activity to failure for the case of rapidly propagating waves. In Sec. IV we analyze the exceedingly long chaotic transients in the regime of slowly propagating waves. In the concluding Sec. V we discuss our results in light of other work on neural networks with small-world topology.[4,22,23]

II. NEURAL MODEL AND NETWORK CONNECTIVITY

We consider a one-dimensional network: a ring of N identical integrate-and-fire neurons. The state of the ith neuron is described by its membrane potential V_i, which is dynamically controlled by the spiking activity of the neurons that project onto it,

$$\tau \frac{dV_i}{dt} = -V_i + RI_{\text{ext}} + g_{\text{syn}} \sum_{j=1}^{N} w_{ij} \delta(t - t_j - \tau_D). \tag{1}$$

In order to fully specify the dynamics of integrate-and-fire neurons, this set of N equations needs to be supplemented with a condition for spiking whenever the membrane potential reaches a specified threshold, and with a reset condition for the membrane potential after the emission of a spike,

$$V(t^+) = V_{\text{res}} \quad \text{whenever } V(t^-) = V_{\text{th}}. \tag{2}$$

In Eq. (1), τ is the membrane time constant, g_{syn} is the synaptic strength measuring the change in membrane potential due to each incoming spike, $w_{ij}=1$ or 0 indicates the presence or absence of a synaptic connection from neuron j to neuron i, t_j is the time at which neuron j fires a spike, I_{ext} is an external current, and R is the membrane resistance. The effective delay τ_D in the neuronal interaction includes both the time for the spike or action potential to propagate along the axon and the time needed for initiating the triggered action potential. When this latter time dominates over the axonal delay, the dependence of τ_D on the physical distance between the presynaptic and the postsynaptic neurons can be neglected. Postsynaptic currents due to synaptic activation are considered instantaneous and are therefore modeled as delta functions. The process of spike emission is described in Eq. (2): whenever the membrane potential of a neuron reaches the threshold value V_{th}, a spike is emitted and the membrane potential is reset to the value V_{res}. Without loss of generality, we write these two equations in terms of dimensionless quantities by measuring V_i and g_{syn} with respect to V_{res}, setting $V_{\text{res}}=0$ and $V_{\text{th}}=1$, and rescaling time by τ. (In Ref. 20, we used $\tau=10$.) Also, we replace RI_{ext} by the steady-state voltage V_∞; this is the asymptotic value that V_i would reach in the absence of synaptic input. We restrict the model to the case of excitable rather than spontaneously oscillating neurons by setting $V_\infty < V_{\text{th}}=1$, and consider only initial conditions such that at most a few neurons are triggered to spike while the rest of the network is in a quiescent state. In the absence of noise, this initial condition implies that neurons can only fire at times that are integer multiples of τ_D. Since the dynamical evolution of the membrane potentials can be integrated exactly between subsequent spikes, the time step for the numerical computations is taken to be $\Delta t = \tau_D$.

Cortical neurons often receive not only local input from nearby neurons but also input from some distant neurons through long-range projections. We mimic this heterogeneous connectivity through an extremely simplified network architecture: each neuron is bidirectionally connected to its $2k$ nearest neighbors, i.e., $w_{ij}=1$ for $|i-j| \leq k$, $j \neq i$, and unidirectionally connected to pN randomly chosen neurons. The parameter p thus indicates the density of additional unidirectional connections, as a fraction of the total number N of neurons.

The dynamics that arise from Eqs. (1) and (2) in the case of purely local connectivity ($p=0$) and in the absence of noise depend only on the interplay between the strength g_{syn} of the synapses, the number $2k$ of local connections per neuron, and the delay τ_D. The dependence on g_{syn} and τ_D is most easily illustrated for first-nearest-neighbor connectivity, $k=1$. In this case, if the presynaptic input is weak enough to satisfy $g_{\text{syn}} + V_\infty < V_{\text{th}}=1$, this presynaptic input is insufficient to cause a spike and the activity is not propagated. In contrast, if the presynaptic input is strong enough to satisfy $g_{\text{syn}} + V_\infty > V_{\text{th}}=1$, it results in a propagating wave of speed $1/\tau_D$. After spike emission, the voltage is reset to $V_{\text{res}}=0$, and the neuron is only ready to fire again after it has recovered to the extent that an input of magnitude g_{syn} is sufficient to trigger another spike. This recovery time is given by

$$T_R = \ln\left(\frac{V_\infty}{V_\infty + g_{\text{syn}} - 1}\right). \tag{3}$$

Note that T_R is not the intrinsic refractory period of the neuron, since this integrate-and-fire neuron can fire at arbitrarily large frequencies for sufficiently strong input g_{syn}.

Due to the bidirectionality of the local connections, the firing of each neuron not only triggers a spike in the neuron ahead of it in the direction of wave propagation, but also gives an input to the neuron behind it, which thus receives an input at a time $2\tau_D$ after its own firing. If $T_R > 2\tau_D$, this input is not sufficient to trigger a new spike, and the activity

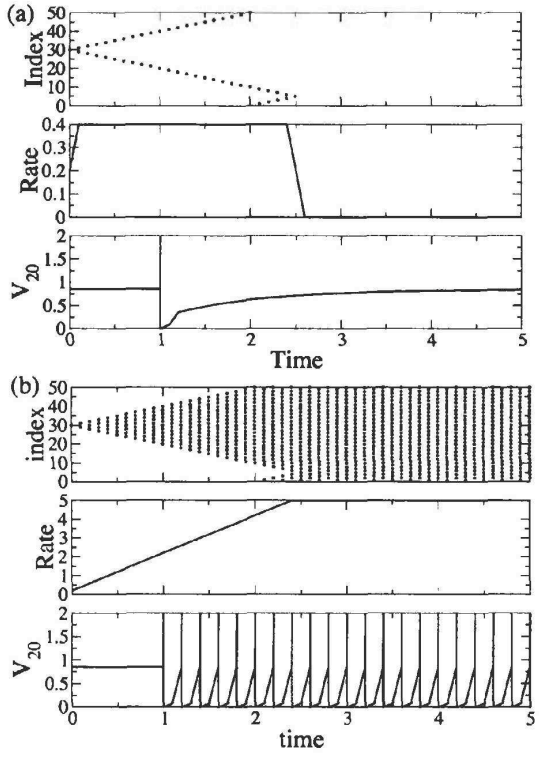

FIG. 1. Dynamics in a regular network of 50 neurons with first-nearest-neighbor coupling. Parameters are $V_\infty=0.85$ and $\tau_D=0.1$. (a) A weak synaptic coupling $g_{syn}=0.2$ results in a propagating wave. The two wave fronts meet and annihilate at time 2.5. Top: Raster plot showing spike times for each neuron. Middle: Population firing rate. Bottom: Membrane potential of neuron number 20. (b) A strong synaptic coupling $g_{syn}=1.0$ results in a wave that entrains all neurons in its path. The final state of the network consists of two synchronous groups of neurons firing out of phase with each other. Top, middle, and bottom panels as in (a). Note that the maximum possible firing rate is $1/\tau_D=10$.

propagates away from the site of initiation as a wave to which each neuron contributes exactly one spike, see Fig. 1(a). However, if $T_R \leqslant 2\tau_D$, the wave front entrains all the neurons in its wake, eventually leading to synchronized activity of the whole network. In the absence of autapses, i.e., for $w_{ii}=0$, the network breaks up into two synchronous groups of neurons that fire out of phase with one another, see Fig. 1(b). In the general case, a neuron receives inputs from k neighbors as the wave approaches; the input coming from a neuron at a distance n is discounted by the factor $e^{-(n-1)\tau_D}$. A propagating wave can thus be sustained if $g_{syn}e^{\tau_D}\sum_{n=1}^{k}e^{-n\tau_D}+V_\infty > V_{th}=1$.

For simplicity, we will focus on the case of first-nearest-neighbor coupling in the regime in which waves of excitation propagate but do not entrain activity in their wake. This choice implies $k=1$ and constrains the allowable values of V_∞ and g_{syn}; we use $V_\infty=0.85$ and $g_{syn}=0.2$ unless otherwise noted. In this regime, the collision of two waves leads to their mutual annihilation and, after having fired in a propagating wave, a neuron can be triggered to fire by a single input of size g_{syn} after a time

$$T_R^{(1)} = \ln\left(\frac{V_\infty - g_{syn}e^{2\tau_D}}{V_\infty + g_{syn} - 1}\right). \tag{4}$$

This calculation includes the input received from the neuron ahead in the wave, at a time $2\tau_D$ after spiking.

The model specified by these assumptions together with Eqs. (1) and (2) is used here as a simple model for the generation and propagation of waves of activity in cortical tissue. As discussed in the following sections, the incorporation of random connections qualitatively alters the dynamics of the network and sustains a rich variety of spatiotemporal patterns.

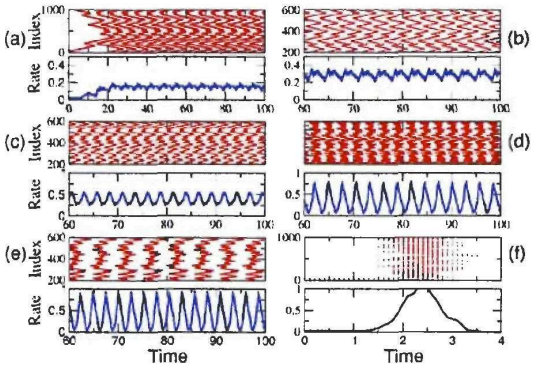

FIG. 2. Examples of network dynamics for $\tau_D=0.1$ and for different values of the density p of shortcuts. The values $p=0.01$, 0.05, 0.10, 0.15, 0.20, 0.25 correspond to panels (a)–(f), respectively. Each panel shows both spiking activity and population firing rate. Note different temporal scale on panel (f).

III. THE ORDERED REGIME: ATTRACTORS AND FAILURE

The dynamics of the model depend on several parameters. Once the input current $V_\infty=0.85$ and the synaptic strength $g_{syn}=0.2$ have been fixed, the dynamics arising from Eqs. (1) and (2) are determined by the remaining two parameters: the fraction p of randomly placed shortcuts and the delay τ_D associated with the neural interaction.

The dynamics for $p\neq 0$ differ qualitatively from those for $p=0$. The presence of shortcuts allows the waves of excitation to be reinjected into portions of the network which have been previously excited. This process of reinjection may lead to persistent network activity, as shown in Fig. 2 for several values of the density p. As the waves spread outward from the initial site of activation, they encounter shortcut connections that inject activity elsewhere in the network. As for the $p=0$ case shown in Fig. 1(a), wave fronts that meet annihilate. After some time, the activity settles into a stable pattern in which the rates of wave generation and annihilation are balanced.

When averaged over time and across network configurations at a fixed value of the shortcut density p, the firing rate of these persistent states increases rapidly with p, and saturates around $p\sim 0.1$ [Fig. 3(a)]. This saturation is a conse-

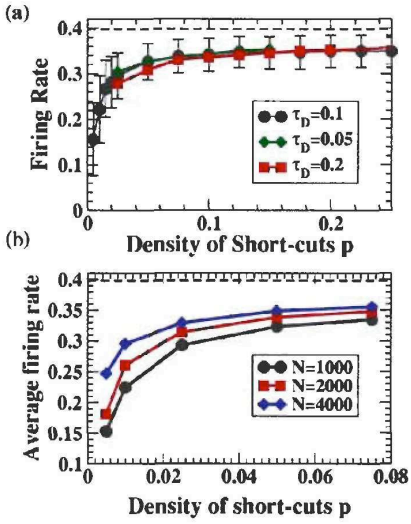

FIG. 3. Population firing rate, averaged over 1000 configurations for $p<0.2$ and over 5000 configurations for $p>0.2$. The maximal value of the firing rate, $1/T_R^{(1)}$, is indicated in both panels by a dashed horizontal line. (a) Firing rate as a function of the density of shortcuts p for different values of the delay τ_D for a network of size $N=1000$. Bars give the standard deviation of the firing rate across configurations for $\tau_D=0.1$. (b) Firing rate as a function of the density of shortcuts p for different values of the system size N with $\tau_D=0.1$.

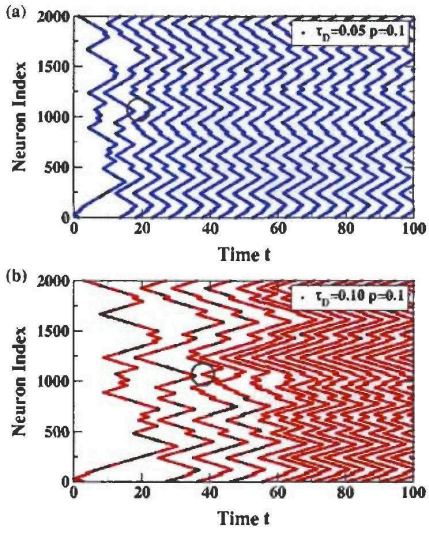

FIG. 4. Dynamics in a network of $N=2000$ neurons with a density of shortcuts $p=0.1$. The same network configuration and the same initial activation is used in both panels. The only difference is in the delay time: $\tau_D=0.05$ for the top panel and $\tau_D=0.10$ for the bottom panel. Note that more waves travel through the system when the delay is longer. Circles indicate a new wave spawned for $\tau_D=0.10$ but not for $\tau_D=0.05$.

quence of the neuron's finite recovery period $T_R^{(1)}$ of Eq. (4); its inverse is the maximal firing rate, indicated as a dashed line in both panels of Fig. 3. As shown in this figure, the firing rate comes very close to this maximal value. As the system size is increased, saturation is reached at smaller values of p [Fig. 3(b)].

The firing rate is essentially the inverse of the time between successive waves passing through a specific node in the ring of neurons. Thus, one may expect that decreasing the wave speed by increasing τ_D would reduce the mean firing rate. However, this is not the case. As shown in Fig. 3(a), the firing rate is quite insensitive to wave speed. The reason for this effect is illustrated in Fig. 4. The two panels show the spatiotemporal pattern of activity for the same network configuration and the same initial activation, but for different delay times τ_D. At the larger delay time, additional waves are excited through the shortcuts. An example of the appearance of such a new wave can be seen at $t=380\tau_D$, a time indicated by a circle in both panels of Fig. 4. At this time, a new wave is spawned by neuron 1071 for $\tau_D=0.1$ but not for $\tau_D=0.05$. These additional waves increase the firing rate in a manner that may even overcompensate for the reduced wave speed, as demonstrated by the higher density of waves for $\tau_D=0.1$ at times beyond $t=800\tau_D$.

Only a few shortcuts are present for low p, and many pathways leading to persistent activity consist only of large closed loops, which result in low firing rates. As p increases, the typical loop size decreases, and network configurations with only large loops and correspondingly low firing rates become increasingly unlikely. This effect is illustrated in the probability density function for the firing rate, shown in Fig. 5. As p increases, the distribution is shifted towards larger firing rates and it narrows substantially, reflecting a saturation close to the maximal firing rate set by the recovery time $T_R^{(1)}$. This maximal firing rate is marked by a dashed vertical line in Fig. 5.

For small values of p, the state of persistent activity settles into a periodic pattern whose oscillations increase in amplitude with increasing p. This effect is clearly illustrated in panels (a)–(e) of Fig. 2. A quantitative description of this effect is shown in Fig. 6, in which the standard deviation of the firing rate, averaged over a large number of network configurations that exhibit persistent activity for a given value of p, is used to characterize the amplitude of the oscillations. An additional feature of this regime, also apparent from panels (a)–(e) of Fig. 2, is that the time for these oscil-

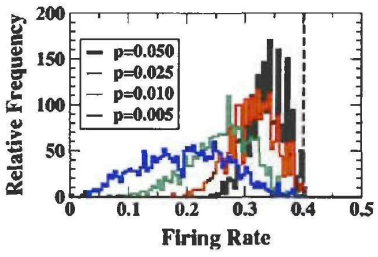

FIG. 5. (Color) Probability distribution of firing rates for several values of p, for networks of $N=2000$ neurons with $\tau_D=0.1$. As p increases, the distributions narrow in width as they shift towards the maximal firing rate $1/T_R^{(1)}$, indicated by a dashed vertical line.

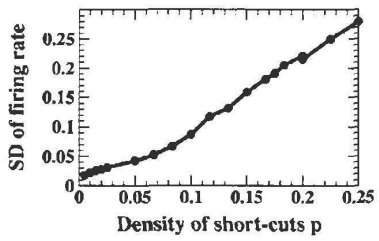

FIG. 6. Amplitude of oscillatory activity, measured through the standard deviation of the firing rate, as an increasing function of the shortcut density p. The standard deviation is obtained as an average over 5000 network configurations that exhibit persistent activity for $\tau_D=0.1$; $N=1000$.

lations to become established after the excitation of a single neuron decreases with increasing p. This property is in agreement with the results of Refs. 15 and 16, which found that, when excited through a small cluster of driven oscillatory neurons, small-world networks of either Hodgkin-Huxley or FitzHugh-Nagumo neurons are entrained much more quickly than regular networks (with no shortcuts) of the same types of neurons.

For larger values of p, the activity patterns can be quite complicated. In this regime, as in the small p regime, all neurons get excited during an oscillation cycle of network activity. However, in this regime not all neurons and not all connections between them are necessary for the persistence of activity, as illustrated in Fig. 7. The full raster plot of network activity shown in the top panel depicts the spikes from all neurons (black dots). This plot also identifies the spikes from those neurons that are essential for sustainability (red dots). These neurons provide a pathway for recurrence,[26] and they are found as follows. At an arbitrary time once the steady state has been reached, all neurons that fire at that time step are labeled. A backwards search is then performed for preceding ancestors of these labeled neurons,

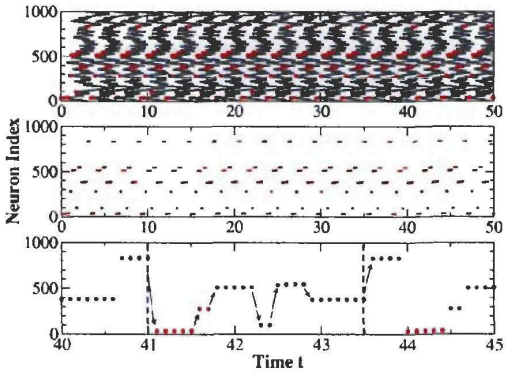

FIG. 7. Spiking activity in a network of $N=1000$ neurons with a density of shortcuts $p=0.1$ is shown in the top panel for $\tau_D=0.1$. The activity of neurons that are part of the backbone pathway is indicated in red. The middle panel shows the spiking activity within the backbone. The enlargement shown in the bottom panel displays periodic activity, with a period longer than the recovery time $T_R^{(1)}=2.494$ (delimited by dashed vertical lines). See text for details.

i.e., those presynaptic neurons that fired one delay τ_D ago and triggered the activity of the labeled neurons. These one-step ancestors are labeled in turn, and the process is iterated backwards in time until $t=0$ is reached. The pattern of labeled neurons quickly converges to a small subset, as shown in the middle panel of Fig. 7. Only the neurons in this reduced subset contribute to the persistence of the pattern; the remaining neurons could be cut out of the network without destroying the persistent activity. The pattern of activity along this backbone, shown in the bottom panel of Fig. 7, is periodic in time. The period is only slightly longer than the recovery time $T_R^{(1)}$, indicated by the dashed vertical lines (note the expanded time scale in this panel). Such backbone pathways have also been identified in an experimental study of the excitable Belousov-Zhabotinsky reaction;[25] in this photosensitive system, unidirectional shortcuts were implemented through local optical excitation.

A striking feature of this regime is that a network configuration capable of sustaining persistent activity displays an extraordinarily large number of different attractors. To assess the number of coexisting attractors we focus on the regime of low shortcut density, where all solutions are periodic. Each solution can be characterized by its period, its mean firing rate, and the standard deviation of the firing rate. A labeling of attractors based only on these three measures is likely to underestimate the total number of attractors; however, it suffices to find a large number of them, as shown in Fig. 8. This figure illustrates attractor multiplicity for a randomly chosen network configuration of $N=1000$ neurons with $p=0.05$ and $\tau_D=0.1$. Each of the 471 distinct stable patterns of persistent activity identified in Fig. 8(a) arises from an initial condition in which only one neuron is activated. As shown in Fig. 8(b), which shows the number of initial conditions that lead to a solution with a given period, many of these stable patterns have the same period (note the logarithmic scale). In contrast, the standard deviation of the firing rate [Fig. 8(c)] shows great variability, reflecting different temporal evolutions of the firing rate within a period.

A large number of attractors is typical for these networks. Figure 9 shows the number of attractors as a function of network size; black circles represent data points obtained as averages over 20 different network configurations of a fixed size. Most attractors have quite small basins of attractions: within the restricted set of initial conditions in which only a single neuron is excited, most attractors can be reached from only one such initial condition (red squares). The overall number of attractors increases roughly linearly with system size for large values of N, as does the number of attractors with different periods (blue diamonds), but the latter is about an order of magnitude smaller than the total number of attractors. The identification of attractors requires that networks achieve a steady state of persistent activity, but since the duration of the transients grows with system size, the computation time grows faster than N^2. This precludes us from simulating significantly larger system sizes than shown in Fig. 9; such data would be necessary to reliably estimate scaling relations between network size and number of attractors. (For $N=4000$ the computation takes over 2 weeks on a desktop PC.) Preliminary computations with more general

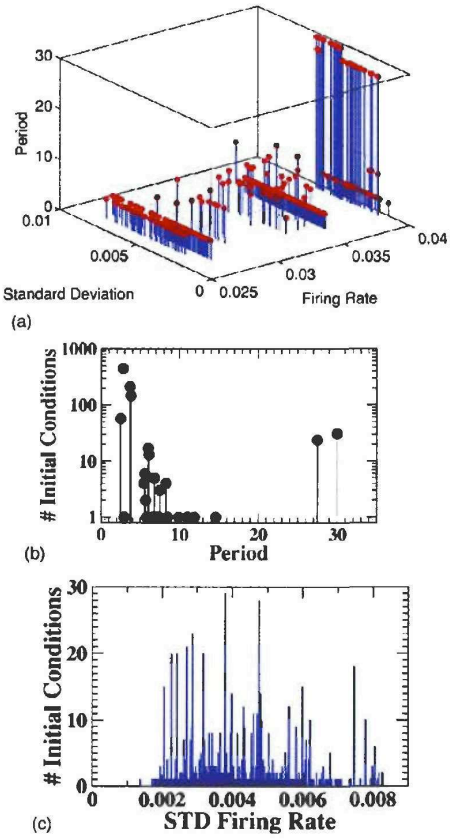

FIG. 8. Large number of attractors for a specific network configuration, with $N=1000$ neurons, $p=0.05$, and $\tau_D=0.1$. (a) The mean firing rate, its standard deviation, and the period of all 471 distinct attractors evoked by initial conditions in which only one neuron is activated. (b) Number of initial conditions that lead to an attractor with a given period; many attractors, although distinct, have the same period (note the logarithmic vertical scale). (c) Number of initial conditions that lead to an attractor with a given standard deviation of the firing rate.

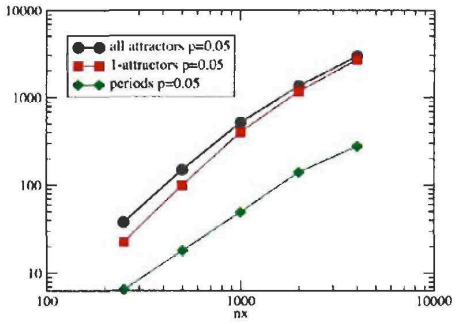

FIG. 9. Number of attractors: all attractors (circles), attractors with basin of attraction of size one (squares), and attractors with different periods (diamonds; note different vertical scale on the right) as a function of network size N.

initial conditions reveal many more attractors than those shown in Fig. 8. Thus, while the restricted initial conditions that give rise to Fig. 9 suggest an almost linear increase in the number of attractors with system size, the full number of attractors may grow substantially faster.

At this point, the origin for this exceedingly large number of different attractors is not clear. In all-to-all coupled oscillator systems, factorially large numbers of attractors are due to the permutation symmetry associated with the global coupling.[27] The small-world networks investigated here do not possess such symmetry. In this case, the large number of attractors found for a specific network configuration is likely to be due to a combination of geometrical and dynamical causes: the coexistence of many backbones that can independently support sustained activity, and the variability in membrane potentials that can result in distinct but not too different firing patterns. While we find transitions between different attractors in the presence of finite-amplitude noise,[26] we have not investigated whether this system exhibits the extreme noise sensitivity found in the case of all-to-all coupled oscillators, where it is due to the crowding of large numbers of attractors.[27]

As the density p of shortcuts increases, the distance traveled by the waves before encountering the entrance to a shortcut decreases. Consequently, waves of excitation spread throughout the network more rapidly, as shown in the progression of spatiotemporal patterns of Figs. 2(a)–2(e) for increasing values of p. If p becomes too large, activity spreads too fast and it quickly dies away, as shown in Fig. 2(f). Since the shortcuts are randomly placed, different network configurations will exhibit different dynamics. Thus, while the overall likelihood of persistent activity decreases with increasing p, the actual network dynamics depend on the particular network configuration.

The mechanism that leads to the extinction of network activity is easily elucidated.[20] Once a neuron has emitted a spike, its membrane potential is reset to a fixed value, chosen here to be $V_{res}=0$. While the membrane potential of the neuron recovers towards its resting value V_∞, activity spreads through the network, eventually finding its way back. Once this occurs, the neuron receives synaptic input equal to g_{syn}. This input will be sufficient to trigger a spike only if this neuron has recovered sufficiently. It is therefore clear that as the number of shortcuts is increased and activity spreads more rapidly, the network is less likely to sustain persistent activity. Whether or not this mechanism of premature return will lead to the extinction of activity in a given network depends on its particular configuration. Many different network configurations for a given value of p have been simulated in order to measure the fraction that fail to sustain persistent activity. This probability of failure is shown as a function of p for different values of the system size N in the left inset of Fig. 10. In agreement with our intuitive argument, the probability that a network drawn at random fails to sustain activity increases with increasing p. In fact, there is a sharp crossover from a low p regime characterized by the ability to sustain persistent activity into a large p regime in which activity will always fail. The transition between these

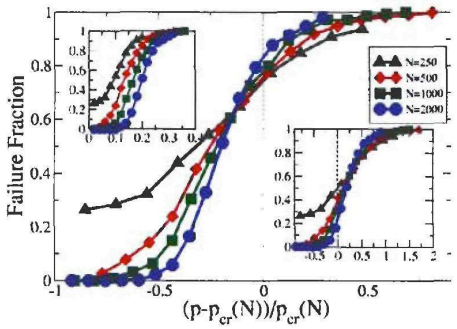

FIG. 10. Probability of failure as a function of shortcut density for different values of the system size N. The density of shortcuts is scaled by p_{cr} from Eq. (8). Left inset: unscaled data. Right inset: data scaled by p_{cr} from Eq. (7).

two regimes occurs at higher values of p as the system size N increases.

As discussed in Ref. 20 this transition can be captured in a mean-field approximation in which the return time is assumed to be identical for all neurons. In this approximation, the maximum return time T_A needed for the activity to traverse the entire network can be expressed as a function of only p and N. Setting this time to be equal to the recovery time yields an upper bound for the critical density of shortcuts at which a transition from persistent activity to failure occurs,

$$T_A(p_{cr}) = T_R^{(1)}. \tag{5}$$

An approximate form for T_A is easily derived. Assume an initial condition in which a single neuron fires at time $t=0$. Given a density p of shortcuts, the entrance to a shortcut will be typically encountered after $1/p$ neurons have fired, which occurs after a time $\tau_D/2p$; the factor of 2 is due to the two wave fronts that emerge from the initially activated neuron and propagate in opposite directions. Due to the activity injected through the shortcut, four wave fronts are now propagating through the system; $2/p$ neurons will fire during the subsequent time interval of duration $\tau_D/2p$, at the end of which a new shortcut entrance will typically be found and two more wave fronts will be generated. The process is iterated, with $2^{k-1}/p$ neurons firing during the kth cycle. It takes n cycles to ensure that all neurons have fired, with n such that

$$\sum_{k=0}^{n-1} 2^k = pN, \tag{6}$$

which leads to a total time

$$T_A(p) \equiv n\frac{\tau_D}{2p} = \tau_D \frac{\ln(1+pN)}{2p \ln 2}. \tag{7}$$

This is a purely geometric result for the time it takes for activity to traverse the entire extent of the network; this time is related trivially to the largest distance in the network. The geometric mean-field properties of small-world networks have been analyzed by Newmann, Moore, and Watts,[28] who used a continuum limit to calculate the fraction of a small-world network that is covered by starting at a single point and extending outwards a distance r in both directions; this is equivalent to following the spread of waves of activation during a time $r\tau_D$ for the neural network considered here. The calculation in Ref. 28 takes into account two effects that were omitted from their earlier calculation[29] and from our derivation, Eq. (7). First, as the network is covered, a shortcut might lead to a part of the network that has already been traced over; this contribution should not be counted. In the neural scenario, this is equivalent to an attempt at injecting activity into a neuron that has already fired but not yet recovered to the point where it can fire again. Such a shortcut does not contribute to sustained activity. Second, when two covering fronts meet, they stop and no longer contribute. In the neural network, this corresponds to activity wave fronts that meet and annihilate. The incorporation of these two additional mechanisms leads to a two-component model that correctly describes both the covered fraction of the network and the number of fronts.[28] The result, when applied to the neural network of Eq. (1), yields

$$\sqrt{\left(1+\frac{4}{pN}\right)} \tanh\left[\sqrt{\left(1+\frac{4}{pN}\right)}\frac{pT_A(p)}{2\tau_D}\right] = 1. \tag{8}$$

The identification $T_A(p_{cr}) = T_R^{(1)}$ then yields the mean-field estimate $p_{cr}^{(MFT)}$ for the density at the failure transition.

The main panel in Fig. 10 shows the failure rates as a function of shortcut density, with p rescaled by the critical density $p_{cr}^{(MFT)}$ that follows from Eq. (8). All rescaled curves intersect at a common value of p, which defines the transition point at p_{cr}. The mean-field theory yields an upper bound, $p_{cr} < p_{cr}^{(MFT)}$. It is interesting to note that a similar rescaling using the estimate for p_{cr} that results from Eq. (7) also produces a family of rescaled curves that intersect at a common value of p, as shown in the right inset of Fig. 10. While $p_{cr}^{(MFT)}$ overestimates the true p_{cr} at which the rescaled curves cross, the estimate based on Eq. (7) underestimates the true p_{cr}. In an earlier report[20] we incorrectly used T_R instead of $T_R^{(1)}$ as the recovery time in Eq. (8). The corresponding rescaled curves intersected at zero. We cannot tell whether this agreement with the true p_{cr} was just a coincidence or the consequence of a subtle cancellation between factors leading to overestimation or underestimation. In any case, it is worth emphasizing that all three methods, although only approximate, succeed in rescaling the curves in the left inset of Fig. 10 so as to obtain a unique crossing. This is due to the fact that these phenomenological approaches result in estimations for the critical density p_{cr} with very similar dependencies on system size N; these estimates seem to provide a good approximation to the true dependence on system size.

The failure transition occurs at the value of p for which the geometrical quantity $T_A(p)$ equals $T_R^{(1)}$. This recovery time is thus the central quantity that determines persistence or failure for a given shortcut configuration. It is worth pointing out that this recovery time is not the same as the absolute refractory period T_r. During the refractory period, neurons are inhibited from receiving synaptic input, while the mem-

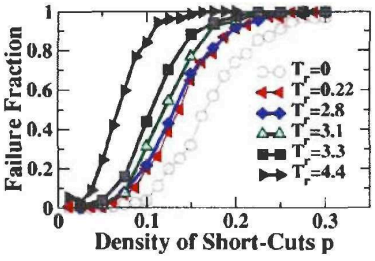

FIG. 11. Dependence of failure probability on shortcut density for different values of the refractory period T_r. Shown are averages over 500 network configurations, with $N=1000$, $\tau_D=0.1$, and $T_R=2.83$.

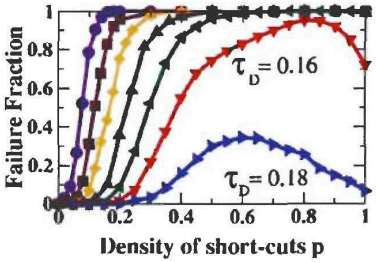

FIG. 12. Dependence of failure probability on shortcut density for different values of the delay $\tau_D=0.06, 0.08, 0.10, 0.12, 0.14, 0.16$. Shown are averages over 2000 network configurations for $N=1000$. Note the nonmonotonic character of the curves for large enough delay. In the large p regime, failure probability is estimated within a finite time $T^*=100$.

brane potential still relaxes towards its resting value. While T_r is an intrinsic property of individual neurons, $T_R^{(1)}$ depends strongly on the strength of the synaptic coupling. The curves in Fig. 11 show the fraction of network configurations that fail to sustain persistent activity for different values of the refractory period T_r. For $T_r<2\tau_D$, the input that neurons in the wake of a propagating wave receive at a time $2\tau_D$ after their own firing is unaffected, and the relevant recovery time is $T_R^{(1)}$ [cf. Eq. (4)]. The corresponding curves are as those for $T_r=0$, shown in Fig. 10. The input received at $2\tau_D$ after firing is suppressed for $T_r>2\tau_D$. In this low p regime, the persistent states do not depend on neurons receiving additional inputs before the one that triggers a spike, and the failure transition is controlled by T_R [cf. Eq. (3)]. The failure transition is thus independent of T_r as long as $2\tau_D<T_r<T_R$. It is only for $T_r>T_R$ that the refractory period suppresses relevant input to the neurons and affects the failure transition. This is illustrated in Fig. 11, where the refractory period T_r is seen to have little effect on persistent activity when it takes values between $2\tau_D=0.20$ and $T_R=2.83$.

In our analysis of persistent activity and transition to failure, we have also considered the possibility of an upper bound in the length of allowed shortcuts. We summarize our results without showing the corresponding numerical data: the behavior of the system is qualitatively unchanged as long as this upper bound exceeds a threshold value; below threshold, the network is essentially only locally coupled and the failure probability rapidly approaches one. Other modifications to the distribution of shortcut lengths might include allowing for a nonuniform distribution. It is unclear how a nonuniform distribution of shortcut lengths would affect the dynamics. However, it has been shown that one-dimensional networks maintain a small-world structure if the distribution of shortcut lengths is power-law with power <2.[30] We assume that the regime we have discussed in this section will also be present in such a scenario.

IV. THE DISORDERED REGIME: CHAOTIC TRANSIENTS IN SLOW WAVES

For small values of the density of shortcuts p, a small-world network of integrate-and-fire neurons is quite likely to sustain persistent activity. As discussed in the preceding section, the spatiotemporal pattern of network activity in this regime is highly regular and most often periodic, despite the complex, heterogeneous topology of the network itself. As p increases, a transition takes place: more and more network configurations exhibit activity which peaks and then shuts down. Interestingly, for large enough τ_D there is an additional change in network dynamics as p increases. As shown in Fig. 12 for $\tau_D=0.16$ and 0.18, the failure probability initially increases with p, as for low values of τ_D, but it then turns downwards again as p increases further. To understand this reentrant phenomenon, we first analyze the spatiotemporal dynamics characteristic of this seemingly persistent activity at large p.

Examples of network dynamics for slow waves ($\tau_D=0.16$) are shown in Fig. 13. For values of p below or near the theoretical transition to failure [Figs. 13(a)–13(c)], the activity is similar to that shown for fast waves ($\tau_D=0.10$) in Fig. 2. However, in the reentrant regime [Fig. 13(d)], the activity is chaotic [cf. Fig. 15(a) below] and the population firing rate exhibits irregular peaks that reflect near-synchronous activity involving a large fraction of the network.

A detailed, quantitative analysis for $\tau_D=0.18$ shows that the change in behavior occurs already before the maximum of the failure probability curve. For fast waves, corresponding to small τ_D, the amplitude of the oscillations in the population activity, as measured by the standard deviation of the firing rate, was found to increase monotonically with p (cf. Fig. 6). However, for slow waves, corresponding to large τ_D, this amplitude of oscillations is nonmonotonic and decreases over the range $0.4\leqslant p\leqslant 0.6$ (Fig. 14). It is instructive to compute the spectral entropy of the population firing rate,

$$\mathcal{S}=-\sum_{\omega} P(\omega)\ln P(\omega), \tag{9}$$

which measures the number of significant peaks in the power spectrum $P(\omega)$. The spectral entropy exhibits a significant increase over the same range $0.4\leqslant p\leqslant 0.6$ [Fig. 15(b)], indicating an increase in the complexity of the dynamics. The variability of the spectral entropy across network configurations with the same density of shortcuts exhibits a broad maximum in the same range of p values, and reaches very small nonzero values (about 0.06) in the strongly chaotic regime. The detailed evolution towards chaotic dynamics,

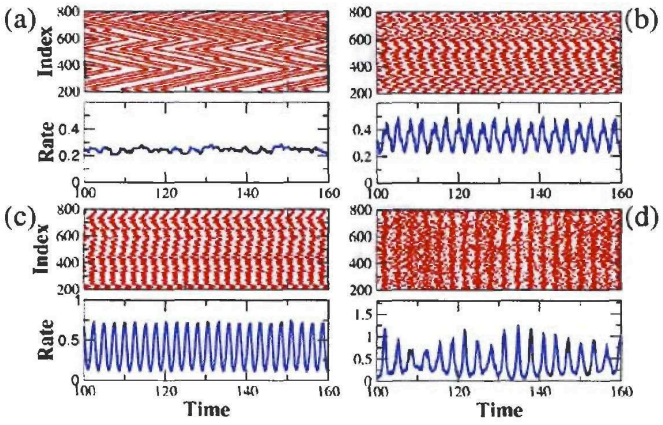

FIG. 13. Examples of network dynamics for $\tau_D=0.16$ and for different values of the density p of shortcuts. The values $p=0.01$, 0.2, 0.4, and 1.0 correspond to panels (a)–(d), respectively. Each panel shows both spiking activity and population firing rate. The reentrant activity in (d) is noisy and exhibits synchronized population bursts.

which depends on the specific configuration of shortcuts, is not investigated in further detail in this work.

What underlies the emergence of reentrant activity with increasing p? The answer lies in the interplay between network topology and the delay τ_D. The mean-field model that provides a description of the failure transition, Eq. (5), is based on the assumption that the maximal firing frequency of each neuron is limited by the recovery time $T_R^{(1)}$. However, a small-world network constructed by adding shortcuts allows for neurons to receive more than one incoming shortcut. The probability of such configurations is small at low p; in this regime, the fraction of neurons with two incoming shortcuts is given by $s_2 \sim p^2/2$,[26] which is indeed negligibly small for $p<1$. (We assume that the number of neurons with more than two shortcut inputs can be ignored and we compute the most likely rather than the expected value of the number of neurons with two shortcut inputs.) Mean-field results that ignore such configurations describe the failure transition provided it occurs at $p_{cr}<1$. However, as p approaches 1, i.e., for $|p-1| \ll 1$, the fraction of neurons with two incoming shortcuts becomes $s_2=1-\sqrt{2}/2+(p-1)/2$, which is nearly 0.3 for $p=1$. In this regime, a significant fraction of neurons is likely to receive several synaptic inputs during one cycle of network activity. Such neurons would not be constrained by the recovery time $T_R^{(1)}$, but would rather be primed to fire earlier, potentially allowing the activity to persist where it otherwise would fail. A neuron that has received n inputs at times t_r, $r=1,\ldots,n$, since its last firing has a recovery time $T_R^{(n)}$ given by

$$T_R^{(n)}(t_1,\ldots,t_n)=\ln\left(\frac{V_\infty-g_{\mathrm{syn}}\Sigma_{r=1}^{n}e^{t_r}}{V_\infty+g_{\mathrm{syn}}-1}\right). \tag{10}$$

Note that Eq. (10) reduces to Eq. (3) for $n=0$ and to Eq. (4) for $n=1$ (with $t_1=2\tau_D$). In general, $T_R^{(n)}$ depends on the specific firing times of the n neurons that provide inputs through shortcuts; these times depend in turn on the details of activity propagation in each specific network configuration. However, since integrate-and-fire neurons become increasingly sensitive to their input as time passes after their firing, the value of $T_R^{(n)}$ in Eq. (10) is bounded below by $T_{R,\min}^{(n)}$, which

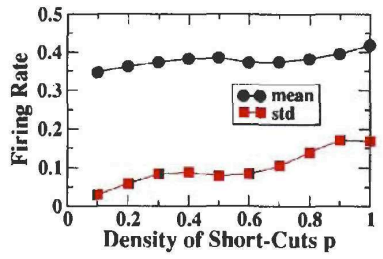

FIG. 14. Average population activity (mean firing rate) and amplitude of its oscillations (standard deviation of the firing rate) as a function of the shortcut density p. Note the nonmonotonic behavior of these curves. Data obtained as an average over those configurations (out of 200) for which the activity persists for at least 15 000 steps for $\tau_D=0.18$ and $N=1000$.

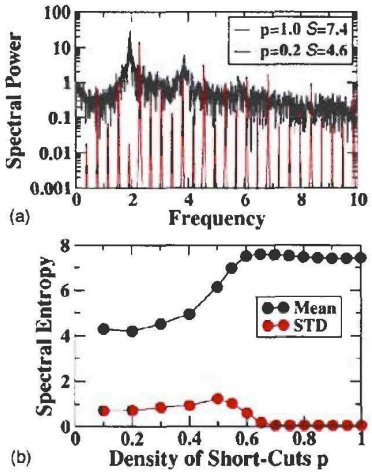

FIG. 15. Temporal complexity of activity patterns. (a) Representative power spectra for $p=0.2$ ($S=4.6$) and $p=1.0$ ($S=7.4$). (b) Spectral entropy S (mean and standard deviation across 200 configurations) for $\tau_D=0.18$ and $N=1000$, over 15 000 time steps.

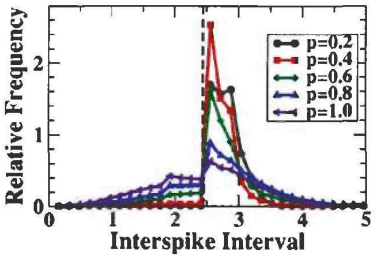

FIG. 16. Distribution of interspike intervals (ISI) for $\tau_D=0.16$ and different values of the shortcut density p. For low p, all allowed ISI are above the recovery period $T_R^{(1)}$ (dashed vertical line). For $p \geq 0.6$, multiple inputs result in ISI below $T_R^{(1)}$.

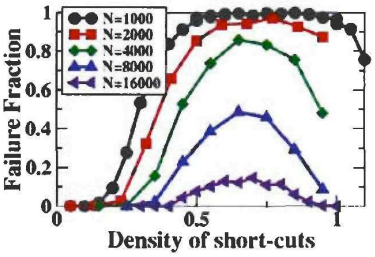

FIG. 17. Failure probability as a function of shortcut density p for $\tau_D=0.14$ and different values of system size N. Shown are averages over 400 configurations; failure probability is estimated within a finite time $T^*=28$. Note the prevalence of prolonged activity in larger systems.

occurs when all n inputs coincide at $T_{R,\min}^{(n)}$ itself. This lower bound is given by

$$T_{R,\min}^{(n)}(t_i = T_{R,\min}^{(n)}) = \ln\left(\frac{V_\infty}{V_\infty + n g_{\text{syn}} - 1}\right). \tag{11}$$

For small enough p, the interspike intervals (ISI) of almost all neurons in almost all network configurations are bounded below by $T_R^{(1)}$; this property has allowed us to calculate the time for activity to spread throughout the whole network using a purely geometric approach. For higher values of p, there may be a subset of neurons with shorter allowable ISI. However, many neurons will still receive only one input per cycle, and the frequency of their spiking activity should reflect this fact. The distribution function for the ISI shown in Fig. 16 supports this argument. Fast spiking activity with $\text{ISI} < T_R^{(1)}$ occurs appreciably only for $p \geq 0.6$, and becomes both more common and faster with increasing shortcut density. Our earlier analysis[20] showed that the spikes with $\text{ISI} > T_R^{(1)}$ occur in population bursts, with no such spikes in between bursts. In the absence of other spikes, the activity would die out during these intervals between bursts. However, the fast spiking neurons that receive multiple inputs via multiple incoming shortcuts are primed to carry over the activity during the intervals between bursts; their fast spiking sustains activity during the time needed for the slow spiking neurons to recover.

Long delays τ_D contribute in several ways to bridging the periods of low activity between bursts. For larger τ_D, the failure transition is shifted towards larger shortcut densities, thus significantly enhancing the number of neurons that receive multiple shortcut inputs. At the same time, in order to bridge the time between the return time T_A and the recovery time $T_R^{(1)}$ of the slow spiking neurons, fewer fast spiking neurons are needed if the delay is longer. Moreover, the exponential recovery of integrate-and-fire neurons towards their resting potential implies that later inputs have a stronger impact on the recovery period than earlier ones [cf. Eqs. (10) and (11)]. With increasing τ_D, all inputs are shifted to later times relative to the most recent spike of the postsynaptic neuron; this shift significantly reduces the recovery time. However, an increased delay τ_D is not necessary to establish a regime of prolonged activity. As shown in Fig. 17 for fixed delay $\tau_D=1.4$, increasing the system size from $N=1000$ to $N=16\,000$ shifts the failure transition to sufficiently large p that the number of neurons with multiple inputs is sufficient to bridge the gap between bursts of slow spiking activity, even for this shorter delay.

For low values of p, the spatiotemporal dynamics are most often periodic. In those cases the dynamics can truly be called persistent. For $p \gtrsim 1$, the chaotic nature of the dynamics precludes such a clear assessment; in fact, failure is possible even after very long times. In this regime, prolonged activity relies on bridging the quiescent period between bursts of slow spiking activity through fast spiking neurons that receive multiple shortcut inputs; it is necessary that these shortcuts are actually activated at suitable times during the quiescent part of the cycle. Thus, while in one cycle the activity during the burst may have excited such a pathway, the different activity pattern in the next burst may fail to do so; the activity could then die out. Indeed, we find that the prolonged activity characteristic of large shortcut densities eventually fails for essentially all configurations. Examples of such long-lived transients are shown in Fig. 18, where population firing rates are shown for a fixed network configuration of shortcuts at increasing values of τ_D.

The value of τ_D has a strong influence on the duration of the transient. As shown in Fig. 18, the overall trend is for the lifetime of the transient activity to increase with increasing delay (note the change in temporal scale from panel to panel). However, the actual dependence on τ_D is more subtle,

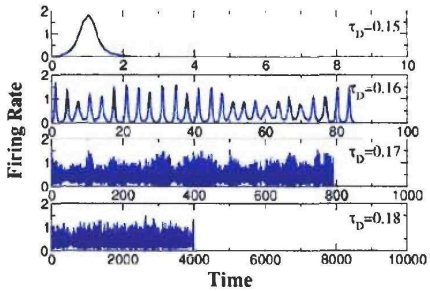

FIG. 18. Population firing rate for four values of the delay τ_D, with $p=1$. The same network configuration and the same initial activation is used in all four panels. Failure tends to occur later as τ_D increases; note the change in temporal scale from panel to panel.

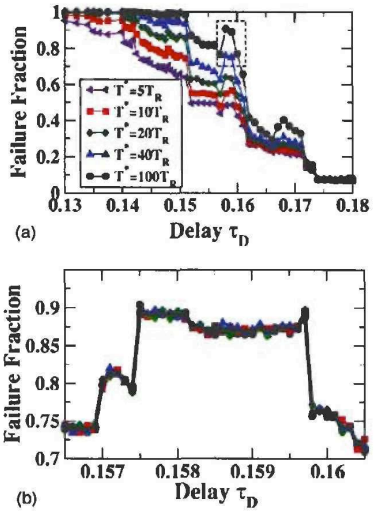

FIG. 19. (a) Failure rates for different values of the final time $T^*=5T_R$, $10T_R$, $20T_R$, $40T_R$, and $100T_R$. Shown are averages over 2000 configurations with $N=1000$ and $p=1$. (b) Enlarged view of the data within the box in (a) for $T^*=100T_R$ illustrates the fine structure in the failure rate. Shown are four runs based on averages over 8000 configurations each; the black line is the average over the four runs.

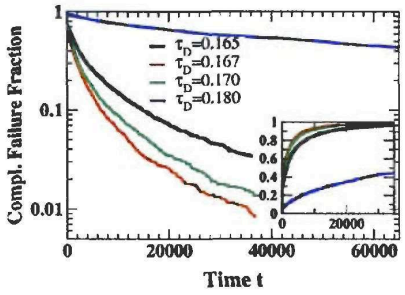

FIG. 21. (Color) Complementary failure fraction $1-\mathcal{F}$ as a function of time for different values of the delay τ_D. Note the logarithmic scale on the vertical axis. Inset: Failure fraction $\mathcal{F}$ for the same data; the vertical scale is now linear.

as shown in Fig. 19. The fraction of network configurations for which the prolonged activity fails before a specified time T^* is reached exhibits a surprising degree of structure in its dependence on τ_D. Most surprising is the finding that an increase in τ_D does not always decrease the probability of failure, but can in fact enhance it. These changes can occur over very small intervals in τ_D, as shown in the expanded window of Fig. 19(b). This fine structure is reminiscent of resonances, although these are more like antiresonances; the values of τ_D within these windows are in some sense optimal for escaping from prolonged activity. While details of the mechanism underlying this structure are not yet understood, it is clear that the dependence on τ_D reflects the significance of the ratio τ_D/T_R. This effect is illustrated in Fig. 20, which shows the dependence of the failure probability on τ_D for two network sizes: $N=500$ and $N=1000$. While the probability of failure is higher overall for the smaller network, the location of the "resonant" windows in τ_D does not show

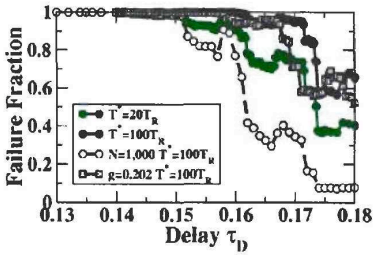

FIG. 20. Failure rates averaged over 8000 network configurations with $N=500$ and $p=1$. Data are shown for both $g_{syn}=0.200$ (circles) and $g_{syn}=0.202$ (squares). Data for $N=1000$ (cf. Fig. 19) shown for comparison.

much dependence on system size. However, even a small reduction in recovery time from $T_R=2.83$ to $T_R=2.79$, due to an increase in synaptic strength from $g_{syn}=0.200$ to $g_{syn}=0.202$, results in a significant shift of the "resonant" windows towards lower values of τ_D.

To assess whether any significant fraction of the network configurations sustains truly persistent activity, we consider the failure fraction $\mathcal{F}$ as a function of the final time T^*, so as to extrapolate to $T^*\to\infty$. The complementary fraction $1-\mathcal{F}(T^*)$ of network configurations that sustain persistent activity up to a time T^* is shown for different values of the delay τ_D in Fig. 21. As anticipated from the nonmonotonicity in Fig. 19, the fraction of failing network configurations is largest for $\tau_D=0.167$; a very rapid drop in failure rate occurs from $\tau_D=0.17$ to $\tau_D=0.18$. When considered as a function of time for fixed τ_D, the behavior of the curves in Fig. 21 indicates that the decay is not exponential.

To obtain an approximate analytic form for the failure fraction $\mathcal{F}(T^*)$, let us consider a specific network configuration for a given value of p. The duration of the activity until failure will then depend on the initial condition. In this numerical experiment we choose a specific network configuration and consider 2000 different initial conditions; to reduce the computational effort these simulations are done for a smaller system with $N=200$. The initial conditions are random and given by $V_i=V_0+\xi_i$, $i=1\ldots N$, with $V_0=0.85$ and ξ_i drawn from a uniform distribution in the interval $[-0.5, +0.5]$. A failure time is determined for the activity triggered by each initial condition. The resulting distribution of failure times exhibits exponential behavior of the form $\beta e^{-\alpha T}$ for large times; this allows the extraction of a characteristic failure time T associated with this network configuration. An exponential distribution of failure times suggests that the chaotic dynamics effectively lead to a fixed probability for the activity to die out after each population burst.

The characteristic failure time T is then computed for many network configurations of the same size and same shortcut density, leading to a distribution $\rho(T)$ of characteristic failure times, as illustrated in Fig. 22. The large-T behavior of this distribution is well fit by an exponential decay,

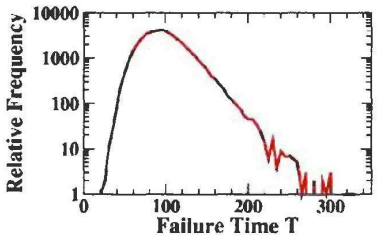

FIG. 22. Distribution of characteristic failure times T, from 50 000 network configurations with $N=200$, $p=1$, and $\tau_D=0.16$. Note the logarithmic scale on the vertical axis.

$$\lim_{T\to\infty} \rho(T) \propto e^{-\alpha T}. \tag{12}$$

The distribution $\rho(T)$ of characteristic failure times determines the average number of failures expected to have occurred by time T^*,

$$\mathcal{F}(T^*) = \int_0^{T^*} dT\rho(T)(1-\beta e^{-T^*/T}). \tag{13}$$

Inserting the asymptotic behavior identified in Eq. (12) into Eq. (13) and assuming that the prefactor β does not depend on the characteristic failure time T yields the expected failure rate for large t,

$$\mathcal{F}(t) = 1 - 2\beta\sqrt{\alpha t}K_1(2\sqrt{\alpha t}), \tag{14}$$

where $K_1(x)$ is the first-order modified Bessel function of the second kind. The asymptotic expansion of this Bessel function for large arguments leads to

$$\mathcal{F}(t) \sim 1 - \beta\sqrt{\pi}(\alpha t)^{1/4}e^{-2(\alpha t)^{1/2}}. \tag{15}$$

which displays stretched exponential behavior. The analytic result of Eq. (14) provides a good fit to the time dependence of the failure probability, as shown in Fig. 23. For $\tau_D=0.18$, the fit with $\alpha=0.67\times10^{-5}$ and $\beta=0.91$ is good over essentially the whole time range. For $\tau_D=0.165$ (inset), the fit is not quite as good; the curvature of the analytic function seems to be smaller than that of the data. A fit to the $\tau_D=0.165$ data for $t\geq3400$ yields $\alpha=0.12\times10^{-3}$ and $\beta=0.64$. This fit (blue dotted line) underestimates the data for long times. A fit with $\alpha=0.10\times10^{-3}$ and $\beta=0.54$ (red dashed line) reduces the underestimation at long times, but is not as good for smaller times. In any case, the analytic results of Eqs. (14) and (15) indicate the existence of very long transients of prolonged activity. This activity will always eventually fail; $\mathcal{F}(t)\to1$ as $t\to\infty$.

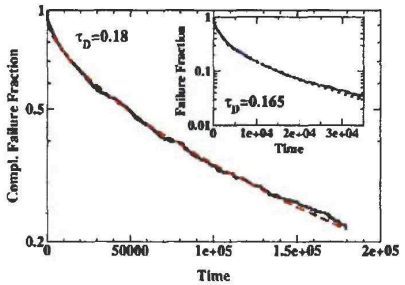

FIG. 23. (Color) Complementary failure fraction $1-\mathcal{F}$ as a function of time for $p=1$ and $\tau_D=0.18$ (inset for $\tau_D=0.165$). Dashed red and dotted blue lines are fits to Eq. (14). Note the logarithmic scale on the vertical axis.

V. CONCLUSION

In this paper we have used a minimal model to study the influence of network topology on the dynamics of coupled excitable elements. The network consists of a ring of locally connected elements; the connectivity is enhanced through random shortcuts that connect arbitrarily distant elements. Since our goal is to capture gross features of cortical connectivity, we assume that these shortcuts provide only unidirectional connections. This is in contrast to the bidirectional shortcuts that are appropriate for modeling epidemic propagation[19] or regular diffusive processes.

The dynamics of the system exhibit three distinct regimes, depending on the density of shortcuts and the speed of the waves that propagate through the network. For low but nonzero density of shortcuts, activity persists for essentially all network configurations when triggered by the initial excitation of a single neuron. This activity is predominantly periodic, and the mean firing rate of these persistent states shows only little dependence on the wave speed or the density of shortcuts once $p\geq0.05$. This firing rate is quite close to the maximal firing rate allowed by the recovery period of the neurons.

The recovery period is not to be confused with an absolute, intrinsic refractory period; rather, it is the time from one spike until the membrane potential has recovered to a value such that a single synaptic input of specified strength will suffice to trigger a new spike. This recovery period can be much longer than the absolute refractory period; this phenomenon has been observed in neurons that exhibit a slow after-hyperpolarization that underlies the slow oscillations (<1 Hz) observed *in vivo* in cat[31] and in cortical slices of ferret.[32] There, the recovery period induced by after-hyperpolarization can last as long as a few seconds. Of relevance to the dynamics investigated here is the time associated with the propagation speed of such slow oscillations over the whole network; specifically, the dependence of this propagation time on network connectivity. This dependence has been studied in cortical models[33,34] that do not incorporate shortcuts but use other mechanisms to control and vary network connectivity: either a variable spatial width of the Gaussian distribution that controls the probability that two neurons are connected,[34] or a trimodal probability distribution that captures a type of patchy connectivity in the cortex.[33] As expected, the speed of activity propagation was found to increase with increased connectivity; it was conjectured that this connectivity dependence underlies the large difference in propagation times observed for slow waves in olfactory cortex and neocortex.[34]

For low density of shortcuts, the persistent activity triggered by a localized excitation is periodic. However, the overall dynamical behavior of the system can be quite com-

plex due to the coexistence of a large number of stable solutions for a given network configuration. Whether the number of attractors grows as fast with system size as it does for globally coupled oscillator networks is not known at this point. In the case of global coupling, the permutation symmetry leads to a factorial growth of the number of attractors and to attractor crowding;[27] however, this permutation symmetry is broken in the small-world topology. So far as we have been able to investigate the dynamics of increasingly large networks, we have not been able to reach saturation of the number of attractors evoked through different initial conditions. The mechanism underlying this large number of attractors is not yet apparent; however, it is clear that noise will induce switching between these different attractors.[26]

As the density of shortcuts is increased, the number of network configurations that can sustain persistent activity decreases, until persistent activity is essentially no longer possible. For fast waves, the transients after a localized excitation consist of a single population burst followed by activity extinction. For slow waves, the crossover to complete failure occurs at larger shortcut densities than for fast waves. In addition, slow waves can exhibit exceedingly long transients that comprise thousands of population bursts. This activity eventually fails; the failure times for different network configurations at a fixed density of shortcuts follow an exponential distribution, which leads to a stretched exponential distribution for the expected probability of failure as a function of time. The mechanism responsible for these long transients is crucially dependent on the existence of pathways that bridge the quiescent periods between population bursts. These pathways are supported by the topology of the small-world network; this mechanism is thus expected to differ from the one relevant for dilute random networks of pulse-coupled oscillators.[35]

Another quantity of interest is the fraction of network configurations that has already failed by a specified time T^*. This quantity exhibits an overall decreasing trend with decreasing wave speed, or increasing recovery time τ_D. In addition to this decreasing trend, this quantity exhibits an intricate fine structure that includes sharp, resonance-like increases of the failure fraction with decreasing wave speeds. A naive argument supports the decreasing trend, but not the sharp resonances; a decrease in wave speed is likely to allow for additional shorter loops to contribute to the activity, and thus enhance the chances for persistence. However, the existence of sharp increases in failure probability indicates that the activation of one such loop can block the propagation of activity through previously active loops, and thus induce failure. While it is clear that such a switching between loops can occur with increasing τ_D, the mechanism that underlies these increased failures is not yet fully understood.

The crossover to failure, which can be understood in detail based on an analytic mean-field result for the effective size of these idealized small-world networks, provides the basis for understanding a number of recent studies of related but more complex neural network models.[4,22,23]

In Ref. 22, the connection between network connectivity and epilepsy in the hippocampus was investigated by considering small-world networks of three different types of neurons: noisy and leaky integrate-and-fire neurons, stochastic Hodgkin-Huxley cells, and Poisson spike-train cells. As parameters such as synaptic strength, number of synapses per neuron, and proportion of local versus shortcut connections, were varied, the network displayed dynamical behaviors described as "normal," "seizing," and "bursting." For low shortcut density, noise-driven activity was found to remain at a low level; this pattern of activity was associated with normal behavior. With increasing shortcut density, the level of activity triggered by a noise-driven event strongly increased, due to the recruitment of a vastly larger number of neurons. This pattern of activity was likened to seizing behavior. According to our analysis, this regime corresponds to patterns of connectivity that support persistent activity. Yet further increases in the shortcut density were found to induce bursting dynamics, characterized by irregular bursts involving a large fraction of all neurons, separated by quiescent periods. This pattern of activity corresponds in our analysis to network configurations associated with failure, for which each noise-triggered event leads to a population burst that brings essentially all neurons into their recovery period.

In Ref. 23, the role of network connectivity in sustaining population bursting activity was investigated by considering a small-world network of Morris-Lecar neurons. Activity was initiated through a localized set of pacemaker neurons. It was found that in the presence of shortcuts, network activity builds up over several driven cycles into bursts that involve a large fraction of neurons firing within a small time window. Both the time needed to build up such bursts and the time between them were found to decrease with increasing shortcut density. The appearance of repeated bursts is related to the failing configurations discussed here. As expected from our analysis, bursting behavior was supplanted by persistent activity when the wave speed was reduced (cf. increasing τ_D in Fig. 12). The slow buildup towards bursting activity observed in Ref. 23 appears to be specific to the Morris-Lecar neurons used in their model.

In Ref. 4, a 1:20 functional model of the rat dentate gyrus was constructed to investigate the functional consequences of two types of changes in network architecture that take place concurrently during epileptogenesis: loss of hillar mossy cells and sprouting of granular cell axons. The removal of mossy cells resulted in a massive reduction in the total number of connections, but this effect was to some extent compensated by an increase in local connectivity due to spatially restricted sprouting of granular cell axons. Surprisingly, as long as mossy cells were not almost fully eliminated, they continued to provide intermediate and long-range connections onto granule cells, thus preserving the short network diameter characteristic of small-world connectivity. The hyperexcitability that arises from these structural changes corresponds in our analysis to the sustained propagation of fast waves in the presence of a small density of shortcuts.

ACKNOWLEDGMENTS

We gratefully acknowledge the NSF support through Grant Nos. DMS-0309657 and DMS-322807, as well as the IGERT program "Dynamics of Complex Systems in Science

and Engineering" (DGE-9987577) (H.R., A.R., S.M.); EU support under Grant No. MRTN-CT-2004-005728 (S.M.) is also gratefully acknowledged. A.R. acknowledges funding by Marie Curie grant 022242.

[1]R. Albert and A. L. Barabasi, Rev. Mod. Phys. **74**, 47 (2002).
[2]M. E. Newman, SIAM Rev. **45**, 167 (2003).
[3]O. Shefi, I. Golding, R. Segev, E. Ben-Jacob, and A. Ayali, Phys. Rev. E **66**, 021905 (2002).
[4]J. Dyhrfjeld-Johnsen, V. Santhakumar, R. J. Morgan, R. Huerta, L. Tsimring, and I. Soltesz, J. Neurophysiol. **97**, 1566 (2007).
[5]M. Barahona and L. M. Pecora, Phys. Rev. Lett. **89**, 054101 (2002).
[6]H. Hong, M. Y. Choi, and B. J. Kim, Phys. Rev. E **65**, 026139 (2002).
[7]T. Nishikawa, A. E. Motter, Y.-C. Lai, and F. C. Hoppensteadt, Phys. Rev. Lett. **91**, 014101 (2003).
[8]P. C. Bressloff, J. Math. Biol. **40**, 169 (2000).
[9]P. C. Bressloff, Physica D **155**, 83 (2001).
[10]D. Golomb and G. B. Ermentrout, Phys. Rev. Lett. **86**, 4179 (2001).
[11]R. D. Traub, D. Schmitz, J. G. Jefferys, and A. Draguhn, Neuroscience **92**, 407 (1999).
[12]T. J. Lewis and J. Rinzel, Network Comput. Neural Syst. **11**, 299 (2000).
[13]T. J. Lewis and J. Rinzel, Neurocomputing **38**, 763 (2001).
[14]M. Perc, New J. Phys. **7**, 252 (2005).
[15]L. F. Lago-Fernández, R. Huerta, F. Corbacho, and J. A. Sigüenza, Phys. Rev. Lett. **84**, 2758 (2000).
[16]L. F. Lago-Fernández, F. J. Corbacho, and R. Huerta, Neural Networks **14**, 687 (2001).
[17]D. R. Paula, A. D. Araujo, J. S. Andrade, H. J. Herrmann, and J. A. Gallas, Phys. Rev. E **74**, 017102 (2006).
[18]A. R. Carvunis, M. Latapy, A. Lesne, C. Magnien, and L. Pezard, Physica A **367**, 595 (2006).
[19]M. Kuperman and G. Abramson, Phys. Rev. Lett. **86**, 2909 (2001).
[20]A. Roxin, H. Riecke, and S. A. Solla, Phys. Rev. Lett. **92**, 198101 (2004).
[21]D. J. Watts and S. H. Strogatz, Nature (London) **393**, 440 (1998).
[22]T. I. Netoff, R. Clewley, S. Arno, T. Keck, and J. A. White, J. Neurosci. **24**, 8075 (2004).
[23]J. Shao, T. Tsao, and R. Butera, Neural Comput. **18**, 2029 (2006).
[24]M. Tinsley, J. X. Cui, F. V. Chirila, A. Taylor, S. Zhong, and K. Showalter, Phys. Rev. Lett. **95**, 038306 (2005).
[25]A. J. Steele, M. Tinsley, and K. Showalter, Chaos **16**, 015110 (2006).
[26]A. Roxin, Ph.D. thesis, Northwestern University (2003).
[27]K. Wiesenfeld and P. Hadley, Phys. Rev. Lett. **62**, 1335 (1989).
[28]M. E. Newman, C. Moore, and D. J. Watts, Phys. Rev. Lett. **84**, 3201 (2000).
[29]M. E. Newman and D. J. Watts, Phys. Rev. E **60**, 7332 (1999).
[30]T. Petermann and P. de Los Rios, Phys. Rev. E **73**, 026114 (2006).
[31]F. Amzica and M. Steriade, J. Neurophysiol. **73**, 20 (1995).
[32]M. V. Sanchez-Vives and D. A. McCormick, Nat. Neurosci. **3**, 1027 (2000).
[33]A. Compte, M. V. Sanchez-Vives, D. A. Mccormick, and X. J. Wang, J. Neurophysiol. **89**, 2707 (2003).
[34]M. Sanchez-Vives and A. Compte, Lect. Notes Comput. Sci. **3561**, 133 (2005).
[35]A. Zumdieck, M. Timme, T. Geisel, and F. Wolf, Phys. Rev. Lett. **93**, 244103 (2004).

Neurobiology of Disease

Epilepsy in Small-World Networks

Theoden I. Netoff,[1,3] Robert Clewley,[2,3] Scott Arno,[1,3] Tara Keck,[1,3] and John A. White[1,3]

[1]Department of Biomedical Engineering, [2]Department of Mathematics and [3]Center for BioDynamics and Center for Memory and Brain, Boston University, Boston, Massachusetts 02215

In hippocampal slice models of epilepsy, two behaviors are seen: short bursts of electrical activity lasting 100 msec and seizure-like electrical activity lasting seconds. The bursts originate from the CA3 region, where there is a high degree of recurrent excitatory connections. Seizures originate from the CA1, where there are fewer recurrent connections. In attempting to explain this behavior, we simulated model networks of excitatory neurons using several types of model neurons. The model neurons were connected in a ring containing predominantly local connections and some long-distance random connections, resulting in a small-world network connectivity pattern. By changing parameters such as the synaptic strengths, number of synapses per neuron, proportion of local versus long-distance connections, we induced "normal," "seizing," and "bursting" behaviors. Based on these simulations, we made a simple mathematical description of these networks under well-defined assumptions. This mathematical description explains how specific changes in the topology or synaptic strength in the model cause transitions from normal to seizing and then to bursting. These behaviors appear to be general properties of excitatory networks.

Key words: epilepsy; networks; small-world networks; seizures; computational modeling; interictal burst

Introduction

Epilepsy is characterized by two electrographic behaviors: interictal bursts of activity that last ~100 msec and "seizures" that last from seconds to minutes (Steriade, 2003). In slice models of epilepsy, bursts and seizures can be elicited in different regions of the hippocampus bathed in 4-aminopyridine (4-AP). Bursts originate in region CA3 of hippocampus (Chesnut and Swann, 1988), whereas seizures originate in region CA1 (Netoff and Schiff, 2002). 4-AP increases excitability and effective synaptic strength (Perreault and Avoli, 1989); however, epileptiform behavior can be induced in slices through a variety of methods (Traub and Miles, 1991), suggesting that the cause of these behaviors is a general property of the network.

Traditionally, epilepsy is viewed as a disease of "hypersynchronous" neuronal activity (Penfield and Jasper, 1954; Steriade, 2003). Evidence from hippocampal slices shows that bursts in CA3 are caused by neuronal activity that is synchronous on a fine time scale (<10 msec); however, neuronal activity during slice seizures in CA1 is not synchronous (Netoff and Schiff, 2002; Van Drongelen et al., 2003). The most notable difference between the hippocampal regions is that CA3 has more recurrent synaptic connections than CA1. Staley et al. (1998) hypothesized that bursts originate in region CA3 because the network activates quickly, via recurrent excitation, depleting the primary glutamate stores of the neurons and thus shutting down the network.

Our goal in this study was to use computational models to explore how epileptiform behaviors relate to the connectivity of the underlying networks. Our operating hypothesis for CA3 bursts is similar to that of Staley et al. (1998), except that our models rely on generally defined neuronal "refractoriness" to terminate burst activity. Refractoriness may arise via a number of mechanisms, including synaptic depletion, inhibition, or voltage-dependent properties in postsynaptic cells. In the CA1, which has less recurrent excitation, the activity spreads slower. Thus, an excitable pool of CA1 neurons is always available, leading to sustainable seizure-like activity. To test these hypotheses, we simulated networks intended to mimic regions CA3 and CA1. We used "small-world" network topologies, in which the majority of connections between cells are "local," but a few cells have "long-distance" connections (Watts and Strogatz, 1998; Watts, 1999). Small-world networks were used because they are simple, flexible, and reminiscent of the connectivity patterns of networks in the brain. As connectivity in the networks was changed, we observed activity resembling epileptiform behaviors seen in slice models. Networks with large numbers of long-distance connections were more prone to generating self-terminating bursts. Additionally, our results suggest that the greater level of interconnectivity in CA3 may be responsible for its tendency to burst rather than seize. Results were independent of the specific neuronal model (Poisson, integrate-and-fire, Hodgkin-Huxley) used in the simulations. We derived a reduced mathematical description of the networks that helped us to describe the conditions under which networks transition from "normal" to "seizing" to "bursting." Although this model provides only a heuristic description of the slice behavior, it demonstrates how epileptiform behaviors may depend on specific physical parameters.

Received Dec. 18, 2003; revised July 29, 2004; accepted July 30, 2004.

This work was supported by National Institutes of Health Grants R01-NS34425 and R01-MH43510 and National Science Foundation Grant DMS-0211505. We thank Nancy Kopell, Sid Redner, Steven J. Schiff, Corey Acker, Alan Dorval, and G. Bard Ermentrout for valuable discussions in the development of this work. The reviewers of this paper made a number of suggestions that improved it dramatically.

Correspondence should be addressed to Theoden I. Netoff, Boston University, Department of Biomedical Engineering, 44 Cummington Street, Boston, MA 02215. E-mail: tnetoff@bu.edu.

DOI: 10.1523/JNEUROSCI.1509-04.2004

 0270-6474/04/248075-09$15.00/0

Materials and Methods

Structure of the network and connectivity. We generated simple network models of excitatory neurons in hippocampus. To keep the number of free parameters manageable, to more easily constrain activity to spread in a controlled manner, and to eliminate the effects of boundary conditions, we restricted our analyses to one-dimensional "rings" of neurons. Because organization of the synaptic connections within cortical regions is neither a lattice of nearest-neighbor connections nor completely randomly connected (Mountcastle, 1997; Gonzalez-Burgos et al., 2000; McCormick and Contreras, 2001), we used a simple method to construct networks that lie between these two extremes. We began with a model in which each neuron is connected to a specific number k of its nearest neighbors and then randomly disconnected a proportion ρ of the synaptic connections and reconnected these synapses to a randomly chosen postsynaptic cell. This method of network construction leads to small-world networks (Watts and Strogatz, 1998; Watts, 1999), in which most connections made by a given presynaptic neuron are local, but an important few can spread activity over long distances. An illustration of networks with varying amount of long-distance connections is given in Figure 1. In the network in Figure 1*a*, each "node" represents a neuron. The ring of neurons is connected in a perfect "lattice" ($\rho = 0$), with each cell connected to its four nearest neighbors. Figure 1, *b* and *c*, represents networks increasing values of ρ. These are small-world networks because they include a preponderance of local, regular connections but a small number of long-distance connections, which greatly reduce the number of synaptic steps required to connect any pair of neurons in the network.

The anatomy of our small-world networks is characterized by three free parameters: network size (N), the number of synaptic connections per neuron (k), and the proportion of randomly made long-distance connections (ρ). For most simulations, we used $N = 3000$, approximately corresponding to the smallest population size within which epileptiform activity is seen in the hippocampus (Fox et al., 2001). In some simulations, we used $N = 24{,}000$ to examine the generality of our results. We examined many values of k but focused our attention on networks with 1% total connectivity ($k = 30$ for $N = 3000$) to represent region CA1 and networks with 3% total connectivity ($k = 90$ for $N = 3000$) to represent region CA3. Both k values are overestimated as follows: excitatory to excitatory coupling in region CA3 is closer to 2% (MacVicar and Dudek, 1980) and for region CA1, it is <1%. Because the numbers of local versus long-distance connections are unknown in hippocampus, we treated ρ (the proportion of random connections in the network) as an explicit free parameter that we varied from 0 to 1. ρ is a particularly important parameter for these models, because it controls the rate at which local "waves" of activity give rise to new waves at distant locations in the network.

Model neurons and synapses. We ran simulations using three different types of model neurons: noisy and leaky integrate-and-fire neurons, stochastic Hodgkin–Huxley cells (Chow and White, 1996), and a Poisson spike-train cell model that is equivalent to the other models in terms of first-order interspike interval statistics. The integrate-and-fire model is a regular leaky integrate-and-fire model with a stochastic component, given by

$$\frac{dV}{dt} = V_{\text{leak}} - V + I_{\text{syn}} + \xi,$$

where V indicates the membrane potential, V_{leak} is the resting potential of the neuron, I_{syn} is the synaptic input (described in a subsequent paragraph), and ξ is the stochastic component (white noise of sufficient variance to generate spontaneous activity at a target rate). The neuron fires when V reaches a threshold, resulting from noise or when a synaptic current is injected into postsynaptic neurons. The neuron is then reset to zero, and all synaptic inputs are blocked for an absolute "refractory" period of time τ_R (see below for additional information on refractoriness).

The stochastic Hodgkin–Huxley model is a conductance-based model, which is described in detail by Chow and White (1996). Parameters were as in the original 1952 study, except that sodium channels were modeled as discrete, stochastic elements. The Langevin method was used to describe the effects of channel noise (Chow and White, 1996). In this model, membrane noise causes the membrane potential to fluctuate and occasionally causes the neuron to fire spontaneously. The number of sodium channels was "tuned" to 3375 to match a target average spontaneous firing rate (see below).

Synaptic currents for the integrate-and-fire and stochastic Hodgkin–Huxley models were calculated using a double exponential function $I_{\text{syn}} = A(e^{-t/\tau_s} - e^{-t/\tau_f})(V_{\text{syn}} - V)$, where A is the synaptic amplitude, t is the time since synaptic input occurred, τ_s and τ_f are the slow and fast decay rates, respectively, and V_{syn} is the reversal potential of the synapse (Bower and Beeman, 1995).

To construct the Poisson model, we used Matlab (MathWorks, Natick, MA) to select spike times from a Poisson process. Synaptic inputs for this model were simulated in the following way: in response to the arrival of a presynaptic spike, the postsynaptic cell has a probability of immediately firing, where the probability for a single synaptic input was set to 2.5%. We set the probability of firing after two or more simultaneous synaptic inputs to 1. If the cell does not immediately fire in response to an input, then it uses the spike time previously drawn from the Poisson distribution.

All models were adjusted to have an absolute refractory period, τ_R (after spiking), 10 times longer than the synaptic delay, τ_t. This allows the active population to travel 10 steps before the neurons recover. For the Poisson model, the synaptic delay was set at 3.7 msec and a refractory time of 36 msec, whereas in the integrate-and-fire model, the synaptic delay was 2.8 msec and the refractory time was 28 msec. The Hodgkin–Huxley model had a synaptic delay dependent on the distance between the neurons with a 1 msec delay between the local cells and up to 5 msec for long-distance connections. An absolute refractory time was 36 msec and was set to behave qualitatively similarly to the other models. The one exception is the network simulation with 24,000 neurons where the refractory time was 28 msec and the synaptic delay was 2 msec, which was necessary to allow enough time for the entire network to be activated before the first cells recovered. The refractory period can be generated by many mechanisms, either presynaptic or postsynaptic, and we leave this undetermined. The important factor is that the refractory time is on the order of the time it takes activity to spread throughout the network in the bursting regimen; otherwise, the activity will re-enter and a clean transition to bursting will not occur. We also matched all models so that they had an approximately exponential interspike interval distribution and firing probability of 0.0315 spikes/sec. In most simulations, synaptic efficacies were set in all models such that single inputs caused postsynaptic action potentials 2.5% of the time, and two simultaneous inputs led to postsynaptic firing with probability of firing approximately equal to one (assumed to be exactly one in our later theoretical analysis). For the 24,000 cell simulations (see Fig. 3), we compensated for the eightfold increase in network size with a 20-fold decrease in synaptic weight. As successfully predicted by our reduced theoretical model, this change kept the same overall rate of wave generation, leading to results (see Fig. 3).

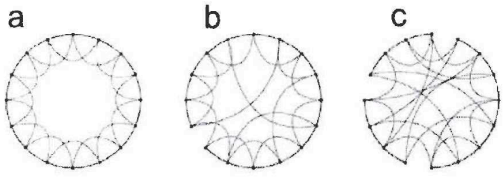

Figure 1. Small-world network. *a*, Networks of neurons are generated in which all cells are only coupled to their nearest neighbors (4 in this case). *b*, To generate small-world networks, small numbers of connections are broken and rewired to make long-distance connections at random locations. Long-distance connections reduce the number of synapses between any pair of neurons in the network. *c*, As more long-distance connections are added, the network loses the property that most connections are local, and the network looks much more random. We find a range of normal and epileptiform behaviors in the small-world network regimen, where few connections are necessary to connect any pair of the neurons, but local connections still predominate.

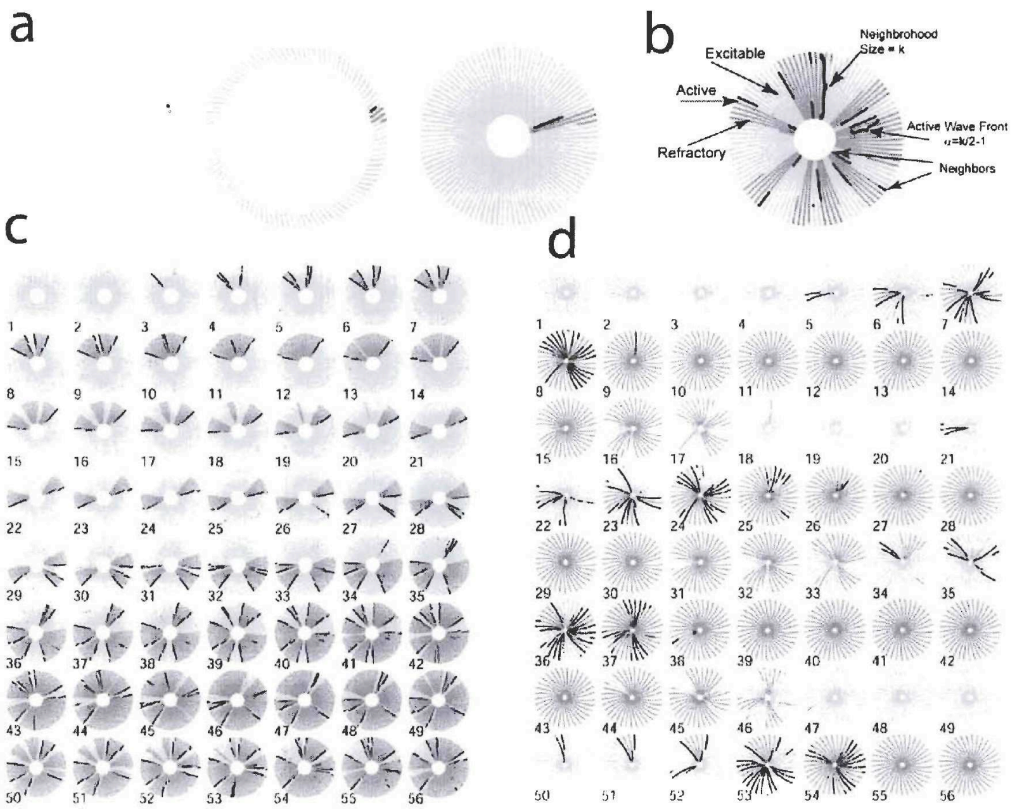

Figure 2. Bursting and seizing behaviors as the number of long-distance connections are changed. *a*, The ring contains N neurons, each of which are connected to k, mostly local neighbors (left). To visualize the activity of this large network, we color coded each point according to the state of the neuron and pulled every kth point in the ring toward the center to make a spoke. Therefore, a neuron in the center of a spoke is connected to all the neurons in the spoke, assuming that all synaptic connections are local. A neuron at the end of the spoke is connected to half of the neurons on the spoke and half of the neurons on the opposite end of the next spoke. This results in a plot of the ring that resembles a slinky. *b*, An illustrative temporal snapshot of network activity, with $N = 3000$, $k = 30$ synapses per neuron (i.e., 1% network connectivity), and $p = 0.1$. Light gray dots represent excitable neurons, black dots are firing neurons, and dark gray dots are refractory neurons. The wave front size stabilizes to approximately half the size of the local neighborhood k and is followed by a refractory tail. This tail is determined by how many steps the wave front can travel before the neurons begin to recover. *c*, Successive frames from a movie of seizing activity, with $N = 3000$, $k = 30$, and $p = 0.1$ (i.e., that 10% of synapses have been rewired). The frame rate is 250 Hz, corresponding to approximately two synaptic time delays; therefore, the active waves appear twice as large (in space) as their actual size. Spontaneous background activity generates a cascade of activity, which stabilizes into two traveling waves (frames 5–25). These traveling waves generate other waves in the network through the long-distance connections (e.g., frames 26, 31, 34). Eventually, waves start to meet and annihilate each other (e.g., frames 4, 33, 43). This network attains equilibrium when the new waves are generated at the same rate that the waves annihilate each other. *d*, Still frames from a movie of bursting activity ($N = 3000$; $k = 90$; $p = 0.1$). In this network, the number of long-distance connections causes waves to generate new waves faster than the waves annihilate each other. This results in all of the neurons firing in the network, all of the neurons becoming refractory, and the activity in the network shutting off. Movies of network activity can be seen at: http://www.bu.edu/ndl/people/netoff/SWN/JNeurosciSupplement.html.

Results

Basic properties of propagating activity

In all three types of networks (Poisson, integrate-and-fire, and stochastic Hodgkin–Huxley), we observed qualitatively similar behaviors. Networks are quiescent at first, but eventually a spontaneous action potential in one neuron initiates activity in two neurons with common local postsynaptic targets. Because convergence of two simultaneous inputs fires postsynaptic cells in these networks with probability near one, this event generates two waves that travel in opposite directions around the ring. With few long-distance connections, a small number of waves sweeps across the network. This results in a small, stable amount of activity. With more long-distance connections, existing waves frequently give rise to new waves in distant locations, and network activity transitions to sustained high activity, which we liken to seizures. Figure 2*c* illustrates still frames from a movie of an ongoing seizure (see Fig. 2, *a* and *b*, for an explanation of the display method). With a large enough number of long-distance connections (Fig. 2*d*), we observed bursts in which the majority of the network fired synchronously and then became refractory. Movies of seizures and bursts can be seen at http://www.bu.edu/ndl/people/netoff/SWN/JNeurosciSupplement.html. As we show, transition points between normal, bursting, and seizing vary according to the number of long-distance connections, network size, synaptic strength, and number of synapses per neuron.

Dependence on model parameters

Figure 3 illustrates how network activity depends on the proportion of long-distance connections (ρ), which controls the spread from local activity to distant portions of the network. Each neuron is coupled, predominantly locally, to 1% (Fig. 3, left panels) (approximately corresponding to connectivity in region CA1) or 3% (right panels) (approximately corresponding to region CA3) of the rest of the network. The top six panels (Fig. 3*a–f*) show traces of population activity versus time for specific cases. Normal activity is characterized by a low sustained population firing rate. Seizing activity is characterized by significantly higher, sustained firing rates with some evidence of coherence. Bursting activity is characterized by network activity that rises and falls rapidly and coherently.

The middle set of panels in Figure 3 show time-averaged population firing rates as a function of ρ, the proportion of long-distance connections. *a–f* in Figure 3 correspond to the examples from the top six traces. For the CA1 model, the slope of the population firing rate versus ρ becomes steep at approximately $\rho = 0.01$. We define this point as the transition from normal firing to seizing in the network. Population oscillations, with a period close to the neuronal refractory period, are seen in parts of the seizing region (Fig. 2*b*,*e*). For the CA3 model, the transition to seizing occurs at $\rho = 4 \times 10^{-4}$. As more long-distance connections are added to the network, coherent bursting begins. Interestingly, the onset of bursting, which occurs at $\rho = 0.01$ for the CA3 model and $\rho = 0.2$ for the CA1 model, leads to a marked decrease in population activity. The period of the bursting is erratic, because after a burst, there is no residual activity in the network, implying that the next burst is triggered only at the rate of the random spontaneous background activity. These results suggest that the observed phenomena are independent of the individual neuron models used in the network (Poisson, integrate-and-fire, stochastic Hodgkin–Huxley).

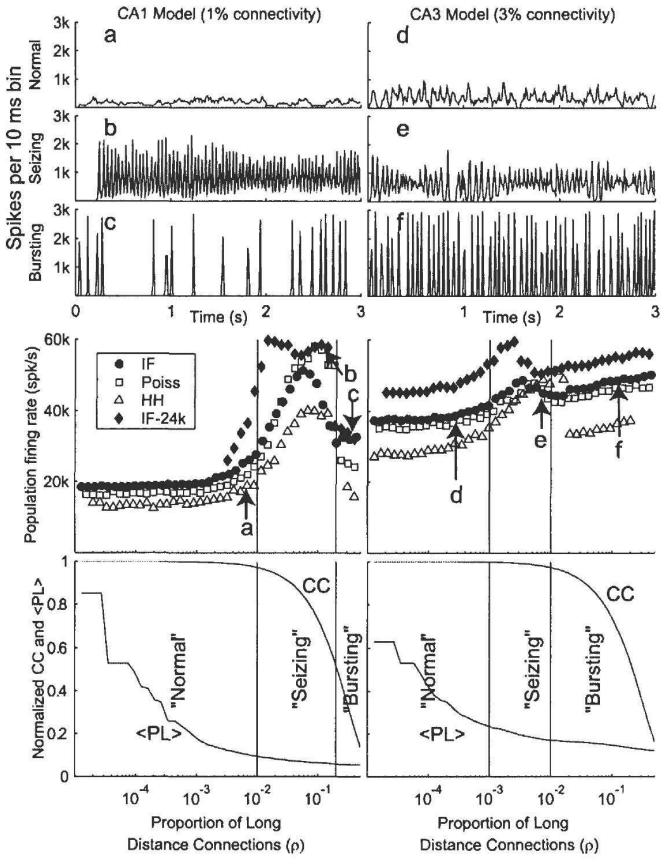

Figure 3. Transition from normal → seizing → bursting behavior as a function of the number of long-distance connections (ρ). The left column shows the results from the CA1 model with $N = 3000$ and $k = 30$, whereas the right column shows the results from a CA3 model with $N = 3000$ and $k = 90$. At the top are three examples of data (taken from a Poisson-simulated network) for normal, seizing, and bursting, showing the count of neurons that fired in a 10 msec time bin. Middle panels illustrate the total population activity for Poisson (Poiss), noisy leaky integrate-and-fire (IF), and stochastic Hodgkin–Huxley (HH) simulations with the examples from above indicated by *a–f*. Vertical bars indicate boundaries between normal, seizing, and bursting as identified by eye from the time traces of population activity from the Poisson model. Simulations of IF network with 24,000 neurons and reduced synaptic strength are displayed as well (IF-24k). These networks show qualitative behaviors similar to the 3000 neurons. The bottom panels illustrate the normalized clustering coefficients and mean path length between neurons in the network as the proportion of long-distance connections in the network (ρ) is increased. The left side of these graphs indicates a network topology in which the ring of neurons has only local connections; the right side indicates a nearly randomly connected network.

The integrate-and-fire network was also scaled up eightfold, to 24,000 neurons, while decreasing synaptic strength 20-fold to balance the excitation in the network. (The formula for determining this decrease in synaptic strength came from our reduced model, which is discussed below.) This manipulation results in very similar transitions from normal to seizing to bursting behavior (Fig. 3, filled diamonds), indicating that these results do not depend on network size. Very similar results (data not shown) were also seen in 24,000 member Poisson-process networks with downsized synapses, further indicating that these results depend critically on connectivity but not on other details.

The bottom two panels in Figure 3 show the normalized clustering coefficient (CC) and mean path length (<PL>) plotted versus ρ. The clustering coefficient is a measure of how likely it is that two interconnected neurons both make connections to the same neighbor. In particular, it is the average probability that the number of observed overlap in neighbors would occur by chance if the network had been connected randomly. Mean path length is the average number of "degrees of separation" between two randomly chosen neurons. It is calculated by averaging the measured distance between all pairs in the network. Both measures decrease with increasing proportion of long-distance connections ρ, but an intermediate value of ρ corresponds to the so-called small-world regimen where the clustering coefficient is high and the

mean path length is low. The regimen of seizing activity in the CA1 model corresponds with this small-world regimen. The beginning of the bursting regimen corresponds with the drop in clustering coefficient, which signals the transition of the network from a small world to a random graph. As indicated by comparing the right and left columns in Figure 3, having a larger number of connections leads to bursting at lower values of ρ.

Scaling relationships and the reduced model of propagating activity

Propagating activity in simulated networks has a number of stereotypical characteristics that allow us to represent it accurately using a reduced model. First, because the time needed for suprathreshold inputs to activate the model neurons is small compared with the synaptic delay time, the synaptic delay sets the amount of time required for wave fronts to propagate from one group of active neurons to another. Consequently, the network evolves in approximately discrete time steps, corresponding to the synaptic delay. Second, assuming a nearly regular lattice (i.e., that the number of long-distance connections is small relative to N), the wave front size, α, is just less than half the neighborhood size: $\alpha = k/2 - 1$. The division by 2 comes from the fact that the wave spreads in both directions (unless one set of cells is refractory); subtracting 1 from the total removes the neuron that only receives a single synaptic input from the active neurons. Third, following each wave is a wake of refractory neurons, approximately the size $\alpha R = \alpha \times \tau_R/\tau_d$, where τ_R denotes the refractory time of each neuron, and τ_d denotes the synaptic delay. This equation defines the number of time steps that a neuron remains refractory, which we have denoted R. Finally, knowing the number of waves, their size, and their wake size, it is straightforward to calculate the characteristics of propagation and the probability of emergence of a new wave per time step, as well as the probability per unit time that two waves will collide and thus annihilate. Thus, we should be able to construct a discrete time, birth-and-death process describing activity in the ring network.

Let w_i denote the number of active waves at time step i. We define the number of new waves that will begin spontaneously in one time step to be $S_i = se_ip_2$. Here, s is the probability that any given neuron will fire in that time, which we set at $s = 0.0315 \times \tau_d$, where 0.0315 is the spontaneous spike rate per second. e_i is the number of excitable neurons present in the network at time i. p_2 is the probability that two or more neurons fire in response to the firing of the same presynaptic neuron. The dependent variable p_2 can be calculated from the binomial theorem using synaptic strength p_1 (which we define as the probability that firing of a single presynaptic cell induces an action potential in a given postsynaptic cell) and the number of synapses per neuron k: $p_2 = 1 - (1 - p_1)^k - kp_1(1 - p_1)^{k-1}$. In our reduced model, if two such neurons in a neighborhood fire, we will assume that a traveling wave will be initiated with probability of exactly one (the relative frequency of such an event was observed to be ~1 in the simulations), with wave front size exactly equal to α. This assumption holds true for our 3000 cell simulations but not for the 24,000 cell simulations. Interestingly, behavior of the network is not sensitive to violations of this assumption (Fig. 3).

Once a wave has been initiated, it can start new waves of activity in other regions of the network through long-distance connections. The rate at which new waves are generated depends on the current number of waves, w_i, which determines the number of active neurons, αw_i. These active neurons have $\alpha w_i k\rho$ long-distance connections on average. The probability that synapses at the end of these connections start a wave at a postsynaptic neuron is $p_1p_2e_i/N$, where e_i is the number of excitable cells (see below). The approximate symmetry in the connectivity of the ring (because ρ is assumed to be much less than 1) means that a new wave will propagate in two directions as two separate wave fronts. This is reflected in the formula for the new wave rate by multiplying by a factor of two. This approximation is valid, provided that the network is far from being saturated with activity (i.e., when the network size N is much larger than the number of active and refractory neurons) and the resulting wave fronts develop into full waves with refractory wakes, an assumption that is true as long as the waves emerge in a region of nonrefractory cells. The number of excitable cells, e_i, is the total number of neurons minus the number that are active or refractory:

$$e_i = N - \alpha w_i - \alpha \sum_{i=1}^{R} w_{i-i}.$$

The last term in this equation for e_i accounts for the recent history of activity, by summing that past activity up to the refractory time. This sum gives the total number of refractory neurons at time i. Initially, we will further simplify this equation by assuming that the number of refractory cells is simply proportional to the number of active waves: $e_i = N - \alpha w_i(1 + R)$. This approximation is also valid only when the network activity is far from saturation. According to this model, the number of new waves born at time step i is approximated by $n_i = (2\alpha w_i k\rho)(p_1p_2e_i/N) + S_i$. This function, a quadratic function of w_i, is plotted in the top panels of Figure 4 (dashed lines) for three different values of ρ, the proportion of long-distance connections.

The average number of wave collisions per time step depends on how many waves are present in the network. The more waves in the network, the more likely collisions will occur. The expected number of dying waves in a time step can be approximated by the time it takes the currently active waves, evenly distributed around the ring, to collide. We estimate the death rate to be $d_i = 2\alpha w_i/e_i$. In this equation, the term 2α reflects the fact that two wave fronts propagate through an excitable region toward each other at a rate of 2α neurons per time step; the term w_i reflects the fact that evenly distributed waves grow, on average, closer as their number grows; and the term e_i reflects the fact that the average distance between two waves is proportional to the number of remaining excitable cells. As for e_i, the approximation in d_i is most valid when the network activity is far from saturation. The death rate d_i is plotted (solid lines) in the top panels in Figure 4. Its value increases without bound as the number of active and refractory neurons approaches N, when the denominator approaches zero (at the point where the network reaches saturation). The net growth in the number of waves at time i is $n_i - d_i$, and thus the wave birth–death process can be written as a one-dimensional map, $w_{i+1} = f(w_i) = w_i + n_i - d_i$, in which we have defined the function $f(w_i)$ for notational convenience. This one-dimensional map is only valid under the assumption that the number of refractory cells is directly proportional to the current number of active wave (see above) (Table 1).

Activity in the network reaches an equilibrium state when new waves are generated at the same rate that they annihilate each other, i.e., when there is a steady state number of waves w^* that solves the equation $f(w^*) = w^*$. A stable equilibrium corresponds to the slope of the function $f(w_i)$ at the equilibrium between 1 and −1; otherwise, it is unstable and the new wave rate is faster than the dying wave rate. The strength of attraction of this equilibrium

affects the spread of the distribution in the number of neurons firing at any given time in a stochastic network.

The equilibrium level of activity and its stability depend on the parameters in the new wave rate n_i and dying wave rate d_i. As we vary parameters such as the proportion of long-distance connections (ρ), we can investigate how changes in the equilibrium cause the network to switch from normal to seizing to bursting. In the bottom panels in Figure 4, we plot the number of waves on the next time step w_{i+1} versus the number of waves on this time step w_i (solid line) as well as the line of identity ($y = x$; dotted line). In these plots, equilibrium points $f(w^*)$ are indicated by intersections of the solid and dotted lines. Stability of equilibrium points is given by the slope of $f(w^*)$. At low long-distance connectivity ($\rho = 0.001$), both n_i and d_i are small, resulting in a weakly attracting equilibrium (with a slope just less than one). As indicated by the fact that $w_{i+1} \approx w_i$, waves are rarely born or die, implying that the network is dominated by the low rate of spontaneous wave generation. As more long-distance connections are introduced ($\rho = 0.01$), the rate of emergence of new waves increases. This trend increases the number of waves that we expect to see at the equilibrium and also makes the equilibrium more strongly attracting (the slope at the equilibrium point is near zero). As even more long-distance connections are introduced ($\rho = 0.05$), the slope of f at the equilibrium point is less than -1, implying that the equilibrium is unstable. [This is known as a "flip bifurcation," or sometimes as a "pitchfork bifurcation" for maps (Baker and Gollub, 1996).] At this point in the full network model, new waves are generated rapidly, giving rise to a burst (i.e., a large, synchronous increase in the amount of activity). The burst (when $w_i > 6$) would lead to a system that is dominated by wave death on subsequent time steps. Then, almost the entire network will become refractory, implying that the system will be quiescent until enough cells have returned to the excitable state and the network can burst again. This detail of bursting behavior is not captured by our reduced model, which was derived under the assumption that the number of active and refractory cells at any given time is small compared with the network size N. Instead, as ρ is increased above a critical point at ~0.05, the reduced system continues to oscillate between increasingly higher and lower states (around the unstable equilibrium) until the state fluctuates chaotically with a very large amplitude. This describes a well-understood "period-doubling route to chaos" for discrete-time maps such as that described by f (which resembles the classic "logistic" map) (Baker and Gollub, 1996). The amplitudes are large enough that the activity of a full network model would reach saturation at this point and therefore enter our "bursting" regimen. Because the large-amplitude chaotic behavior is reached for ρ values very close to that which first caused the equilibrium to become unstable, the onset of instability is a reasonable indicator for the onset of bursting in the full network model. Results from this reduced model and those from simulations are compared in Figure 5 (discussed below).

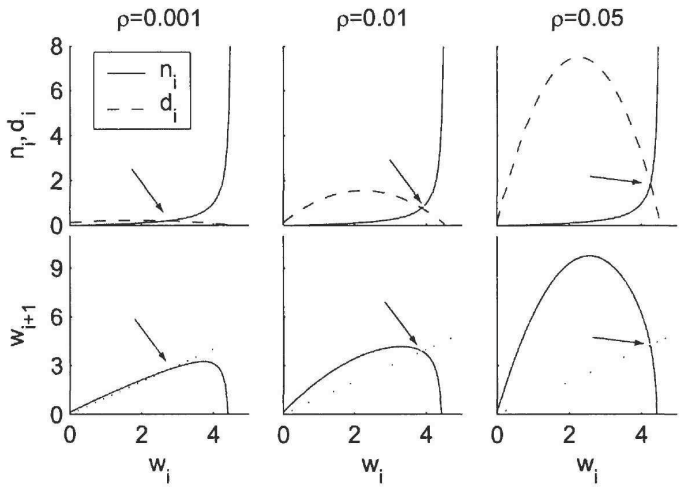

Figure 4. The birth–death process (1-dimensional map) model of wave generation and annihilation. The top panels show how many new waves are generated (n_i; dashed lines) and annihilated (d_i; solid lines) per time step as functions of the number of currently active waves, with $k = 90$. The y-intercept of the dashed lines indicates the spontaneous background rate of wave generation. An equilibrium point exists where the new wave rate is equal to the dying wave rate (indicated by the arrows). The bottom panels map the number of waves on one time step to the average number expected on the next time step (solid lines). Equilibria occur when the number of waves on the next time step is equal to that on the current time step [i.e., at the intersection of the solid line of $f(w_i)$ and the dotted line of identity (also indicated by arrows)]. For $\rho = 0.0001$, the equilibrium point at $w_i \approx 1.82$ is only weakly attracting (the slope of the solid line is approximately +1), and the number of waves changes only slightly at each time step. For $\rho = 0.01$, the system has a strongly attracting equilibrium (where the slope of the solid line is approximately zero), corresponding to ongoing seizures characterized by an average of 3.87 existing simultaneous waves. For $\rho = 0.05$, the equilibrium is unstable, and the dynamics has entered a chaotic regimen. The onset of chaos indicates that the entire network will repeatedly fire brief synchronous bursts.

For both CA1 and CA3 network simulations, the transition from normal activity to seizures corresponds to an increase in the percentage of active cells and the onset of a sustained oscillation in the population activity. Because analysis of the one-dimensional map does not provide us with an explicit condition for this transition, we used the full refractory dynamics in the definition of e_i, making the map $(1 + R)$-dimensional, where R is the length of the refractory period. In a similar way to the one-dimensional map, the $(1 + R)$-dimensional map can be analyzed to predict qualitative changes in the dynamics. For few long-distance connections, both maps exhibit the same equilibria and stability properties. As more long-distance connections are added, the $(1 + R)$-dimensional map exhibits oscillations not present in the one-dimensional map, after a "Hopf bifurcation for maps" occurs as ρ is increased (Agarwal et al., 2000). These small-amplitude oscillations resemble those in the full network simulations during seizures (data not shown) and also have a period approximately equal to the refractory time of the neurons. The transition to oscillation occurs at a value of ρ that can be computed analytically and compared with results from computational simulations (see below). Numerical implementations of the two maps both transition to bursting for similar values of model parameters. However, the $(1 + R)$-dimensional map does not provide an explicit analytic condition for the burst onset. This is because the transition occurs in the full map when the oscillations grow so large that the activity saturates. The saturation of

Table 1. Principal definitions, symbols, and default parameter values used in equations

Symbol	Identification	Definition/values used
N	Number of neurons in network	3000 (24,000 in some network simulations)
k	Number of synapses per neuron	30 (for CA1), 90 (for CA3)
s	Spontaneous firing rate of a single neuron per time step of size τ_d	$0.0315 \times \tau_d$
τ_R	Absolute refractory time of neuron	28 msec (IF), 36 msec (Poiss, HH)
τ_d	Synaptic time delay	2.8 msec (IF), 3.7 msec (Poiss), 1–5 msec (HH)
ρ	Proportion of long-distance connections generated by breaking a synapse and rewiring it to a randomly chosen postsynaptic cell	Varied from 1.0×10^{-5} to 0.4
p_1	Synaptic strength (i.e., probability that postsynaptic neuron will fire given that a particular presynaptic neuron fired)	0.025
p_2	Probability that two postsynaptic neurons fire given the presynaptic neuron fired (dependent on k and p_1)	$p_2 = 1 - (1 - p_1)^k - kp_1(1 - p_1)^{k-1}$
α	Approximate number of neurons in wave front	$k/2 - 1$
R	Number of time steps that a neuron remains refractory	$R = \tau_R/\tau_d \approx 10$
w_i	Number of waves present in network at time i	$w_{i+1} = f(w_i)$
e_i	Number of excitable neurons in the network at time i	$e_i = N - \alpha w_i - \alpha \sum_{t=1}^{R} w_{i-t}$ or $e_i = N - \alpha w_i(1 + R)$ (for one-dimensional map)
n_i	Number of new waves generated at time i resulting from long-distance connections	$n_i = (2\alpha w_i k\rho)(p_1 p_2 e_i/N) + S_i$
d_i	Number of waves that die in time step i resulting from wave collision	$d_i = 2\alpha w_i/e_i$
S_i	Spontaneous wave generation resulting from spontaneous cellular activity	$S_i = sep_2$
w^*	Number of waves in network where new wave rate and dying wave rate are equal (equilibrium point)	$f(w^*) = w^*$
$f(w_i)$	Function describing number of waves on next time step given number of waves on time step i	$f(w_i) = w_i + n_i - d_i$

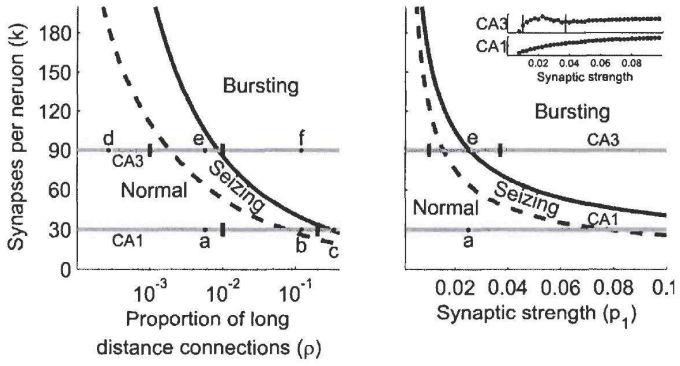

Figure 5. Change in network behavior as a function of number of synaptic connections per neuron and proportion of long-distance connections using the reduced model (for network size of 3000 neurons). The left panel shows curves delineating the normal, seizing, and bursting regimens as the number of synapses per neuron, and the proportion of long-distance connections are changed. The solid black curve is calculated from analysis of the one-dimensional map and the dotted black curve from the $(1 + R)$-dimensional map. Tick marks indicate the boundaries of normal, seizing, and bursting behavior in network simulations from Figure 3. Horizontal lines indicate specific parameter choices for the CA3 and the CA1 models. Points labeled *a–f* correspond to the conditions simulated in Figure 3*a–f*. These plots imply that the CA3 network will transition from normal to bursting at a much smaller proportion of long-distance connections or smaller synaptic strength than the CA1. The right panel illustrates the boundaries between the behavioral regimens as the number of synapses per neuron and the synaptic strength are varied (with the proportion of long-distance connections fixed at $\rho = 0.01$). The curves were calculated in a similar way to that in the left panel. The tick mark in the line for the CA3 indicates the boundary between bursting and seizing observed in the integrate-and-fire model, where the population firing rate as a function of synaptic strength are plotted in the inset. The results of the simulations correlate well with the analyses of the reduced map models. No clear transition from seizing to bursting was seen in the full CA1 model, as predicted by the one-dimensional map model.

activity breaks the assumption of the derivation of the map and is not a precisely definable transition. Thus, it cannot be captured by an analytical expression involving a local change in stability. In contrast, the one-dimensional map represents an "averaged" view of the full dynamics (through its simplified treatment of the refractory wake), for which transition to bursting occurs while the low-activity assumption still holds.

Figure 5*a* shows the boundaries of the different behavior regimens predicted by both of the analytical models as the number of synapses per neuron (k) and proportion of long-distance connections (ρ) is varied. The seizing-bursting border (solid black lines) was calculated from the simplified one-dimensional map. The normal-seizing border (dotted black lines) was derived from the $(1 + R)$-dimensional map. The two horizontal gray lines in each panel correspond to the CA1 and CA3 models from Figure 3. *a–f* in Figure 5*a* correspond to the examples from Figure 3, again as the proportion of long-distance connections ρ is changed over several orders of magnitude. Vertical tick marks in Figure 5*a* correspond to the borders between the normal, bursting, and seizing regimens for the simulated CA1 and CA3 models from Figure 3. Predicted transitions from simplified maps occur near the transition points observed in simulations for a wide range of parameter values.

In the brain and in slice models, epilepsy is probably not caused by an increase in long-distance connections but rather a change in the synaptic strength resulting from drugs or changes in the ionic concentrations of the fluid bathing the slice. Using our reduced map models, we can explore the effects of changing the synaptic efficacy p_1 (Fig. 5*b*), which we define as the probability that a single postsynaptic input gives rise to a postsynaptic spike on the next time step. We look for the regimen transitions as p_1 is varied, keeping ρ at 0.01 (the same value used for panels *a* and *e* in Fig. 3). The transitions predicted by the models are plotted in Figure 5*b*. The total network activity measured from the network simulations is plotted in the insets and shows a drop in activity coinciding with the burst transition for CA3 as predicted (indicated by the line in the inset and the dash in the full panel). The CA1 network did not transition to bursts and had a smooth transition to seizures with an onset that is harder to define but approximately coincides with the predicted values. Thus, the reduced model predicts

that as synaptic strengths are enhanced, CA3 is more likely to transition to bursting, but CA1 is more likely to transition to a seizing regimen, agreeing with experimental results.

Discussion

Here, we have introduced a simple small-world network representation of excitatory neurons in the hippocampal slice. The network was implemented using three different neuron models: noisy and leaky integrate-and-fire, stochastic Hodgkin–Huxley, and a Poisson spike-train model. We used these models to explain why seizures may not be hypersynchronous, but bursts are. In these simulations, seizure activity in the CA1-like networks is not fully synchronous, allowing the activity to be sustained. The same model supports that bursts in CA3 are caused by synchronous rapid recruitment of neuronal activity. Simulation results were independent of particular cellular models used, indicating that the proportion of long-distance connections is more important than the details of individual neurons in determining the epileptiform properties of the network. We derived a reduced mathematical model of the average activity in the network as a birth–death process (map) in discrete time. This model avoids a purely mean-field approximation (which would ignore the small-world properties of the network) and instead retains parameters directly related to the physiology and the connectivity of the network. The one-dimensional map predicted the transition from seizing to bursting found in the network simulations as the number of synapses per neuron, proportion of long-distance connections, and synaptic strength were varied. These transitions were described as a loss of stability of an equilibrium in the map. A more detailed description of the refractory dynamics gave rise to a higher-dimensional map. This map could be analyzed to predict the transition from normal activity to seizing. These reduced models highlight the roles of physical parameters that could underlie the different epileptiform behaviors observed in CA1 versus CA3.

Relation to previous modeling studies

A number of recent modeling studies have examined problems similar to those studied here. For example, Tsodyks et al. (2000) studied coherent activity in randomly connected networks with depressing synapses. They observed coherent activity, somewhat similar to the bursting seen here. In their work and in related work (Tabak et al., 2000; Wiedemann and Luthi, 2003), networks of neurons with depressing synapses initiate bursts from excitatory neurons that had not fired for some time and thus gave rise to large postsynaptic effects. Synaptic depression shut down bursts in these studies. In contrast to these models, our model has explicit small-world connectivity that plays an important role in the behavior of the network. We focused on how changes in the number of long-distance connections, synaptic strength, and overall connectivity led to dramatic changes in network activity.

Nishikawa et al. (2003) studied synchronization in small-world networks that ranged from our Watts–Strogatz style to networks in which a few hyperconnected "hub" neurons served to reduced the mean path length. They found that hubbed networks were less likely to synchronize than Watts–Strogatz networks, although the hubbed networks have smaller mean path lengths. Superficially, this result seems to contrast with our result that the greatest synchronization was seen with small path lengths. But this apparent discrepancy is an artifact of the way the networks were constructed in these two studies. Our results are compatible with the general argument of Nishikawa and colleagues, in that network synchronization decreases with increasing heterogeneity in the number of connections per neuron. Our bursting networks with large ρ have both small mean path and low heterogeneity, because in a randomly connected network, each cell receives approximately the same number of connections. Our seizing networks with small ρ are more heterogeneous and thus are expected to be less synchronized.

Two additional computational efforts have shown that small-world networks similar to ours can synchronize. Networks of oscillatory elements synchronize when the network contains enough long-distance connections of sufficient synaptic strength (Hong et al., 2002). Roxin and colleagues (2004) have showed that adding long-distance connections makes small-world networks of integrate-and-fire neurons transition from sustained activity to synchronous bursts of finite duration. Oscillation of population activity has been studied by Curtu and Ermentrout (2001) and Wilson and Cowan (1973) using differential equations similar in form to our discrete-time maps. Our work utilizes these types of models to study epilepsy. First, we relate our models to epilepsy in a specific brain region (hippocampus) and attempt to explain why regions CA1 and CA3 exhibit different epileptiform behaviors in slice models. Second, we show that the relationship between the number of long-distance connections and seizing or bursting is remarkably independent of the neuronal model used. Third, our derivation of the reduced map models retains important physiological parameters of which the effect on epileptiform behavior can be studied directly.

Relation to experimental results

This model helps to explain how a stable network may become unstable and prone to epileptiform behaviors. Many drugs and disturbances to the cell equilibria can cause this. For example, 4-AP induces epileptiform behaviors in slice models by blocking voltage-gated K^+ channels and thus indirectly enhancing EPSP amplitudes (Chesnut and Swann, 1988). It is shown in Figure 5 that enhancing synaptic strength can transition a stable network into bursting or seizing. Epilepsy can also be induced following cell death. Although decreasing the number of cells alone cannot induce epilepsy in our networks, a concomitant increase in synaptic strength to compensate for the reduced synaptic activity might. Although our simulations only included excitatory cells, normal network activity depends on a balance of excitation and inhibition for stability. The parameter p_1 could be interpreted as representing the ratio of excitation to inhibition. In hippocampal slices, epileptiform activity can be induced by pharmacologically blocking inhibitory synaptic activity (Amitai et al., 1993). These disinhibited slice models of epilepsy show three stages during the ictal event (Borck and Jefferys, 1999). After the first stage of depolarization, the second consists of high-frequency oscillations similar to our seizures. The third stage consists of postictal bursts that are similar to our bursts. Our model suggests that the seizing–bursting transition in disinhibited slices may correspond to increasing synaptic strength, connectivity, or cellular excitability during the ictal event.

We predict from our model that networks with fewer recurrent connections are more likely to seize than networks with more recurrent connections. Our model is consistent with the theory that epileptiform behaviors are generated by positive feedback in excitatory network activity (Schwartzkroin, 1994), resulting in runaway excitation. This may help to explain why some regions of the brain produce seizures, whereas others produce epileptiform bursts. The range of synaptic strengths for which the network will produce seizing behavior is smaller for networks with more recurrent excitatory synapses. These networks are more likely to transition from normal directly to bursting without observing seizures. Our model suggests that epileptiform

bursts in CA1 may occur only when it receives strong synchronous synaptic input from the burst-prone CA3 region. If bursting input to a seizure-producing region is stopped, the region may be released to produce its own seizing behavior, as observed experimentally by Barbarosie and Avoli (1997) and Bragdon et al. (1992).

Organotypic cultures of neocortex generate waves of activity that are reminiscent of our normal and bursting activity (Beggs and Plenz, 2003). Normal activity in the organotypic cultures is scale-free, in that the probability distribution of sizes of waves and the distribution of wave lifetimes both obey a power law, whereas picrotoxin-induced bursts were not. Beggs and Plenz (2003) replicated their scale-free behavior in a multilayer, feed-forward model. In our simulations, distributions of activity do not resemble power laws for normal, seizing, or bursting activity. We believe that our simulated activity is not scale-free primarily because waves of activity, once initiated, almost always propagate over long distances and thus have long lives. This behavior stands in contrast to that observed and modeled by Beggs and Plenz (2003), in which the most common events are small in spatial scale and short in duration.

The time scales that we observe for the bursting and seizing do not necessarily correspond to actual time scales observed experimentally *in vitro*. Furthermore, the seizures in the model do not end as seizures do in the *in vitro* models, because the small-world network model and our mathematical description of the model are highly reduced compared with the hippocampal slice. We expect that fuller models, including inhibition and more spatial realism, may address these discrepancies. The purpose of this model is to develop an understanding of how changes in the physiology change the behavior from normal to bursts to seizures. Therefore, we simulated the networks with only excitatory activity and overestimated the number of recurrent excitatory connections in the CA1 and CA3. This model could be expanded to include inhibitory neurons and more realistic connection schemes, such as a two-dimensional lattice of neurons. The purpose of this model was not to calculate the exact transition of the network behavior or to derive physiological values for these transitions but to give an intuitive feel for why these transitions occur. The exact parameter values where the networks transition between behaviors may differ as we change the form and constituents of the network, but we expect that these transitions will remain qualitatively the same. Nevertheless, we feel that our simple network is useful as one approximation to the qualitative properties of collective behavior in the hippocampus.

References

Agarwal R, Grace S, O'Regan D (2000) Oscillation theory for difference and functional differential equations, Sec 9, Chap 1. Dordrecht: Kluwer.

Amitai Y, Friedman A, Connors BW, Gutnick MJ (1993) Regenerative activity in apical dendrites of pyramidal cells in neocortex. Cereb Cortex 3:26–38.

Baker GL, Gollub JP (1996) Chaotic dynamics: an introduction, Chap 4, Ed 2, p 81. New York: Cambridge UP.

Barbarosie M, Avoli M (1997) CA3-driven hippocampal-entorhinal loop controls rather than sustains *in vitro* limbic seizures. J Neurosci 17:9308–9314.

Beggs JM, Plenz D (2003) Neuronal avalanches in neocortical circuits. J Neurosci 23:11167–11177.

Borck C, Jefferys JG (1999) Seizure-like events in disinhibited ventral slices of adult rat hippocampus. J Neurophysiol 82:2130–2142.

Bower JM, Beeman D (1995) The book of GENESIS: exploring realistic neural models with the GEneral NEural SImulation System, Chap 15, Ed 2, p 245. Santa Clara, CA: Telos.

Bragdon AC, Kojima H, Wilson WA (1992) Suppression of interictal bursting in hippocampus unleashes seizures in entorhinal cortex: a proepileptic effect of lowering $[K+]_o$ and raising $[Ca2+]_o$. Brain Res 590:128–135.

Chesnut TJ, Swann JW (1988) Epileptiform activity induced by 4-aminopyridine in immature hippocampus. Epilepsy Res 2:187–195.

Chow CC, White JA (1996) Spontaneous action potentials due to channel fluctuations. Biophys J 71:3013–3021.

Curtu R, Ermentrout G (2001) Oscillations in a refractory neural net. J Math Biol 43:81–100.

Fox JE, Bikson M, Jefferys JGR (2001) Minimum neuronal aggregate necessary for the generation of epileptiform discharges in the hippocampal slice exposed to low calcium ACSF. Soc Neurosci Abstr 27:969.2.

Gonzalez-Burgos G, Barrionuevo G, Lewis D (2000) Horizontal synaptic connections in monkey prefrontal cortex: an *in vitro* electrophysiological study. Cereb Cortex 10:82–92.

Hong H, Choi MY, Kim BJ (2002) Synchronization on small-world networks. Phys Rev E Stat Nonlin Soft Matter Phys 65:026139.

MacVicar BA, Dudek FE (1980) Local synaptic circuits in rat hippocampus: interactions between pyramidal cells. Brain Res 184:220–223.

McCormick DA, Contreras D (2001) On the cellular and network bases of epileptic seizures. Annu Rev Physiol 63:815–846.

Mountcastle VB (1997) The columnar organization of the neocortex. Brain 120:701–722.

Netoff TI, Schiff SJ (2002) Decreased neuronal synchronization during experimental seizures. J Neurosci 22:7297–7307.

Nishikawa T, Motter AE, Lai YC, Hoppensteadt FC (2003) Heterogeneity in oscillator networks: are smaller worlds easier to synchronize? Phys Rev Lett 91:014101.

Penfield W, Jasper HH (1954) Epilepsy and the functional anatomy of the human brain, Ed 1. Boston: Little Brown.

Perreault P, Avoli M (1989) Effects of low concentrations of 4-aminopyridine on CA1 pyramidal cells of the hippocampus. J Neurophysiol 61:953–970.

Roxin A, Riecke H, Solla SA (2004) Self-sustained activity in a small-world network of excitable neurons. Phys Rev Lett 92:198101.

Schwartzkroin PA (1994) Cellular electrophysiology of human epilepsy. Epilepsy Res 17:185–192.

Staley KJ, Longacher M, Bains JS, Yee A (1998) Presynaptic modulation of CA3 network activity. Nat Neurosci 1:201–209.

Steriade M (2003) Neuronal substrates of sleep and epilepsy. New York: Cambridge UP.

Tabak J, Senn W, O'Donovan MJ, Rinzel J (2000) Modeling of spontaneous activity in developing spinal cord using activity-dependent depression in an excitatory network. J Neurosci 20:3041–3056.

Traub RD, Miles R (1991) Neuronal networks of the hippocampus, Chap 3, p 62. New York: Cambridge UP.

Tsodyks M, Uziel A, Markram H (2000) Synchrony generation in recurrent networks with frequency-dependent synapses. J Neurosci 20:RC50.

Van Drongelen W, Koch H, Marcuccilli C, Pena F, Ramirez JM (2003) Synchrony levels during evoked seizure-like bursts in mouse neocortical slices. J Neurophysiol 90:1571–1580.

Watts DJ (1999) Small worlds, Chap 3, p 58. Princeton: Princeton UP.

Watts DJ, Strogatz SH (1998) Collective dynamics of "small-world" networks. Nature 393:440–442.

Wiedemann UA, Luthi A (2003) Timing of network synchronization by refractory mechanisms. J Neurophysiol 90:3902–3911.

Wilson H, Cowan J (1973) A mathematical theory of the functional dynamics of cortical and thalamic nervous tissue. Kybernetik 13:55–80.

Topological Determinants of Epileptogenesis in Large-Scale Structural and Functional Models of the Dentate Gyrus Derived From Experimental Data

Jonas Dyhrfjeld-Johnsen, Vijayalakshmi Santhakumar, Robert J. Morgan, Ramon Huerta, Lev Tsimring and Ivan Soltesz

J Neurophysiol 97:1566-1587, 2007. First published Nov 8, 2006; doi:10.1152/jn.00950.2006

J Neurophysiol 97: 1566–1587, 2007.
First published November 8, 2006; doi:10.1152/jn.00950.2006.

Topological Determinants of Epileptogenesis in Large-Scale Structural and Functional Models of the Dentate Gyrus Derived From Experimental Data

Jonas Dyhrfjeld-Johnsen,[1]* Vijayalakshmi Santhakumar,[1]* Robert J. Morgan,[1] Ramon Huerta,[2] Lev Tsimring,[2] and Ivan Soltesz[1]

[1]*Department of Anatomy and Neurobiology, University of California, Irvine; and* [2]*Institute for Nonlinear Science, University of California, San Diego, California*

Submitted 6 September 2006; accepted in final form 5 November 2006

Dyhrfjeld-Johnsen J, Santhakumar V, Morgan RJ, Huerta R, Tsimring L, Soltesz I. Topological determinants of epileptogenesis in large-scale structural and functional models of the dentate gyrus derived from experimental data. *J Neurophysiol* 97: 1566–1587, 2007. First published November 8, 2006; doi:10.1152/jn.00950.2006. In temporal lobe epilepsy, changes in synaptic and intrinsic properties occur on a background of altered network architecture resulting from cell loss and axonal sprouting. Although modeling studies using idealized networks indicated the general importance of network topology in epilepsy, it is unknown whether structural changes that actually take place during epileptogenesis result in hyperexcitability. To answer this question, we built a 1:1 scale structural model of the rat dentate gyrus from published in vivo and in vitro cell type–specific connectivity data. This virtual dentate gyrus in control condition displayed globally and locally well connected ("small world") architecture. The average number of synapses between any two neurons in this network of over one million cells was less than three, similar to that measured for the orders of magnitude smaller *C. elegans* nervous system. To study how network architecture changes during epileptogenesis, long-distance projecting hilar cells were gradually removed in the structural model, causing massive reductions in the number of total connections. However, as long as even a few hilar cells survived, global connectivity in the network was effectively maintained and, as a result of the spatially restricted sprouting of granule cell axons, local connectivity increased. Simulations of activity in a functional dentate network model, consisting of over 50,000 multicompartmental single-cell models of major glutamatergic and GABAergic cell types, revealed that the survival of even a small fraction of hilar cells was enough to sustain networkwide hyperexcitability. These data indicate new roles for fractionally surviving long-distance projecting hilar cells observed in specimens from epilepsy patients.

INTRODUCTION

The dentate gyrus, containing some of the most vulnerable cells in the entire mammalian brain, offers a unique opportunity to investigate the importance of structural alterations during epileptogenesis. Many hilar cells are lost in both humans and animal models after repeated seizures, ischemia, and head trauma (Buckmaster and Jongen-Relo 1999; Ratzliff et al. 2002; Sutula et al. 2003), accompanied by mossy fiber (granule cell axon) sprouting. In temporal lobe epilepsy, loss of hilar neurons and mossy fiber sprouting are hallmarks of seizure-induced end-folium sclerosis (Margerison and Corsellis 1966; Mathern et al. 1996), indicating the emergence of a fundamentally transformed microcircuit. Because structural alterations in experimental models of epilepsy occur concurrently with multiple modifications of synaptic and intrinsic properties, it is difficult to unambiguously evaluate the functional consequences of purely structural changes using experimental techniques alone.

Computational modeling approaches may help to identify the importance of network architectural alterations. Indeed, prior modeling studies of idealized networks indicated the importance of altered network architecture in epileptogenesis (Buzsáki et al. 2004; Netoff et al. 2004; Percha et al. 2005). However, to test the role of structural changes actually taking place during epileptogenesis, the network models must be strongly data driven, i.e., incorporate key structural and functional properties of the biological network (Ascoli and Atkeson 2005; Bernard et al. 1997; Traub et al. 2005a,b). Such models should also be based on as realistic cell numbers as possible, to minimize uncertainties resulting from the scaling-up of experimentally measured synaptic inputs to compensate for fewer cells in reduced networks.

Within the last decade, large amounts of high-quality experimental data have become available on the connectivity of the rat dentate gyrus both in controls and after seizures. From such data, we assembled a cell type–specific connectivity matrix for the dentate gyrus that, combined with in vivo single cell axonal projection data, allowed us to build a 1:1 scale structural model of the dentate gyrus in the computer. We characterized the architectural properties of this virtual dentate gyrus network using graph theoretical tools, following recent topological studies of biochemical and social networks, the electric grid, the Internet (Albert et al. 1999; Barabási et al. 2000; Eubank et al. 2004; Jeong et al. 2000; Watts and Strogatz 1998), the *Caenorhabditis elegans* nervous system (Watts and Strogatz 1998), and model neuronal circuits (Lin and Chen 2005; Masuda and Aihara 2004; Netoff et al. 2004; Roxin et al. 2004). To test the functional relevance of the alterations observed in our structural model, we enlarged, by two orders of magnitude, a recently published 500-cell network model of the dentate gyrus, incorporating multicompartmental models for granule cells, mossy cells, basket cells, and dendritically projecting interneurons reproducing a variety of experimentally determined electrophysiological cell-specific properties (Santhakumar et al. 2005).

Taken together, the results obtained from these data-driven computational modeling approaches reveal the topological

* These authors contributed equally to this work.

Address for reprint requests and other correspondence: J. Dyhrfjeld-Johnsen, Department of Anatomy and Neurobiology, University of California, Irvine, CA 92697-1280 (E-mail: jdyhrfje@uci.edu).

The costs of publication of this article were defrayed in part by the payment of page charges. The article must therefore be hereby marked "*advertisement*" in accordance with 18 U.S.C. Section 1734 solely to indicate this fact.

characteristics of the control dentate gyrus and demonstrate that hyperexcitability can emerge from purely structural changes in neuronal networks after loss of neurons and sprouting of new connections, in the absence of changes in synaptic or intrinsic cellular properties.

METHODS

A three-step strategy was implemented to investigate the functional role of the structural reorganizations that take place in the rat dentate gyrus during epileptogenesis: *1*) construction of the database; *2*) construction of the structural models (control and diseased versions); and *3*) construction of the functional models (control and diseased versions). These three steps will be described first, followed by details of the implementation and assessment of the structural and functional models. Additional details can be found in appendixes A1–A3.

Construction of the database and the models

CONSTRUCTION OF THE DATABASE. The database for the normal and epileptic biological dentate networks was assembled from published data. This process itself entailed several distinct steps. As an initial step, eight types of dentate cells were identified as anatomically well described: granule cells, mossy cells, basket cells, axo-axonic cells, molecular layer cells with axonal projections to the perforant path (MOPP cells), hilar cells with axonal projections to the perforant path (HIPP cells), hilar cells with axonal projections to the commissural-associational pathway (HICAP cells), and interneuron-specific (IS) cells (Fig. 1*A*). Next, the numbers of cells for each of these eight neuronal types were estimated from the published data (see cell numbers in the *left column* of Table 1, with references). For a full description of how the cell numbers were estimated, see APPENDIX A1. As a third step in assembling the database, the connectivity matrix was filled in (Table 1). This matrix contains estimates of how many postsynaptic cells among each of the eight cell types a single presynaptic neuron of a given type innervates (for example, from the *third row, second column* in Table 1: a single basket cell innervates about 1,250 granule cells; mean and ranges are indicated, with references). For full justification of the estimates in the connectivity matrix, see APPENDIX A2. As a final step, spatial constraints in connectivity were considered. For each cell type, the extent of the axons of single cells along the septotemporal axis of the dentate gyrus was determined from in vivo single-cell fills published in the literature (Fig. 2). For example, in the case of control mossy fibers, the averaged in vivo axonal distribution of 13 granule cells (Buckmaster and Dudek 1999) was fitted with a single Gaussian (Fig. 2). For a full description of the construction of the axonal distributions from the in vivo single-cell filling data and the single or double Gaussian fits, see APPENDIX A3.

CONSTRUCTION OF THE STRUCTURAL MODEL—CONTROL CONDITION. Once the database was assembled, a structural model of the dentate gyrus was created in the computer. This was a so-called graph network, consisting of "nodes" (corresponding to neurons) and "links" (corresponding to synaptic connections). Each node carried the identity and connectivity pattern of a particular cell type (in other words, there were "granule cell nodes" and "mossy cell nodes," etc.). The links were directed (like synapses) but nonweighted (meaning that a link simply represented the existence of a connection from cell A to cell B, irrespective of the number of synapses between cells A and B or the functional strength of that connection; note that the functional model, described later, takes some of these factors into account). The structural model was full scale (1:1, meaning that the number of nodes in the graph equaled the total number of cells in the dentate gyrus) and captured the salient connectivity and axonal distribution of the various cell types. Overall, the resulting structural model of the dentate gyrus was similar to graph representations of other real-world systems (e.g., Watts and Strogatz 1998).

CONSTRUCTION OF THE STRUCTURAL MODEL—PROGRESSIVE SCLEROSIS. In terms of the structural reorganization of the neuronal networks during limbic epileptogenesis, the loss of hilar cells and the sprouting of mossy fibers are two key factors underlying the process of "end-folium" (meaning the dentate gyrus) sclerosis (Margerison and Corsellis 1966; Mathern et al. 1996) (in the rest of the paper, we will use the shorthand "sclerosis" for end-folium sclerosis; note that end-folium sclerosis is distinct from the broader term "hippocampal sclerosis"). Herein, we simulated the structural changes in sclerosis by removing hilar cells (mossy cells, HIPP cells, HICAP cells, and IS cells) and adding mossy fiber contacts. The biological process of sclerosis (original meaning: "hardening of the tissue") encompasses more than the loss of cells and sprouting of axons (importantly, it also entails gliosis). However, from the perspective of neuronal network reorganization in the dentate gyrus, the loss of hilar cells and the sprouting of mossy fibers are clearly the two major factors.

There were three important features that needed to be considered during the implementation of sclerosis in the structural model. First, just as in the biological network, the loss of hilar cells entailed the loss of both the excitatory mossy cells and the inhibitory HIPP, HICAP, and IS interneurons in the hilus (Buckmaster and Jongen-Relo 1999). Second, just as in the biological network, the spatial extent of sprouted mossy fibers from a single granule cell remained restricted to a single hippocampal lamella (about 600 μm) like the control mossy fibers (Buckmaster et al. 2002b). Third, the progression of sclerosis was implemented by considering full (100%) sclerosis the state of maximal hilar cell loss (when all hilar cells are removed) and the addition of a maximal number of previously nonexistent mossy fiber connections to other granule cells [the densest, anatomically quantified sprouting reported in the literature from an experimental epilepsy model was an average of 275 extra mossy fiber contacts per granule cell (Buckmaster et al. 2002b)—we considered this number 100% sprouting]. Therefore intermediate stages in the progression of sclerosis could be distributed between the control (0% sclerosis) and the maximally sclerotic (100% sclerosis) states. For example, at 50% sclerosis, 50% of mossy cells and 50% of hilar interneurons were lost, and 50% of the maximal sprouting of mossy fibers was implemented (Fig. 1B_2). Sclerosis could also be studied in networks containing only the nodes representing the excitatory cells ("isolated excitatory graph") or only the interneurons ("isolated inhibitory graph"). However, mossy fiber sprouting obviously could not be implemented in the isolated inhibitory graph. Similarly, sprouting could be studied without hilar cell loss ("sprouting-only networks"). However, the reverse was not necessarily true because mossy cell loss without mossy fiber sprouting in the isolated excitatory graph caused the graph to become disconnected as sclerosis progressed (because granule cells do not make synapses on each other in the control network). It should also be noted that in the isolated interneuronal graphs, axo-axonic cells were included only as synaptic targets for other interneurons, but not sampled for the L and C calculations, because they exclusively projected to excitatory neurons. In addition, the interneuronal graphs were characterized only $\leq$96.66% sclerosis because 100% sclerosis resulted in a disconnected graph.

CONSTRUCTION OF THE STRUCTURAL MODEL—EQUIVALENT RANDOM GRAPHS. Specific topological measures (the average path length and the clustering coefficient; see following text) were calculated for each structural model representing different stages in the progression of sclerosis, to quantify how network architecture changes during sclerosis. However, because the numbers of nodes and links change during sclerosis, these topological measures are meaningful only if they are contrasted with similar measures taken for equivalent random graphs at each stage of sclerosis. An

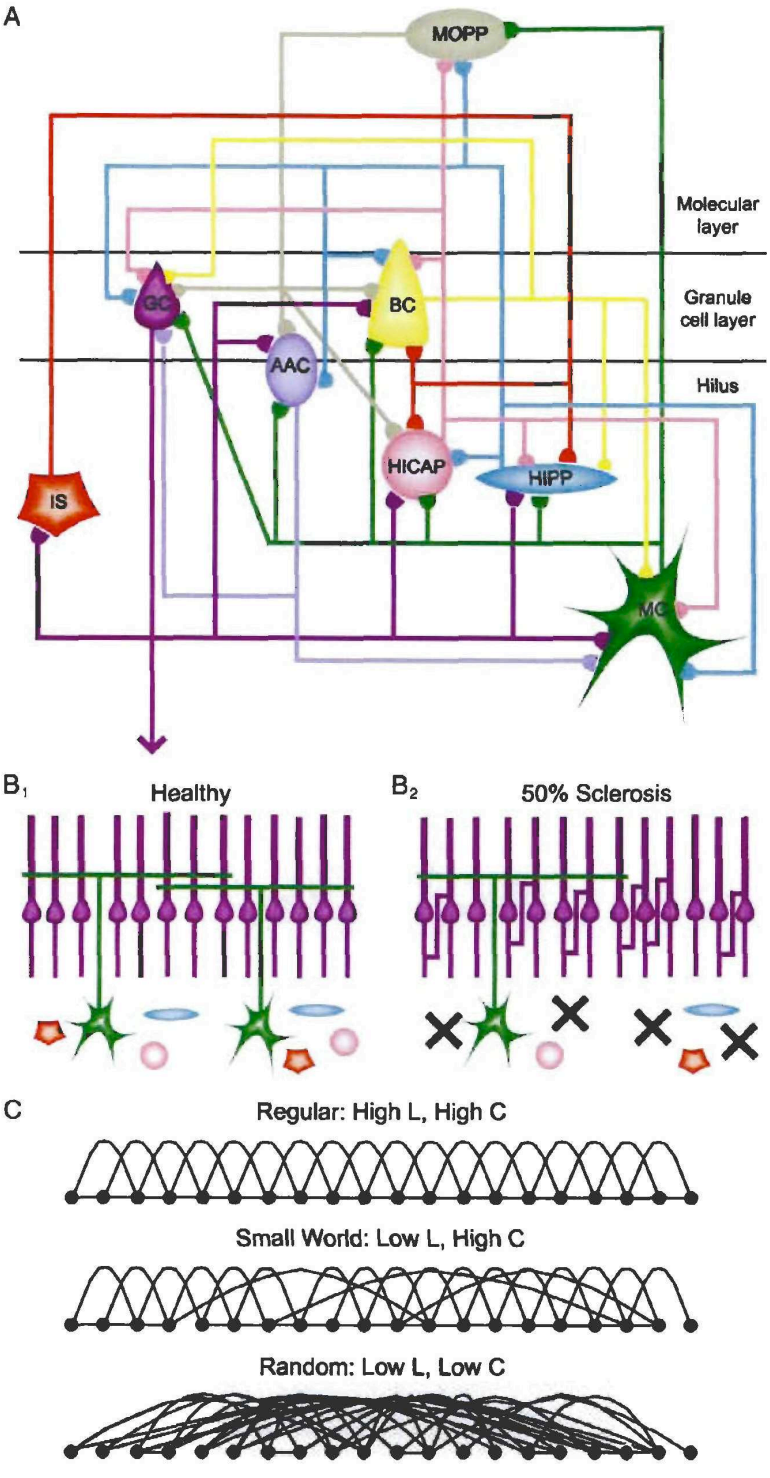

FIG. 1. Schematic of the basic circuitry of the dentate gyrus and the changes to the network during sclerosis. *A*: relational representation of the healthy dentate gyrus illustrating the network connections between the 8 major cell types: GC, granule cell; BC, basket cell; MC, mossy cell; AAC, axo-axonic cells; MOPP, molecular layer interneurons with axons in perforant-path termination zone; HIPP, hilar interneurons with axons in perforant-path termination zone; HICAP, hilar interneurons with axons in the commissural/associational pathway termination zone; and IS, interneuron selective cells. Schematic shows the characteristic location of the various cell types within the 3 layers of the dentate gyrus. Note, however, that this diagram does not indicate the topography of axonal connectivity (present in both the structural and functional dentate models) or the somatodendritic location of the synapses (incorporated in the functional network models). B_1: schematic of the excitatory connectivity of the healthy dentate gyrus is illustrated (only cell types in the hilus and granule cells are shown). Note that the granule cell axons (the mossy fibers) do not contact other granule cells in the healthy network. B_2: schematic of the dentate gyrus at 50% sclerosis shows the loss (indicated by the large × symbols) of half the population of all hilar cell types and the 50% sprouting of mossy fibers that results in abnormal connections between granule cells (note that, unlike in this simplified schematic, all granule cells formed sprouted contacts in the structural and functional models of sclerosis; thus progressive increase in sprouting was implemented by increasing the number of postsynaptic granule cells contacted by single sprouted mossy fibers; see METHODS). *C*: schematics of 3 basic network topologies: regular, small-world, and random. Nodes in a regular network are connected to their nearest neighbors, resulting in a high degree of local interconnectedness (high clustering coefficient C), but also requiring a large number of steps to reach other nodes in the network from a given starting point (high average path length L). Reconnection of even a few of the local connections in a regular network to distal nodes in a random manner results in the emergence of a small-world network, with a conserved high clustering coefficient (C) but a low average path length (L). In a random network, there is no spatial restriction on the connectivity of the individual nodes, resulting in a network with a low average path length L but also a low clustering coefficient C.

TABLE 1. *Connectivity matrix for the neuronal network of the control dentate gyrus*

	Granule Cells	Mossy Cells	Basket Cells	Axo-axonic Cells	MOPP Cells	HIPP Cells	HICAP Cells	IS Cells
Granule cells	**X**	**9.5**	**15**	**3**	**X**	**110**	**40**	**20**
(1,000,000)	X	7–12	10–20	1–5	X	100–120	30–50	10–30
ref. [1–5]	ref. [6]	ref. [7]	ref. [6–9]	ref. [6,7,9]	ref. [6]	ref. [4,10,11]	ref. [4,7,10,11]	ref. [7]
Mossy cells	**32,500**	**350**	**7.5**	**7.5**	**5**	**600**	**200**	**X**
(30,000)	30,000–35,000	200–500	5–10	5–10	5	600	200	X
ref. [11]	ref. [4,11–13]	ref. [12,13]	ref. [13]	ref. [13]	ref. [14]	ref. [12,13]	ref. [12,13]	ref. [15]
Basket cells	**1,250**	**75**	**35**	**X**	**X**	**0.5**	**X**	**X**
(10,000)	1,000–1,500	50–100	20–50	X	X	0–1	X	X
ref. [16,17]	ref. [4,16–19]	ref. [11,16,17,19]	ref. [16,17,20,21]	ref. [18]	ref. [18]	ref. [18]	ref. [18]	ref. [10,20]
Axo-axonic cells	**3,000**	**150**	**X**	**X**	**X**	**X**	**X**	**X**
(2,000)	2,000–4,000	100–200	X	X	X	X	X	X
ref. [4,22]	ref. [4,18,22]	ref. [4,5,11,14,23]	ref. [5,18]	ref. [5,18]	ref. [5,18]	ref. [5,18]	ref. [5,18]	ref. [5,18,19]
MOPP cells	**7,500**	**X**	**40**	**1.5**	**7.5**	**X**	**7.5**	**X**
(4,000)	5,000–10,000	X	30–50	1–2	5–10	X	5–10	X
ref. [11,14]	ref. [14]	ref. [14,24]	ref. [14,25]	ref. [14,26]	ref. [14,25]	ref. [14,20,25]	ref. [14,25]	ref. [14,15]
HIPP cells	**1,550**	**35**	**450**	**30**	**15**	**X**	**15**	**X**
(12,000)	1,500–1,600	20–50	400–500	20–40	10–20	X	10–20	X
ref. [11]	ref. [4,11,20]	ref. [4,11,12,27,28]	ref. [4,11,20]	ref. [20,25]	ref. [25]	ref. [14,20,25]	ref. [25]	ref. [15,20]
HICAP cells	**700**	**35**	**175**	**X**	**15**	**50**	**50**	**X**
(3,000)	700	30–40	150–200	X	10–20	50	50	X
ref. [5,29,30]	ref. [4,11,20]	ref. [20]	ref. [4,11,20]	ref. [20]	ref. [14,20]	ref. [20]	ref. [20]	
IS cells	**X**	**X**	**7.5**	**X**	**X**	**7.5**	**7.5**	**450**
(3,000)	X	X	5–10	X	X	5–10	5–10	100–800
ref. [15,29,30]	ref. [15]	ref. [15]	ref. [15,19]	ref. [15]		ref. [19]	ref. [19]	ref. [15]

Cell numbers and connectivity values were estimated from published data for granule cells, Mossy cells, basket cells, axo-axonic cells, molecular layer interneurons with axons in perforant-path termination zone (MOPP), hilar interneurons with axons in perforant-path termination zone (HIPP), hilar interneurons with axons in the commissural/associational pathway termination zone (HICAP), and interneuron-selective cells (IS). Connectivity is given as the number of connections to a postsynaptic population (*row 1*) from a single presynaptic neuron (*column 1*). The average number of connections used in the graph theoretical calculations is given in bold. Note, however, that the small-world structure was preserved even if only the extreme low or the extreme high estimates were used for the calculation of L and C (for further details, see APPENDIX B1(3). References given correspond to: [1]Gaarskjaer (1978); [2]Boss et al. (1985); [3]West (1990); [4]Patton and McNaughton (1995); [5]Freund and Buzsáki (1996); [6]Buckmaster and Dudek (1999); [7]Acsády et al. (1998); [8]Geiger et al. (1997); [9]Blasco-Ibanez et al. (2000); [10]Gulyás et al. (1992); [11]Buckmaster and Jongen-Relo (1999); [12]Buckmaster et al. (1996); [13]Wenzel et al. (1997); [14]Han et al. (1993); [15]Gulyás et al. (1996); [16]Babb et al. (1988); [17]Woodson et al. (1989); [18]Halasy and Somogyi (1993); [19]Acsády et al. (2000); [20]Sik et al. (1997); [21]Bartos et al. (2001); [22]Li et al. (1992); [23]Ribak et al. (1985); [24]Frotscher et al. (1991); [25]Katona et al. (1999); [26]Soriano et al. (1990); [27]Claiborne et al. (1990); [28]Buckmaster et al. (2002a); [29]Nomura et al. (1997a); [30]Nomura et al. (1997b).

equivalent random graph has the same numbers of nodes and links as the graph (representing a particular degree of sclerosis) to which it is compared, although the nodes have no representation of distinct cell types and possess uniform connection probabilities for all nodes. For example, the equivalent random graph for the control (0% sclerosis) structural model has about a million nodes and the same number of links as in the control structural model, but the nodes are uniform (i.e., there is no "granule cell node," as in the structural model) and the links are randomly and uniformly distributed between the nodes.

CONSTRUCTION OF THE FUNCTIONAL MODEL. The effects of structural changes on network excitability were determined using a realistic functional model of the dentate gyrus (note that "functional" refers to the fact that neurons in this model network can fire spikes, receive synaptic inputs, and the network can exhibit ensemble activities, e.g., traveling waves; in contrast, the structural model has nodes that exhibit no activity). The functional model contained biophysically realistic, multicompartmental single-cell models of excitatory and inhibitory neurons connected by weighted synapses, as published previously (Santhakumar et al. 2005). Unlike the structural model, which contained eight cell types, the functional model had only four cell types, as a result of the insufficient electrophysiological data for simulating the other four cell types. The four cell types that were in the functional model were the two excitatory cells (i.e., the granule cells and the mossy cells) and two types of interneurons (the somatically projecting fast spiking basket cells and the dendritically projecting HIPP cells; note that these represent two major, numerically dominant, and functionally important classes of dentate interneurons, corresponding to parvalbumin- and somatostatin-positive interneurons; as indicated in Table 1, basket cells and HIPP cells together outnumber the other four interneuronal classes by about 2:1). Because the functional model had a smaller proportion of interneurons than the biological dentate gyrus, control simulations (involving the doubling of all inhibitory conductances in the network) were carried out to verify that the observed changes in network excitability during sclerosis did not arise from decreased inhibition in the network, i.e., that the conclusions were robust (see RESULTS and APPENDIX B3).

Although the functional model was large, because of computational limitations, it still contained fewer neurons (a total of about 50,000 multicompartmental model cells) than the biological dentate gyrus (about one million neurons) or the full-scale structural model (about one million nodes). Because of this 1:20 reduction in size, a number of measures had to be taken before examining the role of structural changes on network activity. First, we had to build a structural model of the functional model itself (i.e., a graph with roughly 50,000 nodes) and verify that the characteristic changes in network architecture observed in the full-scale structural model of the dentate gyrus occur in the 1:20 scale structural model (graph) of the functional model as well. Second, certain synaptic connection strengths had to be adjusted from the experimentally observed values (see following text).

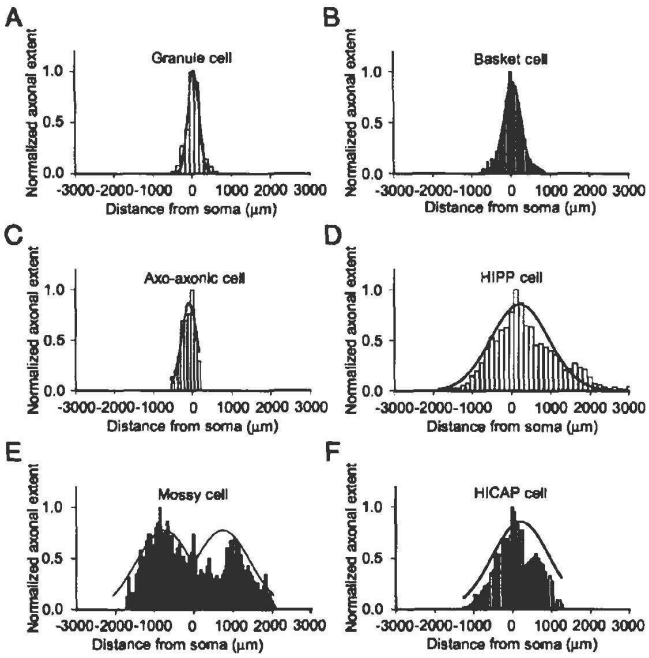

FIG. 2. Gaussian fits to experimentally determined distributions of axonal branch length used in construction of the models of the dentate gyrus. *A*: plot shows the averaged axonal distribution of 13 granule cells (Buckmaster and Dudek 1999) and the corresponding Gaussian fit. *B*: fit to the septotemporal distribution of axonal lengths of a filled and reconstructed basket cell (Sik et al. 1997). *C*: fit to the axonal distribution of a CA1 axo-axonic cell (Li et al. 1992). *D*: Gaussian fit to the averaged axonal distributions of 3 HIPP cells from gerbil (Buckmaster et al. 2002a). *E*: fit to averaged axonal distributions of 3 mossy cells illustrates the characteristic bimodal pattern of distribution (Buckmaster et al. 1996). *F*: histogram of the axonal lengths of a HICAP cell along the long axis of the dentate gyrus (Sik et al. 1997) and the Gaussian fit to the distribution. All distributions were based on axonal reconstruction of cells filled in vivo. In all plots, the septal end of the dentate gyrus is on the *left* (indicated by negative coordinates) and the soma is located at zero.

Implementation and assessment of the models

IMPLEMENTATION OF THE STRUCTURAL MODEL. The dentate gyrus was represented as a 6-mm strip (corresponding to the approximate septotemporal extent of the rat dentate gyrus; West et al. 1978) subdivided into 60-μm bins. Cells of the eight distinct neuronal types were represented in the structural model as individual nodes and distributed evenly among the bins. The nodes were linked according to cell-type–specific connection probabilities derived from the average number of projections from the pre- to the postsynaptic neuronal class in the literature (i.e., according to the connectivity matrix shown in Table 1; appendixes A1 and A2). In general, in addition to the mere existence of connections between two particular cell types (codified in Table 1), the probability of connections from one particular cell A to a given cell B also depends on the extent of the axonal arbor of cell A and the relative distance between cells A and B. Therefore the cell-type–specific connection probability was further modified by a factor obtained by the normalized Gaussian fits to the experimentally determined axonal distributions of the presynaptic cells (APPENDIX A3 and Fig. 2) and the relative positions of the pre- and postsynaptic neurons in the graph. Within these cell-type–specific constraints, connections were made probabilistically on a neuron to neuron (or, more specifically, because we are talking about a graph, a "node to node") basis with a uniform synapse ("outgoing link") density along the axon [in agreement with the in vivo data in Sik et al. (1997)], treating multiple synapses between two cells as a single link and excluding autapses. Note that this implementation of the structural model did not take into account certain potential factors that may distort local connection probabilities (see DISCUSSION). Also note that because the neuronal origin of GABAergic sprouting is unknown (Andre et al. 2001; Esclapez and Houser 1999), only sprouting of mossy fiber connections were included in sclerotic graphs.

ASSESSMENT OF THE STRUCTURAL MODEL: CALCULATION OF GRAPH CHARACTERISTICS. To quantify the topological characteristics of the structural model, the approach of Watts and Strogatz (1998), originally applied to the neuronal network of the worm *C. elegans*, was used. Two measures were used to assess the salient features of the structural models: the average path length L (average number of steps to reach any node in the network) reflecting global connectivity and the average clustering coefficient C (for a given node, the fraction of possible connections between its postsynaptic nodes that actually exist) as a measure of local connectivity. In human societies, for example, C describes the probability that friends of person X also know each other (i.e., it is a measure of local "cliquishness"), whereas L describes what is commonly known as "the six degrees of separation" between any two persons on the planet (i.e., it is a measure of large-distance or "global" connectivity). These two key topological measures for the structural model of the dentate gyrus were calculated using custom C code on a Tyan Thunder 2.0 GHz dual Opteron server (32 GB RAM). Graph calculation times were roughly 50 h per graph.

In general, there are three distinct major network topologies (for reviews, see Buzsáki et al. 2004; Soltesz 2006): *1*) *Regular* (high L, high C); *2*) *Random* (low L, low C); and *3*) *Small world* (low L, high C) (Fig. 1*C*). The graph of a regular (or "ordered" or "lattice-like") network is characterized by a high degree of local interconnectedness (because each node is linked to its nearest neighbors, resulting in a high C), but nodes at the two ends of the graph are separated by a large number of nodes (leading to a high L). In other words, a regular network has an abundance of local connections (thus the comparison to a "lattice" or a fishing net), but has no long-distance connections. Conversely, the graph of a random network is well connected globally (low L), but its local connectivity is low (low C) (this is because random connectivity does not typically form local clusters, but it results in numerous long-distance connections). A small-world structure can be best understood by considering that it can be derived from a regular network by disconnecting and randomly reconnecting a few of its connections (leading to at least a few long-distance connections, which, in turn, results in a low L while retaining the high C of the regular network) (Fig. 1*C*; note that the term "random reconnection" is used here for didactic purposes to describe a commonly used

derivation of a small-world network from a regular network, without implying that long-distance connections in an actual biological small-world network are random). Therefore small-world networks are both locally (high C) and globally (low L) well connected (again, in the language of social networks, humans tend to have a strongly interconnected local cluster of friends, but also at least a few acquaintances with connections far outside of the local circle). The quantitative determination of the small-world topology of a given network is performed by comparison to an equivalent random graph: for a small-world network, $L \approx L_{random}$ and $C \gg C_{random}$.

Given the large size of the graph, L and C were determined from the weighted averages of randomly sampled nodes ("weighted" here refers to the fact that our sampling took into account the ratio of the nodes representing granule cells, mossy cells, and the six interneuronal classes; i.e., the sampling of the nodes in the structural model had to reflect the ratio of the constituent cell types). A minimum of 1/1,000 granule and mossy cells and 1/100 interneurons were sampled and control calculations were performed to verify the accuracy and stability of the sampling method, as described in APPENDIX B1.

IMPLEMENTATION OF THE FUNCTIONAL MODEL. The functional model network was implemented using the NEURON 5.6 simulation environment (Hines and Carnevale 1997). The required simulation times ranged from about 35 to 70 h per model network. The single-cell models were taken from Santhakumar et al. (2005), with morphologies, voltage-gated conductances, and intrinsic properties based on detailed experimental data. Briefly, the single-cell models had nine to 17 compartments including a somatic compartment and two to four dendrites. Minimally, each dendrite was modeled with a proximal, middle, and distal dendritic segment. The models contained nine classes of active conductance mechanisms such as sodium channels, three types of potassium channels (A-type and fast and slow delayed rectifier), three types of calcium channels (L-, N-, and T-type), two types of calcium-dependent potassium channels (SK and BK channels), I_h, and an intracellular calcium clearance process. The intrinsic properties of the cell types were modeled to simulate the passive (membrane potential at rest, input resistance, and membrane time constant) and active (amplitude and threshold of action potential, fast afterhyperpolarization, spike frequency adaptation, and sag ratios) properties observed in experimental data (Lubke et al. 1998; Staley et al. 1992). For granule cells, the somatodendritic distribution of active conductances was adapted from Aradi and Holmes (1999). In all other cell types, the active conductances, with the exception of sodium and fast delayed rectifier potassium channels, were distributed uniformly in all compartments. Sodium and fast delayed rectifier potassium conductances were present only in the soma and proximal dendritic compartments. Additionally, correction for the membrane area contribution of spines was implemented for the granule and mossy cell models. The multicompartmental single-cell models of 50,000 granule, 1,500 mossy, 500 basket, and 600 HIPP cells were evenly distributed in 100 bins along the septotemporal axis.

Connectivity in the functional model network was established using the procedure described for the structural model. All connection probabilities were increased fivefold compared with the structural model, to compensate for the fewer number of cells in the functional model and ensure that no cells in the model networks were disconnected (note that even with this increase in connection probability, each presynaptic cell still made fewer connections in the functional model network than in the full-scale structural model because the postsynaptic cell populations were reduced by a factor of 20; compare Tables 1 and 2). The synaptic conductances between cell types, based on unitary conductances from the literature, were taken from Santhakumar et al. (2005). Excitatory synaptic conductances were adjusted to avoid depolarization block in postsynaptic cells arising from the higher value of the clustering coefficient C in the functional model network (see Fig. 3*B*). Except when specifically stated (see APPENDIX B3), distance-dependent axonal conduction delays were not included. Perforant path stimulation was simulated as in Santhakumar et al. (2005), by a single synaptic input to 5,000 granule cells, 10 mossy cells (note that only a fraction of all mossy cells receive direct perforant path input; Buckmaster et al. 1992; Scharfman 1991), and 50 basket cells (situated in the middle lamella of the model network) at t = 5 ms after the start of the simulation. Additional details of the functional model network, including the convergence and divergence of the connections and the synaptic weights, are listed in Table 2. Note that the current functional model has three primary differences from the network model of Santhakumar et al. (2005). First, we have enlarged the network by two orders of magnitude, making it possible to study the small-world network characteristics of the dentate gyrus.

TABLE 2. *Parameters of functional network model*

		Functional Model Network Parameters			
From	To →	GC	MC	BC	HC
Granule cells*	Convergence	68.03	78.05	370.95	2,266.64
(50,000)	Divergence	68.03	2.34	3.71	27.19
	Synapse weight, nS	1.00	0.20	0.94	0.10
Mossy cells	Convergence	243.62	87.23	5.59	375.53
(1,500)	Divergence	8,120.82	87.23	1.86	150.21
	Synapse weight, nS	0.30	0.50	0.30	0.20
Basket cells	Convergence	3.11	6.31	8.98	n/a
(500)	Divergence	313.22	18.93	8.98	n/a
	Synapse weight, nS	1.60	1.50	7.60	n/a
HIPP cells	Convergence	4.82	3.76	140.13	n/a
(600)	Divergence	401.86	9.39	116.77	n/a
	Synapse weight, nS	0.50	1.00	0.50	n/a
Perforant path†	Synapse weight, nS	20.00	17.50	10.00	n/a

The cell numbers (*column 1*) and synaptic connectivity values and strengths in the functional model network are used for the activity calculations in Fig. 4 (quantified in Fig. 5). Note that this network is smaller (50,000+ cells) than the full-scale dentate gyrus (>1,000,000 cells); thus the connectivity had to be adjusted from what is shown in Table 1. Convergence is given as the number of connections converging onto a single postsynaptic neuron (*row 1*) from a presynaptic neuronal population (*column 1*). For example, 243 mossy cells converge on a single granule cell in this network. Divergence is given as the number of connections diverging to a postsynaptic population (*row 1*) from a single presynaptic neuron (*column 1*). For example, a single mossy cell makes synapses on 8,120 postsynaptic granule cells in this network. The strengths of the connections are given in nanosiemens (nS). For example, the strength of the excitatory synapse formed by a single mossy cell on a single granule cell is 0.3 nS. *Granule cell to granule cell connections represent values at 100% sprouting. †Perforant path input to 5,000 granule cells (two synapses each), 50 basket cells (two synapses each), and 10 mossy cells (one synapse each) in the central 10 bins of the network model.

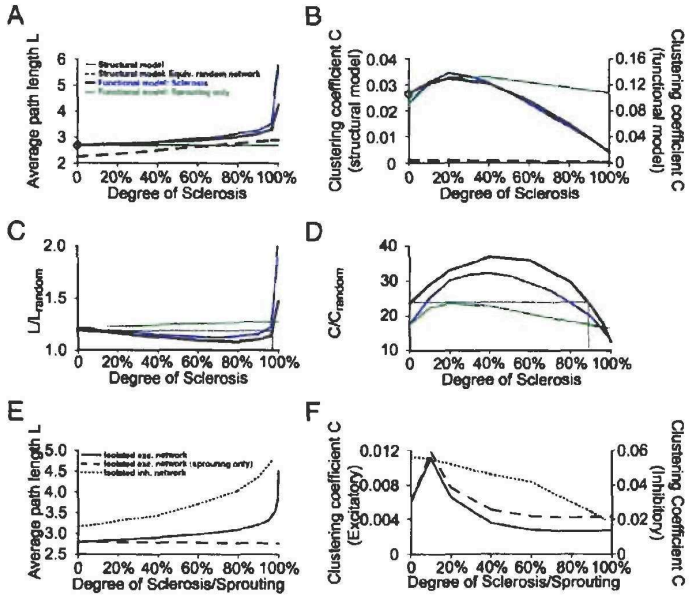

FIG. 3. Alterations in L and C with sclerosis for the various structural models of the dentate gyrus. *A*, *C*, and *E*: changes in average path length L with sclerosis. *B*, *D*, and *F*: changes in clustering coefficient C with sclerosis. Explanation of symbols in *A* also applies to *B–D*. Explanation of symbols in *E* also applies to *F*. Black lines in *A–D*: full-scale structural models. Black lines in *E* and *F*: isolated excitatory/inhibitory graphs. Blue lines: structural model of the functional model with sclerosis. Green lines: structural model of the functional model network with sprouting only. Dashed lines in *A* and *B*: equivalent random graphs of the full-scale structural model. *A* and *B*: plots of the changes in L and C of the various dentate graphs. L and C for the full-scale structural model of the healthy (i.e., at 0% sclerosis) dentate gyrus are marked with "○" on the *y*-axis. *C* and *D*: plots for relative L ($=L/L_{random}$, from *A*) and relative C ($=C/C_{random}$, from *B*). In *C* and *D*, dotted horizontal lines indicate the relative L and C for the full-scale structural model of the healthy dentate graph; vertical dotted lines indicate the degree of sclerosis where the relative L exceeds and the relative C decreases below the values for the control graph. Note the close similarity of the relative L and C changes during sclerosis in the structural model of the functional model network (50,000+ nodes; blue lines) and in the full-scale structural model (>1 million nodes; solid black lines). *E* and *F*: plots of changes in L and C for the isolated excitatory and inhibitory graphs with sclerosis and for the isolated excitatory graphs with sprouting alone (without mossy cell loss), respectively. Changes in L and C for inhibitory interneurons after hilar interneuron loss: dotted lines; for excitatory cell types (granule cells and mossy cells): solid lines; for mossy fiber sprouting in the absence of concurrent mossy cell loss: dashed lines. Note the 2 *y*-axes in *B* and *F*.

Second, in contrast to the Santhakumar et al. (2005) study that focused on moderate (<50%) sclerosis, the current model examines the structural and functional effects of the progression of sclerosis from 0 to 100%. Third, the use of Gaussian fits to constrain axonal distributions instead of an uniform probability adopted in the earlier model considerably increased topological accuracy of this model. Moreover, the current study also tested the effects of hilar interneuronal loss and parallel increases in sprouting and hilar cell loss in contrast to the independent examination of sprouting and mossy cell loss performed in Santhakumar et al. (2005).

ASSESSMENT OF THE FUNCTIONAL MODEL: MEASURES OF HYPEREXCITABILITY. Excitability of the functional model was assessed by a number of measures, including: *1*) total duration of the granule cell discharges in the network (defined as the time from the first spike fired by a granule cell in the network to the last spike fired by a granule cell in the network; note that the first and the last granule cell spikes may originate from different granule cells); *2*) mean number of spikes per granule cell; *3*) latency to spread of activity from the perforant path activation to the firing of the most distant granule cells in the network; and *4*) synchrony of granule cell discharges. Because the latter measure is the most complicated, it will be described below separately.

To assess synchrony, the coherence of granule cell firing between 100 and 200 ms (i.e., sufficiently far in time from the initial stimulus, and during a period where networkwide activity could be observed at most degrees of sclerosis; see Fig. 4) was calculated, using a published coherence measure (Foldy et al. 2004; White et al. 1998). The local coherence was calculated by all-to-all comparison of the activity in granule cells #25000 to #25999. Pairwise comparison of the activity in granule cells #25000 to #25999 and #45000 to #45999 provided the long range coherence. To calculate coherence from the network simulations during the postsimulation analysis, trains of square pulses were generated for each firing cell in a pair with each pulse of unitary height centered on the spike peak and the width equal to 20% of the mean interspike interval of the faster spiking cell in the pair. Subsequently, the shared area of the unit height pulse trains was calculated (equivalent to the zero time lag cross-correlation). Coherence was defined as the sum of their shared areas normalized by the square root of the product of the total areas of the individual trains (Foldy et al. 2004; White et al. 1998).

Data analysis and plotting were done using Matlab 6.5.1 (The MathWorks, Natick MA) and Sigmaplot 8.0 (SPSS, Chicago IL).

Note that the structural and functional model networks are available for download from ModelDB (http://senselab.med.yale.edu/senselab/ModelDB).

RESULTS

Key features of the biological net captured by the structural model

The structural model of the healthy, nonsclerotic dentate gyrus contained over one million (1,064,000) nodes, with the majority (94%) representing granule cells. The million nodes in the control dentate graph were richly linked by over a billion links (1,287,363,500). As in the biological network, there was a large difference in the degree of interconnectedness between nodes representing different cell types. The nodes representing granule cells gave the fewest links (Table 1) and these links were also the most spatially restricted (corresponding to the restricted septotemporal extent of the in vivo filled granule cell axons shown; Figs. 1*B* and 2). In contrast, nodes representing mossy cells formed by far the highest number of links to other nodes (Table 1) and these links spanned almost the entire length of the dentate graph (corresponding to the large extent of single mossy cell axon arbors; Figs. 1*B* and 2).

Globally and locally well connected nature of the control dentate gyrus

We assessed the quantitative topological properties of the control structural model of the dentate gyrus by calculating L and C for the graph at 0% sclerosis and for the equivalent

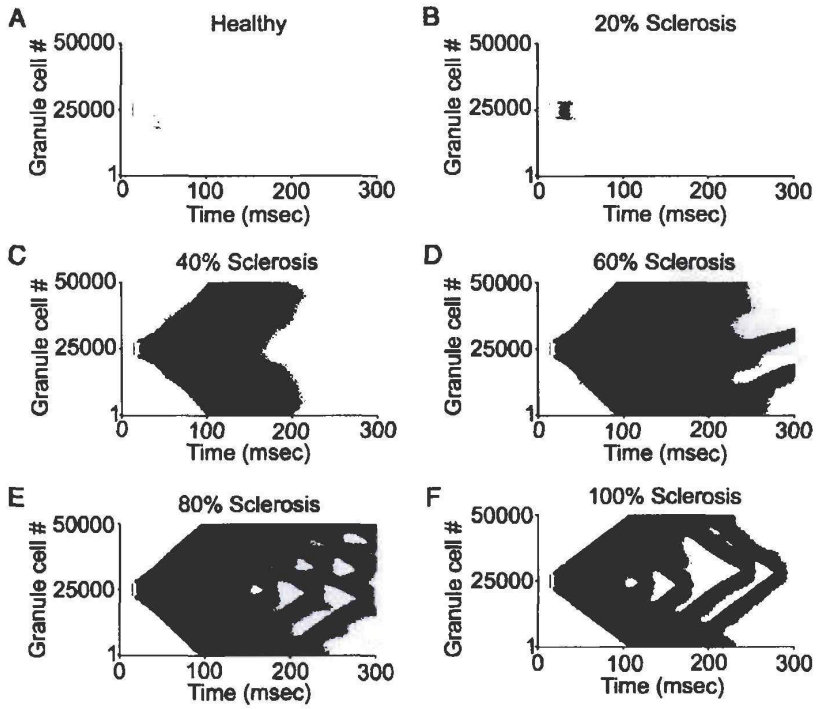

FIG. 4. Effects of the sclerosis-related topological changes on granule cell activity in functional model networks. *A–F*: raster plots of the first 300 ms of action potential discharges of granule cells in the functional model network (Granule cells #1 to #50,000, plotted on the y-axis) at increasing degrees of sclerosis. Network activity was initiated by a single stimulation of the perforant path input to granule cells #22,500 to #27,499 and to 10 mossy cells and 50 basket cells (distributed in the same area as the stimulated granule cells) at t = 5 ms (as in Santhakumar et al. 2005). Perforant path activation led to an initial spike in the directly stimulated granule cells (vertically aligned dots at t = 14 ms), followed by a gap in granule cell activity resulting from inhibition by local, directly stimulated basket cells. Note that the most pronounced hyperactivity was observed at submaximal (80%) sclerosis (for quantification, see Fig. 5, *A–D*).

random graph. The average path length for the control dentate graph was remarkably low (L = 2.68, marked ○ in Fig. 3*A*), considering the presence of over one million nodes in the network. The L = 2.68 value indicated that, on average, fewer than three synapses separated any two neurons in the dentate gyrus. Therefore the low L showed that the graph was well connected globally. To our knowledge, this is the first measurement of L for a mammalian microcircuit, where each neuron is represented by a unique node in the graph. It is interesting to note that the average path length for the control dentate graph was virtually identical to the L = 2.65 reported for the much smaller nervous system of the worm *C. elegans* with a connected graph of only 282 nodes (Watts and Strogatz 1998) (note, however, that the *C. elegans* simulations were done on a nondirected graph, whereas our graphs take into account the directionality of the connections).

The average path length calculated for the equivalent random graph was only slightly lower (L_{random} = 2.25) than the L for the control structural model, resulting in a L/L_{random} ratio close to one (1.19; indicated by the solid black line at 0% sclerosis in Fig. 3*C*). However, the control structural model was much more highly connected locally than the equivalent random graph, as shown by the high value of the relative clustering coefficient (C/C_{random} = 0.026751 / 0.001135 = 24.7, indicated by the solid black line at 0% sclerosis in Fig. 3*D*; note that the control value for C is marked ○ in Fig. 3*B*). The relatively low average path length and high clustering coefficient of the control dentate graph fulfilled the dual requirements of $L \approx L_{random}$ and $C \gg C_{random}$, demonstrating that the normal, healthy biological dentate gyrus is a small-world network (Watts and Strogatz 1998).

Enhanced local and global connectivity with submaximal sclerosis and the transition to a more regular network structure at severe sclerosis

Next, we determined how the graph characteristics of the dentate gyrus change during the progression of sclerosis, characterized by the loss of hilar neurons and mossy fiber sprouting (Longo et al. 2003; Nadler 2003; Ratzliff et al. 2004). The fully sclerotic dentate graph exhibited only a small (4.5%) decrease in the total number of nodes (48,000 nodes representing hilar cells lost out of 1,064,000), but there was a dramatic (74%) reduction in the number of links (953,198,800 links removed out of the total 1,287,363,500), indicating that maximal sprouting did not replace the lost links resulting from the removal of all richly connected hilar cells (Table 1). To determine how small-world topology was affected by the removal of so many links, L and C values were calculated for dentate graphs

constructed at various degrees of sclerosis (solid black lines in Fig. 3, *A* and *B*). Because the average path length and clustering coefficient of the equivalent random graphs also changed with deletion of nodes and addition of links, these were recalculated for each degree of sclerosis (dashed lines in Fig. 3, *A* and *B*).

The results revealed that the progression of sclerosis (increasing loss of the predominantly long distance projecting mossy cells and hilar interneurons, with increasing degrees of spatially restricted mossy fiber sprouting) did not significantly elevate L, until about 90% of the hilar cell nodes were lost (solid black line in Fig. 3*A*). In fact, the relative average path length (L/L_{random}) actually decreased below the control, 0% sclerotic level (illustrated by the horizontal dotted line in Fig. 3*C*). These data indicated that, despite the loss of long-distance projecting hilar cells and the resulting massive decrease in connections, there was a seemingly paradoxical enhancement of long-distance connectivity and conservation of the small-world topology during submaximal (<90%) sclerosis. However, the relative L did not stay below its control value because it showed a sudden increase during the last stages of sclerosis. Therefore the changes in relative L during sclerosis were strongly biphasic (i.e., the initial decrease in L was followed by a sudden increase). Importantly, as illustrated in Fig. 3*C*, it was only at 96.6% sclerosis (vertical dotted line) that the relative average path length (solid black line) started to increase above the control value (horizontal dotted line), indicating that global connectivity was preserved until the final stages of sclerosis.

The high C value (the second characteristic feature of small-world topology) of the control dentate graph was also preserved and actually enhanced during submaximal sclerosis. Although the initial increase in C values was followed by a subsequent decrease at midlevel sclerosis (around 40%) (solid black line in Fig. 3*B*), the relative clustering coefficient (C/C_{random}, solid black line in Fig. 3*D*) increased above the control value (indicated by horizontal dotted line in Fig. 3*D*) up to about 90% sclerosis, showing a sclerosis-related enhancement of local connectivity. Similar to the biphasic changes in relative L, it was only shortly before the onset of full sclerosis that the relative C values decreased below the control level (dotted lines in Fig. 3*D*; note that, even though relative clustering coefficient decreased at 100% sclerosis in Fig. 3*D*, the absolute clustering coefficient in Fig. 3*B* remained more than tenfold higher than C_{random} even at maximal sclerosis).

The decreasing relative average path length (solid black line in Fig. 3*C*) and increasing relative clustering coefficient (solid black line in Fig. 3*D*) during submaximal sclerosis together demonstrated an unexpected enhancement of the features characterizing a small-world topology. However, a transition to a more regular or lattice-like network structure (Watts and Strogatz 1998), characterized by high values of both L and C (i.e., poor global but rich local connectivity), occurred shortly before maximal (100%) sclerosis (note that the fully sclerotic network is not a true lattice structure with only nearest-neighbor connections because, e.g., the axonal arbors of basket cells span roughly 25% of the septotemporal extent of dentate gyrus, providing a large number of midrange connections in the network even at 100% sclerosis).

Analysis of the changing roles of topological factors using isolated excitatory and inhibitory structural models

To determine the mechanisms underlying the transient enhancement of small-world properties during sclerosis, graphs of the excitatory and inhibitory parts of the dentate network were considered separately. First, the isolated excitatory graph was examined. The sclerosis-induced changes in L and C in the isolated excitatory graph (mossy cells and granule cells alone; solid lines in Fig. 3, *E* and *F*) were generally similar to the alterations in the full dentate graph (solid black lines in Fig. 3, *A* and *B*), suggesting that it was the loss of long-range connections (in this case, from mossy cells) and mossy fiber sprouting that played key roles in alterations of graph structure. Sprouting without mossy cell loss did not significantly affect the average path length in the excitatory graph (dashed line in Fig. 3*E*), indicating that the added local connections from sprouted mossy fibers mattered little for L when the long-range connections of the mossy cells were retained. However, sprouting without mossy cell loss in the excitatory graph produced similar changes in the clustering coefficient (dashed line in Fig. 3*F*) as sprouting with mossy cell loss (solid line in Fig. 3*F*). (Note that the essentially unchanged L and the biphasic changes in C observed in the sprouting-only isolated excitatory network will play an important role in determining the role of L and C in network hyperexcitability during sclerosis; see following text.) The decrease in C at higher degrees of sclerosis (which is also observed in the structural model containing both excitatory and inhibitory neurons) was the result of each granule cell primarily contacting other granule cells after mossy fiber sprouting. Because the probability of sprouted connections between any two granule cells is low, the fraction of actually existing connections between pairs of postsynaptic granule cells is also low, resulting in a decreasing C (see METHODS, ASSESSMENT OF THE STRUCTURAL MODEL: CALCULATION OF GRAPH CHARACTERISTICS). In the structural model network containing both excitatory and inhibitory neurons, this dominant influence of granule-to-granule cell connections on the clustering coefficient was more gradual as a result of the larger number of nongranule cell postsynaptic targets of each granule cell.

In contrast to the isolated excitatory graph, the isolated interneuronal graph (i.e., without granule cells and mossy cells) showed a steady increase in average path length and decrease in clustering coefficient with sclerosis (dotted lines in Fig. 3, *E* and *F*) because the progressive loss of hilar interneurons resulted in an increasingly sparse graph (note that there were no granule cells and thus no sprouting of mossy fibers in the isolated interneuronal graph). Interestingly, the control interneuronal graph had an order of magnitude higher clustering coefficient (C = 0.0561) than the control excitatory graph (C = 0.0060), reflecting the significantly more interconnected nature of interneuronal circuits.

These results showed that, during submaximal sclerosis, it was primarily the sprouting of mossy fibers that played a key role in determining topology because the local shortcuts provided by sprouting not only increased C, but also maintained a low L: for granule cells (GC), the loss of mossy cells (MC) removed a number of two-step (GC → MC → GC) and three-step (GC → MC → MC → GC) paths that were partially compensated by the introduction of a large number of new

three-step paths (GC → MC → GC → GC; GC → GC → MC → GC). This mechanism was similar for connections involving other long-range projecting hilar neurons. However, with severe sclerosis, the primary role shifted to the loss of hilar cells because their numbers became too small to maintain the low average path length (even with maximal sprouting). Therefore these calculations, carried out in the isolated excitatory and inhibitory networks, revealed that mossy fiber sprouting was primarily responsible for the transient increase in C at submaximal sclerosis, whereas the dramatic increase in L at maximal sclerosis was mostly explained by the loss of the last distantly projecting hilar neurons. In other words, the key topological determinant switches from sprouting to hilar cell loss during severe sclerosis.

Biphasic alterations in network topology during sclerosis result in biphasic changes in network excitability

Next, the functional consequences of the biphasic alterations in network topology observed in the structural model were explored in our large-scale, topographically, and biophysically realistic functional model of the dentate gyrus (for details on the model, see METHODS). Before the simulations, we first verified that the changes in L and C for the graph of the functional model network with 50,000+ cells were similar to those observed for the graph of the biological network containing 1,000,000+ cells (blue lines in Fig. 3, *A–D*; compare with solid black lines in the same panels).

As with the biological dentate gyrus (Santhakumar et al. 2001), the functional model network of the normal, nonsclerotic dentate gyrus showed only limited firing in response to single simulated perforant path stimulation (Fig. 4*A*). Between 20 and 80% sclerosis (when the features characteristic of small-world topology were found to be enhanced in the structural model), the functional model network showed increasing hyperexcitability (Fig. 4, *B–E*), with activity spreading to the entire network by 40% sclerosis, reminiscent of the epileptiform activity recorded in vitro (Rafiq et al. 1995). However, beyond 80% sclerosis, corresponding to the change from a small-world network to a more regular network in the structural model, the activity in the functional model network decreased (Fig. 4*F*). In other words, changes in network activity during sclerosis, as assessed by a probing stimulus to the perforant path, appeared to be biphasic, similar to the biphasic nature of the topological alterations during sclerosis observed in the structural model. It is interesting to note that the structural changes also affected network dynamics, as indicated by the transition from a spatially relatively uniform pattern (40–60% sclerosis; Fig. 4, *C* and *D*) to a pattern with distinct waves of activity (80–100% sclerosis; Fig. 4, *E* and *F*), that could collide and mutually annihilate (Netoff et al. 2004; Roxin et al. 2004).

Next, we quantified the changes in activity seen in Fig. 4 in the functional model network during sclerosis, using a number of measures of hyperexcitability (see METHODS). Both the maximal duration of granule cell activity and the mean number of spikes fired per granule cell (black lines in Fig. 5, *A* and *B*) increased and peaked at 80% sclerosis, followed by a decrease at 100% sclerosis. For degrees of sclerosis where the activity spread to the entire functional model network (40–100% sclerosis), the latency from perforant path activation to the firing of the most distant granule cells (black line in Fig. 5*C*) was the shortest (i.e., activity spreads the fastest) at 60% sclerosis (89.7 ms), followed by an increase in latency to the maximal value at 100% sclerosis (106.2 ms). The topological alterations also affected synchrony of firing in the network. Comparison of local and global synchrony in granule cell firing showed that local and long-range coherences initially were similar at 40 and 60% sclerosis (Fig. 5*D*, dashed black line: local coherence; solid black line: long-range coherence), but the long-range

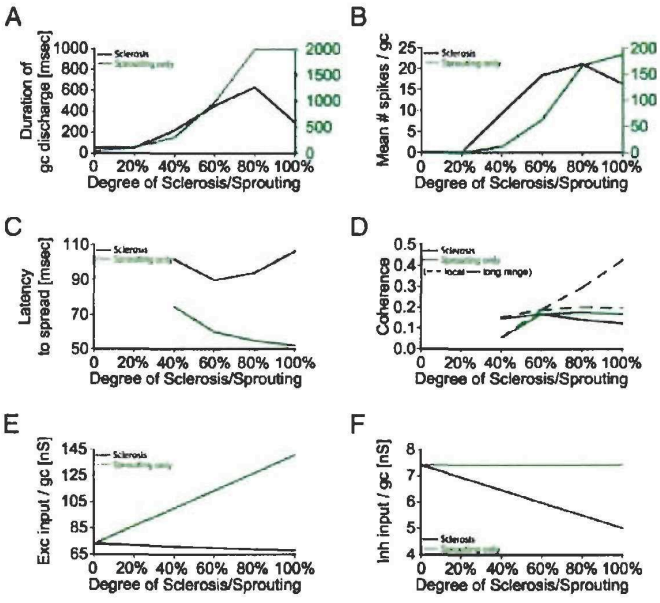

FIG. 5. Biphasic changes in granule cell firing in the functional model of the dentate gyrus during progressive sclerosis and the lack of biphasic changes when sprouting occurs without hilar neuron loss. Black lines: sclerosis; green lines: sprouting alone, without concurrent hilar cell loss. *A*: changes in the maximal duration of perforant path stimulation-evoked granule cell firing (for a description of this measure, see METHODS) as a function of sclerosis or sprouting alone (note that granule cell firing persisted beyond 2,000 ms at 80 and 100% sprouting in the sprouting-only case). *B*: mean number of spikes fired per granule cell with progressive sclerosis or sprouting without cell loss. *C*: latency to firing of granule cells in all 100 bins, in networks with persistent activity in all granule cell bins. *D*: local (dashed line, all-to-all comparison of action potential firing in granule cells #25000 to #25999) and long range (solid line, pairwise comparison of the activity in granule cells #25000 to #25999 to granule cells #45000 to #45999) coherence of granule cell firing in the time interval of 100 to 200 ms for 40–100% sclerosis or sprouting without cell loss. Note that in *C* and *D*, results are shown only for 40–100% sclerosis or sprouting, where activity spread to the entire network and persisted beyond 100 ms. *E* and *F*: changes in average total peak conductance of excitatory (*E*) and inhibitory (*F*) synapses onto the model granule cell during sclerosis or sprouting in the absence of cell loss. Note the lack of biphasic changes in *A–D* when sprouting took place without hilar cell loss.

coherence subsequently decreased with increasing sclerosis, whereas the local coherence dramatically increased. This divergence of local and long-range synchrony with progressive sclerosis reflected the increasing dominance of short-range connections over long-range hilar cell axonal projections. Taken together, these measures all indicated that biphasic changes in the structural model resulted in biphasic alterations in hyperexcitability during sclerosis.

We also tested the potential caveat that changes in the activity of the functional model network simply reflected alterations in net excitatory and inhibitory conductances to granule cells, rather than transitions in network architecture. As shown in Fig. 5, *E* and *F* (black lines), there was a monotonic decrease in both net excitatory and inhibitory peak conductances received by individual granule cells during sclerosis. Clearly, these monotonic changes in synaptic innervation of the granule cells could not be directly responsible for the biphasic changes in network activity.

Network activity parallels changes in sprouting in the absence of cell loss

The described biphasic changes in network hyperexcitability during sclerosis (solid black lines in Fig. 5, *A–D*) occurred in conjunction with biphasic changes in both relative average path length and relative clustering coefficient (solid black and blue lines in Fig. 3, *C* and *D*). Which of these two topological measures primarily determine changes in network hyperexcitability? How do the changes in L and C correspond to cell loss and mossy fiber sprouting? To answer these questions, we took advantage of the fact that (as noted before), in graphs of the isolated excitatory network with sprouting but no cell loss (dashed lines in Fig. 3, *E* and *F*), the average path length did not change significantly, but the clustering coefficient still underwent a biphasic change with increasing degree of sprouting. Therefore we could use sprouting-only networks (showing unchanged L but biphasic changes in C) to test whether biphasic changes in the clustering coefficient alone would conserve the biphasic changes in network hyperexcitability. Accordingly, we constructed functional model networks where mossy fiber sprouting occurred in the absence of hilar neuron loss. Again, before the actual simulations were performed, we first verified that the graphs of these sprouting-only functional model networks indeed showed the expected biphasic changes in absolute and relative clustering coefficient (green lines in Fig. 3, *B* and *D*), without significant changes in absolute and relative average path length (green lines in Fig. 3, *A* and *C*). (Note that these calculations were crucial because the functional model network contained 20 times fewer neurons than the number of nodes in the structural model network. Therefore topological changes taking place in the structural model cannot be automatically assumed to occur in the graph of the functional model.)

In response to perforant path stimulation, the sprouting-only functional model networks showed increasing granule cell activity with progressive sprouting, which spread to the entire model network in a self-sustained manner at 40–100% sprouting (Fig. 6). Detailed analysis of the activity in the sprouting-only networks (green lines in Fig. 5, *A–D*) showed that both the maximal duration of activity and the mean number of spikes fired per granule cell increased monotonically with increasing degree of sprouting and exceeded those in the corresponding sclerotic networks (compare black and green lines in Fig. 5, *A* and *B*; note the difference in scale of the *y*-axes), whereas the latency of the spread of activity to the most distant granule cells steadily decreased (green line in Fig. 5*C*). In contrast to the sclerotic networks (black lines in Fig. 5*D*), the local and long-range coherence of the granule cell firing remained similar to each other for all degrees of sprouting in the sprouting-only networks (green lines in Fig. 5*D*). The monotonic increase in granule cell firing and decrease in latency of activity propagation in the sprouting-only networks reflected the monotonic increase in excitatory drive to granule cells with progressive sprouting (68 nS increase per granule cell at maximal sprouting; green line in Fig. 5*E*), whereas inhibition remained constant (green line in Fig. 5*F*).

These results with the sprouting-only networks demonstrate that biphasic changes in the absolute and relative clustering coefficient alone (i.e., without corresponding alterations in path length) do not result in biphasic changes of network hyperexcitability. Therefore these findings further support the conclusion that, in networks with concurrent sprouting and hilar neuron loss, the biphasic changes in relative average path length and the corresponding transition from a small world to a more regular network structure were primarily responsible for the biphasic change in network hyperexcitability.

Control simulations and tests of robustness

To examine the robustness of our results, we tested the effects of changes in structural and functional parameters on L and C values and on network activity in an extensive series of control simulations. These controls are described in appendixes B2 and B3 and illustrated in Figs. 7–9. The control simulations concerning structural parameters [APPENDIX B2, (1)–(5)] included tests of cell-type–specific changes in neuronal density along the septotemporal axis, inhomogeneity in connectivity along the transverse axis, axonal distributions at the septal and temporal poles of the model dentate gyrus, offset degrees of cell loss and sprouting, and the bilateral dentate gyrus model with both associational and commissural projections. The control simulations concerning functional parameters [APPENDIX B3, (1)–(3)] included increasing (doubling) the strength of inhibitory synaptic connections, inclusion of axonal conduction delays, and simulation of spontaneous instead of stimulation-evoked activity.

All variations in structural parameters in these control calculations yielded L and C values that were similar to the L and C values of the base model used in the rest of the paper. Similarly, the simulations of activity with altered structural and functional parameters all displayed the characteristic decrease in network activity with the transition from 80 to 100% sclerosis, demonstrating the robustness of the major conclusions.

DISCUSSION

The following are major findings of this study. *1*) The control dentate gyrus is a locally and globally well connected small-world network. *2*) Structural alterations during epileptogenesis result in biphasic changes of small-world topology. Initially, and during the majority of the sclerotic process, the

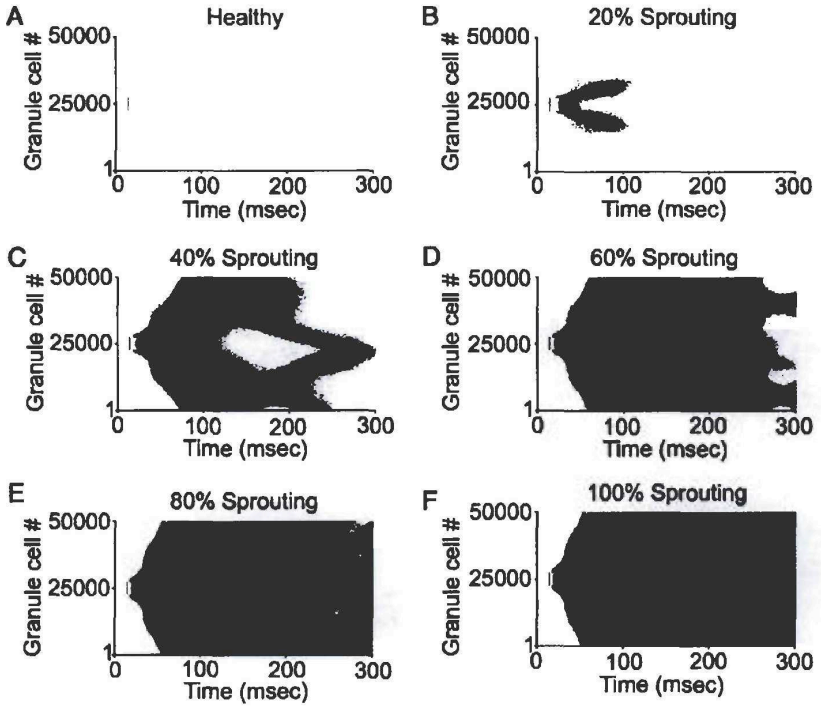

FIG. 6. Functional effects of sprouting without hilar neuron loss in the functional model network. *A–F*: raster plots of action potential discharges of granule cells in the functional model networks at increasing degrees of mossy fiber sprouting. Network activity was initiated as in Fig. 4. Note that maximal hyperactivity occurred at maximal sclerosis (for quantification, see Fig. 5, *A–D*).

features defining the small-world characteristics of the dentate gyrus are enhanced (the dentate gyrus becomes "more small world" than in its control state). This is shown by a decreased relative L and increased relative C, indicating enhanced global and local connectivity. However, just before maximal sclerosis is reached, the relative L sharply increases as a result of the loss of the last long-distance projecting hilar cells, while relative C declines, leading to an overall decrease in the small-world characteristics. *3*) Analyses of isolated excitatory and inhibitory graphs show that biphasic changes in small-world characteristics correspond to changing roles of topological factors: During submaximal sclerosis, the key factor is the predominantly local mossy fiber sprouting, which (as long as at least some long-distance projecting hilar cells survive) compensates for the loss of hilar cells (leading to a decrease in relative L, despite the loss of many long-distance connections). However, during the last stages of sclerosis, the loss of hilar neurons becomes the major topological determinant: as the last long-distance connections are removed, the network evolves into a more regular, lattice-like structure. *4*) Simulations in the functional network show that changes in network topology predict the development of hyperexcitability: during submaximal sclerosis, when small-world characteristics increase, network hyperexcitability increases; however, during the last stages of sclerosis, when small-world characteristics decrease, the network hyperexcitability declines. *5*) Sprouting-only networks, showing insignificant changes in L but biphasic changes in C, exhibited monotonic increases in hyperexcitability. These latter results further underline the importance of network topology by indicating that, in networks with concurrent sprouting and hilar cell loss, the biphasic changes in relative L (and the corresponding transition from a small-world to more regular network topology) are primarily responsible for the biphasic change in network hyperexcitability. Consequently, these results suggest that the survival of even a few hilar cells is critically important in maintaining networkwide hyperexcitability in the epileptic dentate gyrus.

Limitations of the models and robustness of the conclusions

Although our structural model was full scale and incorporated eight neuronal classes with cell-type–specific and topographic connections, the "virtual dentate gyrus" did not replicate the complete connectivity of the biological network. In most cases, specific components were not represented in the structural model because no precise data were available. For example, recent results indicate that local connection probability may be modified by intraclass correlations (Yoshimura and Callaway 2005; Yoshimura et al. 2005) and overrepresentation of small network motifs (Milo et al. 2002; Reigl et al. 2004; Song et al. 2005; Sporns and Kotter 2004). However, there is no evidence for such factors in the dentate gyrus. In the functional model, the neuronal populations were simulated with homogeneous cellular properties and synaptic connectiv-

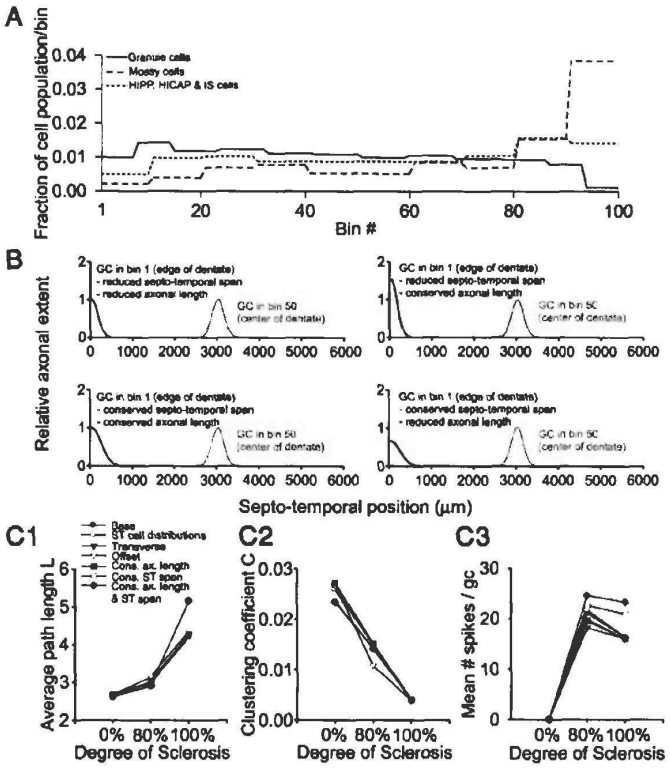

FIG. 7. Control simulations for structural parameters. *A*: cell-type–specific changes in neuronal densities along the septotemporal axis of the dentate gyrus, based on estimates from published data [see APPENDIX B2(1)]. Bin #1 is the septal end. *B*: 4 distinct boundary conditions, implemented to test the effects of skewing axonal distributions toward the septal and temporal poles of the model dentate gyrus [see APPENDIX B2(3)]. *C*: results of the calculations of L (C_1) and C (C_2), and of the simulations of activity (C_3), for the various controls designed to test the effects of changes in structural parameters. Labels in C_1 apply to all panels in *C*: "Base": base model used in the simulations described in RESULTS [corresponding to reduced septotemporal span, reduced total axonal length; see APPENDIX B2(3)]; "ST cell distributions": septotemporal cell distributions [illustrated in *A* and described in APPENDIX B2(1)]; "Transverse": inhomogeneous connectivity perpendicular to the septotemporal axis [APPENDIX B2(2)]; "Offset": offset (i.e., staggered) changes in the degrees of sprouting and hilar cell loss [APPENDIX B2(4)]; "Cons. ax. Length": conserved axonal length, with reduced septotemporal span; "Cons. ST span": conserved septotemporal span, reduced axonal length; "Cons. ax. length and ST span": both axonal length and septotemporal span conserved. Note that for the "offset" simulations, 70% sprouting with 90% hilar cell loss is plotted as 80% sclerosis for simplicity; similarly, 80% sprouting with 100% hilar cell loss is plotted as 100% sclerosis. Note that all 6 controls for structural parameters plotted in *C* yielded similar L and C values as those of the base model, and they all showed the characteristic decrease in activity with the progression of sclerosis from 80 to 100%.

ity strengths. However, a large degree of heterogeneity was still present, stemming from the use of four very different neuronal populations with different synaptic characteristics, variability in the number and distribution of connections, and a random, noisy conductance implemented in the mossy cell models to emulate the experimentally described spontaneous firing. Furthermore, simulations with continuous random synaptic activation of the network (see Fig. 9, *C* and *D*) did not alter the described behavior. The functional model deliberately did not incorporate a number of factors that reportedly change in epilepsy because our goal was to test the functional roles of purely structural changes, while keeping all functional parameters unaltered.

Despite model limitations, the conclusions are remarkably robust. Confidence in the results are strengthened by two factors: *1*) the multicompartmental single-cell models were specifically developed to replicate a large number of electrophysiological properties, including resting membrane potential, input resistance, action potential amplitude, threshold, adaptation, afterhyperpolarization, maximal firing rate, and sag ratio (Santhakumar et al. 2005); and *2*) the functional networks constructed from these model cells simulate biological responses, including action potential firing in only a small fraction of granule cells in response to a single-shock stimulation of perforant path fibers under control conditions (Santhakumar et al. 2005) (Fig. 4*A*), resulting from the low resting membrane potential of granule cells and strong feedforward inhibition from basket cells. Also, hyperexcitability already emerged in the functional model at mild (20–40%) levels of sclerosis, in agreement with experimental observations (Lowenstein et al. 1992; Santhakumar et al. 2001; Toth et al. 1997). In addition, an extensive series of control simulations (appendixes B2 and B3) tested the dependency on structural and functional parameters that may not have been well constrained by experimental data: e.g., the biphasic change in network hyperexcitability was unaltered despite doubling of all inhibitory conductances in the functional model to compensate for the excluded interneuronal subtypes. Remarkably, control simulations with the bilateral model showed that the conclusions persisted even when the network was doubled in size and interconnected with anatomically realistic commissural projections. The robustness of the conclusions was further supported by the strong predictive powers of the different models: e.g., although the structural model was based on nonweighted graphs, consistent functional effects were observed in the functional model with weighted synaptic connections.

Control dentate microcircuit as a small-world network

Our results demonstrated that neurons in the healthy dentate gyrus form a both locally and globally well connected small-world network microcircuit. Interestingly, any two neurons in the healthy dentate gyrus were separated by fewer than three synapses on average, just as in the *C. elegans* neuronal network (Watts and Strogatz 1998), despite the severalfold difference in network size. It is interesting to speculate that perhaps an

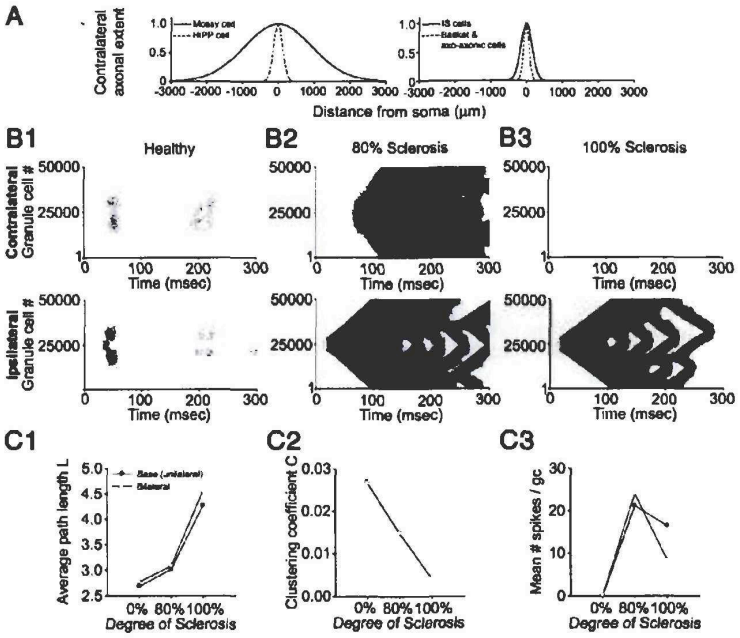

FIG. 8. Control simulations with the bilateral model of the dentate gyrus. *A*: cell-type–specific commissural axonal distributions, based on estimates from data in the published literature [see APPENDIX B2(5)]. *B*: raster plots of granule cell activity as a function of sclerosis in the functional bilateral model. *Top panels*: contralateral side. *Bottom panels*: ipsilateral side. B_1: 0%, B_2: 80%, B_3: 100% sclerosis. Sclerosis was bilateral and perforant path stimulation was applied to the middle lamella in the ipsilateral side only. Note that at 100% sclerosis, the activity did not spread to the contralateral side as a result of the complete loss of mossy cells. *C*: calculations of L (C_1) and C (C_2) show that the L and C for the entire bilateral network were similar to the L and C of the "base" full-scale (ipsilateral) structural model of the dentate gyrus used to obtain the data presented in RESULTS. C_3 shows that the drop in activity (calculated for both sides) with the progression of sclerosis from 80 to 100% was present in the bilateral functional model (and was even more pronounced than in the base model). Note that the symbols in C_1 also apply to C_2 and C_3 (symbols in C_2 overlap).

evolutionary pressure exists to keep L constant as network size increases. However, more networks must be analyzed to test this hypothesis. Currently, the only neuronal networks for which L and C values have been determined, with individual neurons considered as distinct nodes, are the networks of the *C. elegans* (Watts and Strogatz 1998), culture systems (Shefi et al. 2002), and the dentate gyrus (present study). In all other studies where small-world characteristics were determined from anatomical data, the nodes were entire brain areas (Achard et al. 2006; Sporns and Zwi 2004; Stephan et al. 2000), not single cells. Studies describing small-world topology of interarea brain connectivity (Sporns and Zwi 2004; Stephan et al. 2000)

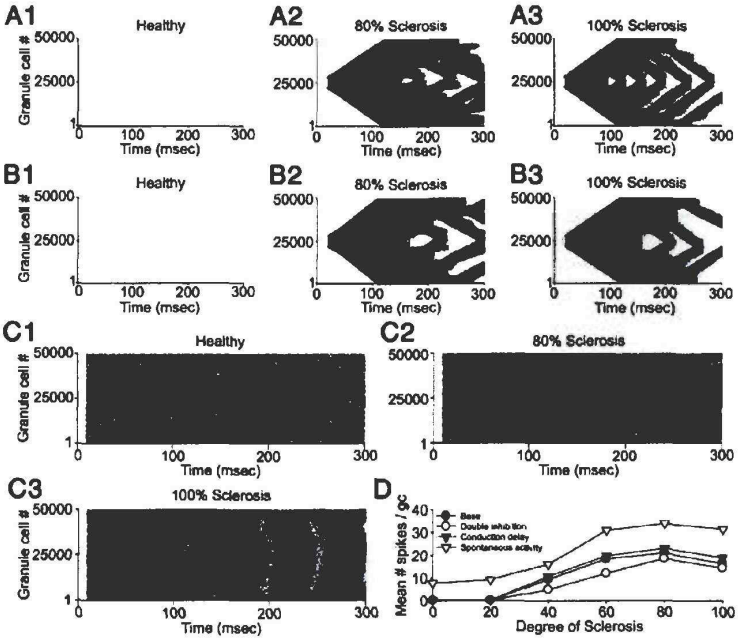

FIG. 9. Control simulations for functional parameters. *A*: granule cell activity in functional model networks with double inhibition [maximal conductance of all inhibitory synapses indicated in Table 2 was doubled compared with the base network used in the rest of the simulations; see APPENDIX B3(1)]. *B*: granule cell activity with axonal conduction delays included in the network [an axonal conduction velocity of 0.25 m/s (Bartos et al. 2002) was implemented in the network; see APPENDIX B3(2)]. *C*: granule cell activity in functional model networks with spontaneous activity [simulated 10-Hz Poisson-distributed perforant path inputs were applied independently to all granule cells, all basket cells and 100 mossy cells, as a function of increasing amount of sclerosis; see APPENDIX B3(3)]. A_1, B_1, C_1: 0% sclerosis; A_2, B_2, C_2: 80% sclerosis; A_3, B_3, C_3: 100% sclerosis. *D*: summary plot of granule cell activity for the base model used in the rest of the paper and for the 3 control simulations depicted in this figure. Note that, in spite of large changes in functional parameters, the characteristic biphasic shape of the changes in activity with sclerosis (the drop in activity with the progression of sclerosis from 80 to 100%) was present in all simulations.

predict that the low L of the dentate gyrus is unlikely to increase considerably when larger parts of the limbic system are considered, in agreement with the presence of long-distance connections between distinct limbic areas (Buzsáki et al. 2004; Ceranik et al. 1997; Sik et al. 1994).

Functional relevance of topological changes during epileptogenesis and correspondence to experimental data

Based on the presence of both local and long-distance connections, it may be predicted that small-world topology should allow both fast local computations and efficient relay of signals to distant parts of the network. Indeed, previous modeling studies demonstrated that small-world networks display fast signal propagation and long-range synchronization (Barahona and Pecora 2002; Lago-Fernandez et al. 2000; Li and Chen 2003; Masuda and Aihara 2004). We found a marked enhancement of small-world characteristics of the submaximally sclerotic dentate that was accompanied by increasing degrees of hyperexcitability, as assessed by a number of different measures. The enhancement of small-world network characteristics during submaximal sclerosis was counterintuitive (it took place despite a massive loss of connections), occurring because mossy fiber sprouting compensated for the loss of long-range hilar neurons, leading to only slight increases in L. However, this compensation was a double-edged sword: because of the highly localized mossy fiber sprouting, submaximal sclerosis increased the clustering coefficient, leading to an overall enhancement of small-world network properties, and thus enhanced network hyperexcitability.

The importance of network topology was perhaps best demonstrated by the surprising decrease of hyperexcitability with maximal sclerosis. This decrease in hyperexcitability took place at the transition from small-world topology to a more regular network structure, resulting from the loss of the last hilar mossy cells that normally project several millimeters in the dentate gyrus, innervating tens of thousands of granule cells. This result not only supported the functional role of network topology, it is also in agreement with experimental observations in both epileptic animals and humans. That is, in experimental studies of animal models of epilepsy where quantitative hilar cell counts have been performed, the hilar cell loss was never 100% (Buckmaster and Dudek 1997; Buckmaster and Jongen-Relo 1999; Cavazos and Sutula 1990; Cavazos et al. 1994; Gorter et al. 2001; Leite et al. 1996; Mathern et al. 1997; van Vliet et al. 2004; Zappone and Sloviter 2004). (Note that our results indicate that even a tiny fraction of mossy cells can maintain low L and a high level of hyperexcitability.) Similarly, in surgically removed specimens from pharmacologically intractable human temporal lobe epilepsy patients (Gabriel et al. 2004), cell counts showed that roughly 20% of the mossy cells survive on average, even in patients with pronounced sclerosis (Blumcke et al. 2000). The survival of 20% of the mossy cells in human specimens from intractable epilepsy patients coincides with the maximal epileptiform activity in our model networks observed at around 80% sclerosis.

APPENDIX A1: ESTIMATION OF CELL NUMBERS

The number of granule cells (GCs) in the dentate gyrus of the rat was estimated to be 1,000,000 (Boss et al. 1985; Freund and Buzsáki 1996; Gaarskjaer 1978; Patton and Mcnaughton 1995; West 1990). Buckmaster and Jongen-Relo (1999) estimated the number of GAD-mRNA negative neurons in the dentate hilus [presumed mossy cells (MCs)] to be 30,000 (see also control calculations in APPENDIX B1). The maximal fraction of GABAergic cells in the granule cell layer of the dentate has been estimated to be 2% (Babb et al. 1988; Woodson et al. 1989), many of which are likely to be basket cells (BCs) (Patton and Mcnaughton 1995). Thus because the number of granule cells is 1,000,000, we set the number of basket cells to 10,000 (also in agreement with Patton and Mcnaughton 1995). In the CA1 region of the rat hippocampus, the ratio of pyramidal cells to axo-axonic cells (AACs) is estimated to be 200–600:1 (Li et al. 1992), whereas the ratio of granule cells to axo-axonic cells in the dentate is estimated to be in the higher end of this range (Patton and Mcnaughton 1995). Assuming a GC:AAC ratio of 500:1, we estimated the number of axo-axonic cells to be 2,000. Buckmaster and Jongen-Relo (1999) estimated the total number of GAD-mRNA positive neurons in the molecular layer of the dentate gyrus to be about 10,000. Assuming an even distribution between inner-, medial- and outer molecular layers, we estimated that there were 4,000 molecular layer interneurons with axonal arborization in the perforant path termination zone (MOPP cells), with somata located in the inner molecular layer (Han et al. 1993). Note that molecular layer interneurons with a majority of their postsynaptic targets outside the dentate gyrus, like the outer molecular layer interneurons projecting to the subiculum (Ceranik et al. 1997), have not been included. Because the hilar interneurons with axonal arborization in the perforant path termination zone (HIPP cells) are thought to be identical to the somatostatin positive interneurons in the dentate hilus (Freund and Buzsáki 1996; Katona et al. 1999) and because Buckmaster and Jongen-Relo (1999) estimated that there were 12,000 somatostatin-positive neurons in the hilus, we included 12,000 HIPP cells in the dentate network. Hilar interneurons with axonal arborizations in the commissural/associational pathway termination zone (HICAP cells) are thought to be NOS-positive (Freund and Buzsáki 1996). Because roughly 50% of the nearly 7,000 NOS-positive cells in the hilus are single labeled (i.e., not somatostatin/neuroptide-Y or calretinin positive) (Nomura et al. 1997a,b), we estimated the number of HICAP cells in the dentate gyrus to be 3,000. The hilus contains about 6,500 calretinin-positive cells (Nomura et al. 1997a,b), roughly 30% of which are somatostatin-positive (presumably spiny CR positive cells) and some of which overlap with the NOS-positive cells (Nomura et al. 1997a,b). Hilar interneuron-selective cells (IS cells) are aspiny and calretinin-positive (Gulyás et al. 1996), and, assuming that maximally 50% of the calretinin-positive cells are aspiny, we estimated the number of IS cells to be 3,000.

APPENDIX A2: ESTIMATION OF CONNECTIVITY

The connectivity for each cell type is summarized in Table 1 and described below in detail. In the estimates given below, we used a uniform bouton density along the axon of the presynaptic cell, in agreement with the in vivo data in Sik et al. (1997).

Granule cells

Mossy fibers (granule cell axons) in the healthy rat dentate gyrus are primarily restricted to the hilus (97%), with few collaterals (3%) in the granule cell layer (Buckmaster and Dudek 1999). In addition to mossy cells (Acsády et al. 1998), mossy fibers were also shown to contact basket cells (Buckmaster and Schwartzkroin 1994; Geiger et al. 1997) and parvalbumin-positive interneurons (Blasco-Ibanez et al. 2000). With a total of 400–500 synaptic contacts made by a single mossy fiber (Acsády et al. 1998), the 3% of each axon located in the granule cell layer (Buckmaster and Dudek 1999) was estimated to contact 15 basket cells and three axo-axonic cells, assuming no preferential targeting of either interneuron type. In the hilus, a single granule cell was shown to project to seven to 12 mossy cells, forming

large complex mossy fiber boutons (Acsády et al. 1998), whereas an estimated 100–150 mossy fiber terminals target hilar interneurons with approximately one synapse per postsynaptic interneuron (Acsády et al. 1998). Gulyás et al. (1992) estimated that a single spiny CR-positive cell (presumed HIPP cell) is contacted by about 9,000 granule cells. With 12,000 HIPP cells and 1,000,000 GCs, each granule cell is estimated to contact about 110 HIPP cells. The remaining contacts were distributed among HICAP cells (40 contacts). Additionally, in agreement with the presence of mossy fiber terminals on aspiny calretinin-positive interneurons (Acsády et al. 1998), we included 15 mossy fiber synapses to IS cells. Because mossy fibers avoid the molecular layer (Buckmaster and Dudek 1999) in the healthy dentate gyrus, it is assumed that they do not contact MOPP cells. During sclerosis, sprouted mossy fibers were shown to contact ≤500 postsynaptic granule cells (Buckmaster et al. 2002b); thus we estimate an average of 50 to 500 connections from a single granule cell to other granule cells at maximal sclerosis.

Mossy cells

A single filled mossy cell axon was reported to make 35,000 synapses in the inner molecular layer (Buckmaster et al. 1996; Wenzel et al. 1997). Assuming a single synapse per postsynaptic cell, a single mossy cell is estimated to contact 30,000–35,000 granule cells. Of the 2,700 synapses made by a single mossy cell axon in the hilus, about 40% (about 1,000 synapses) target γ-aminobutyric acid (GABA)–negative neurons (Wenzel et al. 1997). Because each mossy cell is estimated to make one to five synaptic contacts on a postsynaptic mossy cell (Buckmaster et al. 1996), we estimate that each mossy cell contacts about 350 other mossy cells. The remaining 60% of the hilar mossy cell axons target GABA-positive cells (Buckmaster et al. 1996; Wenzel et al. 1997), with no reports supporting mossy cell targeting of IS cells. Assuming that there is no preferential target selectivity between HIPP and HICAP cells, and that each postsynaptic hilar interneuron receives two synaptic contacts from a single mossy cell axon (Buckmaster et al. 1996), we estimated that each mossy cell contacted 600 HIPP and 200 HICAP cells. With very low mossy cell to interneuron connectivity in the inner molecular layer (Wenzel et al. 1997), we estimated that each mossy cells contacts five to ten basket and axo-axonic cells and nearly five MOPP cells with somata in the inner molecular layer (Han et al. 1993).

Basket cells

In the CA3 region of the rat hippocampus, each principal cell is contacted by about 200 basket cells (Halasy and Somogyi 1993), whereas it is suggested a granule cell in the dentate is contacted by as few as 30 basket cells. Assuming that each of the 1,000,000 granule cells is contacted by 115 basket cells, each making one to 20 synaptic connections (Acsády et al. 2000; Halasy and Somogyi 1993), we estimated that each basket cell contacted about 1,250 granule cells. Mossy cells receive 10–15 basket cell synapses (Acsády et al. 2000), leading to an estimate of 75 mossy cells contacted by a single basket cell. Roughly 1% of the 11,000 synapses made by a single basket cell axon in the granule cell layer of the dentate are onto other basket cells (Sik et al. 1997) with three to seven synapses per postsynaptic cell (Bartos et al. 2001). Consequently, we estimated that each basket cell in the dentate gyrus contacted 35 other basket cells. Because hilar and molecular layer interneurons are not a major target of basket cells (Halasy and Somogyi 1993), we estimated that a basket cell contacted zero to one HIPP cells (i.e., every second basket cell contacted a HIPP cell). Similarly, the basket cell synapses onto axo-axonic cells, HICAP, and MOPP cells were assumed to be negligible. Because parvalbumin-positive (PV) cells preferentially contact other PV-positive cells in the hilus (Acsády et al. 2000), we assume that basket cells do not contact the calretinin-positive IS cells (Gulyás et al. 1992).

Axo-axonic cells

Most synapses made by axo-axonic cell axons are thought to target granule cell axon initial segments (Halasy and Somogyi 1993), although a small fraction of axon collaterals also descend into the superficial and deep hilus (Freund and Buzsáki 1996; Han et al. 1993). In neocortex, an axo-axonic cell makes four to ten synapses on the postsynaptic cells' axon initial segment (Li et al. 1992). With 22,000,000 estimated axon initial segment synapses in the granule cell layer (Halasy and Somogyi 1993) and assuming four synapses per postsynaptic cell [based on the data from the neocortex from Li et al. (1992)], we estimated that each of the 2,000 axo-axonic cell targeted about 3,000 granule cells. Mossy cells receive axo-axonic cell inhibition (Ribak et al. 1985) and, with the comparatively small fraction of axons from axo-axonic cells in the hilus (Freund and Buzsáki 1996; Han et al. 1993), it was estimated that axo-axonic cells targeted a number of mossy cells equal to about 5% of their granule cell targets, corresponding to 150 mossy cells. Because axo-axonic cells primarily target the axon initial segment of non-GABAergic cells (Freund and Buzsáki 1996; Halasy and Somogyi 1993), we assumed that these cells did not project to interneurons.

HIPP cells

HIPP cells were previously estimated to contact about 1,600 granule and 450 basket cells with one to five synapses per postsynaptic cell (Sik et al. 1997). Mossy cells can have one dendrite in the molecular layer (Buckmaster et al. 1996), which can be targeted by HIPP cell axons, whereas granule cells have two primary dendrites (Claiborne et al. 1990; Lubke et al. 1998). With the mossy cell population corresponding to 1/30 of the granule cell number, the mossy cell dendrites constitute a target for HIPP cells about 1/60 of that of granule cells. Increasing this fraction to about 1/45 to account for the presence of a few HIPP cell contacts on mossy cells in the hilus (Buckmaster et al. 2002a) allowed us to estimate that each HIPP cell contacts about 35 mossy cells. HIPP cell axonal divergence onto HICAP and MOPP cells in the molecular layer was assumed to be similar to that found for somatostatin-positive cells in CA1 (Katona et al. 1999) and set to 15 connections to each population. The HIPP cell axonal divergence to axo-axonic cells was estimated to be between the divergence to basket and HICAP cells and thus the HIPP cell axon was assumed to contact 30 axo-axonic cells.

MOPP cells

MOPP cells target an estimated 7,500 granule cells in the rat dentate gyrus. Although MOPP cells have a horizontal axonal extent similar to that of HIPP cells, they show considerably less branching (Han et al. 1993), leading us to estimate that they contact only half as many MOPP and HICAP cells as HIPP cells. Because MOPP cell axons are restricted to the molecular layer (Han et al. 1993) and do not target the basal dendrites of basket cells, they were assumed to contact <1/10 the number of basket cells targeted by HIPP cells. Likewise, because MOPP cells with axons restricted to the outer and middle molecular layers (Han et al. 1993) would not target the hilar dendrites of axo-axonic cells (Soriano et al. 1990) and the axo-axonic cells with somata and proximal dendrites in the hilus (Han et al. 1993), we estimate that MOPP cells contact only one to two axo-axonic cells. Because the MOPP cell axonal arbors in the molecular layer (Han et al. 1993) do not overlap with major parts of the dendritic arborizations of mossy cells (Frotscher et al. 1991), HIPP cells (Han et al. 1993; Katona et al. 1999; Sik et al. 1997), and IS cells (Gulyás et al. 1996), the connectivity to these cells was deemed negligible.

HICAP cells

Sik et al. (1997) estimated that the septotemporal extent and bouton density of HICAP cell axons was similar to those of HIPP cell axons,

whereas the estimated axonal length of HICAP cells was nearly half that of the HIPP cell axonal length. Thus we estimated that HICAP cells contacted about half the number of granule cells contacted by HIPP cells, although because the HICAP cells have an additional 3% of axon collaterals in the hilus (Sik et al. 1997), their number of postsynaptic mossy cells was assumed to be the same as that of the HIPP cells. HICAP cells were assumed to contact less than half the number of basket cells targeted by HIPP cells (about 175) and a negligible number of axo-axonic cells. With a total of 26,000 from a single HICAP cell axon (Sik et al. 1997), nearly 700 synapses should be present in the hilus. Assuming two to five synapses per postsynaptic cell, each HICAP cell could contact 100–300 hilar cells. We assumed that each HICAP cell targeted 50 HIPP and HICAP cells, which, along with 35 synapses on mossy cells, was in the estimated range. Although the total axonal length of HICAP cells is only about half that of HIPP cells, the number of MOPP cells targeted was assumed to be the same (about 10–20) because the HICAP cell axons primarily project to the inner molecular layer where both cell bodies and proximal dendrites of MOPP cells are located (Han et al. 1993).

IS cells

IS cells contact an estimated 100–800 other IS cells and five to ten (presumably CCK-positive) basket cells (Gulyás et al. 1996). Acsády et al. (2000) suggested that CCK cells would include both BC and HICAP morphologies and that, furthermore, IS cells project to somatostatin-positive presumed HIPP cells. We therefore estimate that IS cells also project to five to ten HICAP cells and HIPP cells.

APPENDIX A3: FITS TO THE EXPERIMENTALLY DETERMINED AXONAL DISTRIBUTIONS

The density of connections made by each neuron type as a function of distance from the soma was assumed to be proportional to the length of axonal branches (Sik et al. 1997). For each cell type, Gaussian distributions were fitted to normalized, binned distributions of data from in vivo fills of the respective cells (Fig. 2). The distribution of sprouted mossy fiber to granule cell connections during sclerosis followed the same distribution as that of the healthy mossy fibers (Buckmaster and Dudek 1999) (Fig. 2*A*). Because of the bimodal distribution of the mossy cell axonal branches (Fig. 2*E*), a single Gaussian was fitted to the average of the length of axonal branches on both sides of the soma and mirrored around the somatic coordinate to give the final fit. No experimental data are available on the axonal distributions of MOPP and IS cells. However, because the horizontal axonal extent of MOPP cells was previously reported to be about 2 mm (Han et al. 1993), they were assigned a distribution based on the average of the basket and HIPP cell axonal distributions. IS cells were assumed to have axonal distributions similar to those of MOPP cells. Note that these axonal distributions are all for ipsilateral projections; for axonal distributions concerning commissural projections, see APPENDIX B2(5) and Fig. 8*A*.

APPENDIX B1: CONTROLS FOR CALCULATING L AND C

To ascertain the robustness of our calculations of L and C in the full-scale structural model of the dentate gyrus, a number of control calculations were performed.

(1) Accuracy of sampling

Because the structural model of dentate gyrus contained a total of 1,064,000 interconnected nodes, it was not computationally feasible to calculate the properties of all nodes. Therefore a minimum of 1/1,000 granule and mossy cells and 1/100 interneurons were sampled randomly, and the weighted averages of L and C were calculated (see METHODS). To ensure the accuracy and stability of this sampling method, control calculations were performed using different random seeds to establish connectivity and randomly sample different subpopulations of cells. Comparison of L and C of the network graphs generated using different random seeds to establish connectivity and/or sampling different cells did not reveal significant differences; in fact, the SD of L and C calculated for these control networks was <0.2%. Additionally, the clustering coefficient calculated for the equivalent random graph of the control dentate gyrus agreed with the theoretical value for a random graph $C = k/n = 0.0011$, where k is the number of connections per node and n is the number of nodes (Watts and Strogatz 1998).

(2) Variations in cell numbers

The small-world structure of the structural model of the dentate gyrus was preserved even when large changes in the estimated cell numbers were introduced. For example, control calculations showed that reducing the number of mossy cells by 50% did not dramatically change the graph structure (L = 2.79, C = 0.0263).

(3) Variations in connectivity estimates

The calculations of L and C presented in this paper were based on the means of connectivity ranges estimated from the literature (Table 1). The small-world structure was preserved even if only the extreme low or the extreme high connectivity estimates (Table 1) were used for the calculation of L and C (extreme low: L = 2.76; C = 0.0163; extreme high: L = 2.62; C = 0.0379), indicating the robustness of the basic findings.

APPENDIX B2: CONTROLS FOR STRUCTURAL PARAMETERS

In five distinct sets of control simulations, we tested the effects of changes in structural parameters on L and C values and network activity, comparing the obtained data to the L and C and activity measures calculated for the base model described in the main part of the paper.

(1) Inhomogeneous distributions of neurons along the septotemporal axis

The density of neurons along the septotemporal axis was previously shown to vary in a cell-type–specific manner in the dentate gyrus. Specifically, the density of granule cells decreases dramatically at the temporal pole (Fricke and Cowan 1978), whereas the densities of mossy cells and hilar interneurons increase at the temporal pole (Buckmaster and Jongen-Relo 1999) (Fig. 7*A*). Calculations of L and C for structural models implementing these inhomogeneous cell distributions along the septotemporal axis did not show any significant differences from the baseline structural model described in the main text (Fig. 7, C_1 and C_2) and the corresponding functional model network with inhomogeneous cell distributions also displayed the characteristic decrease in activity with the progression of sclerosis from 80 to 100% (Fig. 7C_3).

(2) Inhomogeneity in connectivity along the transverse axis

Earlier autoradiographic studies showed that within a given lamella, the density of associational fibers from hilar cells to their molecular layer targets appears to double from the tip of the ventral blade to the tip of the dorsal blade (Fricke and Cowan 1978). This nonuniform projection density in the transverse plane (perpendicular to the septotemporal axis) was modeled by including a linear ventrodorsal scaling in the probability of connecting mossy cells and HIPP cells to their molecular layer targets (e.g., granule cell #10,000 in each bin had

twice the probability of receiving mossy or HICAP cell input compared with granule cell #1). The results obtained with the structural and functional models implementing inhomogeneous connectivity in the transverse plane for either L and C (Fig. 7, C_1 and C_2) or the granule cell activity (Fig. 7C_3) did not show any significant differences from the base model described in the main text.

(3) Axonal distributions at the septal and temporal poles (anatomical boundary)

The cell-type–specific axonal distributions (Fig. 2) were based on in vivo fills obtained from cells situated some distance away from the septal and temporal poles of the dentate gyrus. However, the structural and functional model networks contained cells whose axons reached these boundaries. Because it is not known how the axonal distributions are skewed at the two poles of the biological dentate gyrus, control simulations with four different boundary conditions were implemented affecting all cell types, resulting in the conservation or reduction of the septotemporal span (i.e., the tail-to-tail width) of the Gaussians shown in Fig. 2, and the conservation or reduction of the total axonal length (i.e., the area under the Gaussians; note that the total axonal length corresponds to the total number of connections): *1*) reduced septotemporal span, reduced total axonal length (i.e., the axons beyond the anatomical boundary were simply cut off and not preserved; this was the baseline method used for all simulations described in RESULTS); *2*) reduced septotemporal span, conserved total axonal length (i.e., higher density of axons in the arbor that remained after the cutoff at the boundary); *3*) conserved septotemporal span, conserved total axonal length; *4*) conserved septotemporal span, reduced axonal length. These four boundary conditions are illustrated for the case of a granule cell situated at the septal pole of the dentate gyrus in Fig. 7*B*. The results of these control calculations showed that the L and C values obtained for the three additional boundary conditions were similar to the L and C values calculated for the baseline case (reduced septotemporal span, reduced total axonal length) used in the rest of the paper (Fig. 7, C_1 and C_2). Similarly, the networks with the distinct boundary conditions all showed the characteristic decrease in activity as sclerosis progressed from 80 to 100% (Fig. 7C_3). Therefore these anatomical boundary controls further support the robustness of our main results.

(4) Offset degrees of sprouting and hilar neuron loss

A strong correlation between the degree of hilar neuron loss and mossy fiber sprouting was previously reported in both specimens from patients with temporal lobe epilepsy (Gabriel et al. 2004) and animal models (Nadler and Jiao 2004). However, to test whether a potential offset in the degrees of sprouting and hilar cell loss would affect our main conclusions, control calculations with sprouting lagging 20% behind the hilar neuron loss were performed (70% sprouting with 90% cell loss, 80% sprouting with 100% cell loss). These calculations did not show any significant differences from the baseline model described in the main text (Fig. 7, C_1–C_3).

(5) Bilateral model of the dentate with commissural projections

The full-scale structural model consisted of only one side of the dentate gyrus (and, consequently, contained only ipsilateral, associational connections). To test whether the main findings of the paper (on L and C and the biphasic activity) also apply when both sides of the dentate gyrus are taken into account, bilateral structural and functional model networks were implemented. For both the structural and functional bilateral models, two individual unilateral models were implemented and anatomically realistic commissural connections were established between them (Table B1). Cell-type specificity of the commissural projections and their axonal distributions (Fig. 8*A*) were constrained based on data from studies using anterograde tracer techniques (reviewed in Deller 1998). Briefly, *1*) because mossy fibers do not cross the commissure (Blackstad et al. 1970; Zappone and

TABLE B1. *Connectivity matrix for commissural projections of the control dentate gyrus*

	% Commisural Projections	Granule Cells	Mossy Cells	Basket Cells	Axo-axonic Cells	MOPP Cells	HIPP Cells	HICAP Cells	IS Cells
Granule cells	**0%**	**X**	**X**	**X**	**X**	**X**	**X**	**X**	**X**
(1,000,000)	ref. [1,2]	X	X	X	X	X	X	X	X
Mossy cells	**100%**	**22,500**	**X**	**6**	**6**	**X**	**X**	**X**	**X**
(30,000)		15,000–30,000	X	2–10	2–10	X	X	X	X
	ref. [3,4]	ref. [5–7]	ref. [4,8]	ref. [5–7]	ref. [5–7]		ref. [4,8]	ref. [4,8]	ref. [4,8]
Basket cells	**38%**	**400**	X	10	X	X	X	X	X
(10,000)		400	X	10	X	X	X	X	X
	ref. [2]	ref. [8]		ref. [8]					
Axo-axonic cells	**38%**	**1000**	**X**	**X**	**X**	**X**	**X**	**X**	**X**
(2,000)		1000	X	X	X	X	X	X	X
	ref. [2]	ref. [8]	ref. [4,8]						
MOPP cells	**0%**	**X**	**X**	**X**	**X**	**X**	**X**	**X**	**X**
(4,000)		X	X	X	X	X	X	X	X
	ref. [2]								
HIPP cells	**98%**	**400**	**X**	**40**	**X**	**4**	**X**	**X**	**X**
(12,000)		400	X	40	X	4	X	X	X
	ref. [2]	ref. [8]	ref. [4,8]	ref. [8]		ref. [8]	ref. [4,8]	ref. [4,8]	ref. [4,8]
HICAP cells	**0%**	**X**	**X**	**X**	**X**	**X**	**X**	**X**	**X**
(3,000)		X	X	X	X	X	X	X	X
IS cells	**33%**	**X**	**X**	**3**	**X**	**X**	**X**	**X**	**X**
(3,000)		X	X	3	X	X	X	X	X
	ref. [2]			ref. [4,8]			ref. [4,8]	ref. [4,8]	ref. [4,8]

Connectivity values were estimated from published data [see APPENDIX B2(5)] and are given as number of connections to the contralateral postsynaptic population (*row 1*) from a single presynaptic neuron (*column 1*). The fraction of a population projecting contralaterally and the average number of connections used in the graph theoretical calculations are given in bold. References given correspond to: [1]Blackstad et al. (1970); [2]Zappone and Sloviter (2001); [3]Frotscher et al. (1991); [4]Deller (1998); [5]Deller et al. (1994); [6]Fricke and Cowan (1978); [7]Seress and Ribak (1984); [8]Deller et al. (1995a).

Sloviter 2001), granule cells were modeled without contralateral projections. 2) Mossy cells have extensive commissural projections (Frotscher et al. 1991) with almost all cells projecting bilaterally (Deller 1998). Similar to their ipsilateral side, the commissural projections of mossy cells terminate exclusively in the inner molecular layer and on both granule cells and parvalbumin-positive interneurons (Deller et al. 1994; Seress and Ribak 1984). In agreement with tracer studies demonstrating similar densities and longitudinal extent for both associational and commissural projections to the inner molecular layer (Fricke and Cowan 1978), the number and septotemporal span of the ipsilateral distribution of mossy cell axons were conserved on the contralateral side. However, commissural contacts of the mossy cell axons were restricted to the molecular layer because they are known to avoid synaptic contacts in the hilus (Deller 1998; Deller et al. 1995b). In contrast to the bimodal ipsilateral distribution, the contralateral distribution of mossy cell axons is unimodal with the maximal density in the homotopic contralateral lamella (Deller 1998). Therefore the commissural axonal distribution of mossy cells was described by a single Gaussian (Fig. 8*A*) with the same septotemporal width as the ipsilateral mossy fiber axons (Fig. 2), with the peak located in the contralateral lamella homotopic to the soma. *3*) Previous studies showed that nearly 38% of parvalbumin cells, nearly 98% somatostatin cells, and nearly 33% of calretinin interneurons in the dentate project contralaterally (Zappone and Sloviter 2001). Additionally, with the exception of avoiding hilar targets, the cell-type specificity of the interneuronal axonal termination zone is preserved in contralateral projections (Deller et al. 1995b). Therefore we included contralateral projections from basket cells, axo-axonic cells, HIPP cells, and IS cells to their appropriate targets in the bilateral network (Table B1). However, in keeping with the more restricted septotemporal span of the interneuronal contralateral projections (Deller et al. 1995a,b) we reduced the number of contacts and longitudinal extent of commissural terminals (Fig. 8*A*) compared with the corresponding associational connections (Fig. 2).

To test whether the biphasic change in network hyperexcitability was present in a bilateral dentate gyrus, a bilateral functional model network was also implemented, by scaling down the connectivity of the bilateral structural model in exactly the same way as for the ipsilateral model, resulting in a bilateral functional model with 100,000+ cells (containing the various cell types in anatomically realistic proportions, as in the ipsilateral model). The commissural connection strengths and kinetics were assumed to be identical to those for the ispilateral model (Table 2). Because of the additional inputs to granule cells from spontaneously active contralateral mossy cells, the bilateral functional model network showed greater granule cell discharge activity (Fig. 8B_1) than that of the unilateral model after perforant path stimulation at 0% sclerosis. However, in agreement with the low firing frequency of biological granule cells (Santhakumar et al. 2005), 87.3% of granule cells did not spike and the average firing frequency of granule cells remained low (0.27 Hz) at 0% sclerosis even in the bilateral model (as illustrated by the similar activity measures for the bilateral and base models at 0% sclerosis in Fig. 8C_3).

The results of these bilateral control simulations showed that the L and C characteristics of the bilateral network with >2 million nodes and possessing both commissural and associational links were virtually identical to the L and C values calculated for the ipsilateral structural network (Fig. 8, C_1 and C_2). Futhermore, the bilateral functional model network also displayed the characteristic drop in activity as sclerosis progressed from 80 to 100% (Fig. 8, B_2, B_3, and C_3). Note that the hyperactivity in the bilateral model at 100% sclerosis did not spread to the contralateral side (Fig. 8B_3), arising from the complete loss of mossy cells, resulting in an even more pronounced decrease in the overall granule cell firing at 100% sclerosis in the bilateral network than in the ipsilateral base model (compare open and filled circles in Fig. 8C_3).

APPENDIX B3: CONTROLS FOR FUNCTIONAL PARAMETERS

In addition to simulations testing the effects of changes in the structural model (described above), three sets of control simulations were performed to determine the effects of varying specific parameters in the functional network model. In all cases, we tested how large parameter changes affect the biphasic nature of the changes in hyperexcitability during sclerosis.

(1) Double inhibition

Stemming from the lack of sufficiently detailed data on four interneuron types, only the two major somatically and dendritically projecting interneuronal classes (basket and HIPP cells) were included in the functional model network, effectively removing nearly 50% of the inhibitory connections (see Table 1). Therefore control simulations were carried out to determine if large increases in inhibition in the network alter the basic conclusions. As illustrated in Fig. 9, A_1–A_3 (and summarized in Fig. 9*D*), the biphasic changes in network activity in the functional model during sclerosis persisted even after doubling of the maximal conductances of all inhibitory synapses (base values listed in Table 2). Therefore these data indicate that the main conclusions do not depend on the strength of inhibition included in the functional model.

(2) Axonal conduction delay

In the baseline network model described in the main text, a fixed, connection-type–specific synaptic delay was used (Santhakumar et al. 2005). In additional control simulations, an axonal conduction velocity of 0.25 m/s (Bartos et al. 2002) was used to add distance-dependent delays to connections made outside the 60-μm bin of the presynaptic neuron. This resulted in an additional 0.24-ms delay for each bin separating the pre- and postsynaptic cells. As illustrated in Fig. 9, B_1–B_3 (and summarized in Fig. 9*D*), these simulations with distance-dependent delays displayed biphasic changes in network activity during sclerosis similar to those in networks with fixed synaptic delays. These data also support the robustness of our conclusions.

(3) Spontaneous instead of stimulation-evoked activity

In most simulations, a perforant path stimulus was used to investigate the functional consequences of network architectural changes. To show that the main conclusions were stimulus independent, spontaneous network activity, simulated by uncorrelated activation of each granule cell, each basket cell and 100 evenly distributed mossy cells was implemented by assigning individual perforant path inputs with Poisson-distributed interspike intervals. As illustrated in Fig. 9, C_1–C_3 (and summarized in Fig. 9*D*), these simulations revealed the characteristic biphasic changes in activity with sclerosis: the average granule cell activity showed a peak at 80% sclerosis, followed by a decrease at 100% sclerosis. Therefore the main conclusions were not dependent on the specific parameters of the stimulus.

ACKNOWLEDGMENTS

The authors are grateful to Drs. P. Somogyi, T. F. Freund, and A. Gulyás for advice on the dentate connectivity matrix, and to Drs. M. I. Rabinovich and A. Howard and E. Klinger for discussions.

GRANTS

This work was supported by National Institute of Neurological Disorders and Stroke Grant NS-35915 to I. Soltesz.

REFERENCES

Achard S, Salvador R, Whitcher B, Suckling J, Bullmore E. A resilient, low-frequency, small-world human brain functional network with highly connected association cortical hubs. *J Neurosci* 26: 63–72, 2006.

Acsády L, Kamondi A, Sik A, Freund T, Buzsáki G. GABAergic cells are the major postsynaptic targets of mossy fibers in the rat hippocampus. *J Neurosci* 18: 3386–3403, 1998.

Acsády L, Katona I, Martinez-Guijarro FJ, Buzsáki G, Freund TF. Unusual target selectivity of perisomatic inhibitory cells in the hilar region of the rat hippocampus. *J Neurosci* 20: 6907–6919, 2000.

Albert R, Jeong H, Barabási AL. Internet—diameter of the world-wide web. *Nature* 401: 130–131, 1999.

Andre V, Marescaux C, Nehlig A, Fritschy JM. Alterations of hippocampal GABAergic system contribute to development of spontaneous recurrent seizures in the rat lithium-pilocarpine model of temporal lobe epilepsy. *Hippocampus* 11: 452–468, 2001.

Aradi I, Holmes WR. Role of multiple calcium and calcium-dependent conductances in regulation of hippocampal dentate granule cell excitability. *J Comput Neurosci* 6: 215–235, 1999.

Ascoli GA, Atkeson JC. Incorporating anatomically realistic cellular-level connectivity in neural network models of the rat hippocampus. *Biosystems* 79: 173–181, 2005.

Babb TL, Pretorius JK, Kupfer WR, Brown WJ. Distribution of glutamate-decarboxylase-immunoreactive neurons and synapses in the rat and monkey hippocampus—light and electron-microscopy. *J Comp Neurol* 278: 121–138, 1988.

Barabási AL, Albert R, Jeong H. Scale-free characteristics of random networks: the topology of the world-wide web. *Physica A* 281: 69–77, 2000.

Barahona M, Pecora LM. Synchronization in small-world systems. *Phys Rev Lett* 89: 054101, 2002.

Bartos M, Vida I, Frotscher M, Geiger JRP, Jonas P. Rapid signaling at inhibitory synapses in a dentate gyrus interneuron network. *J Neurosci* 21: 2687–2698, 2001.

Bartos M, Vida I, Frotscher M, Meyer A, Monyer H, Geiger JRP, Jonas P. Fast synaptic inhibition promotes synchronized gamma oscillations in hippocampal interneuron networks. *Proc Natl Acad Sci USA* 99: 13222–13227, 2002.

Bernard C, Cannon RC, Ben Ari Y, Wheal HV. Model of spatio-temporal propagation of action potentials in the Schaffer collateral pathway of the CA1 area of the rat hippocampus. *Hippocampus* 7: 58–72, 1997.

Blackstad TW, Brink K, Hem J, Jeune B. Distribution of hippocampal mossy fibers in the rat. An experimental study with silver impregnation methods. *J Comp Neurol* 138: 433–449, 1970.

Blasco-Ibanez JM, Martinez-Guijarro FJ, Freund TF. Recurrent mossy fibers preferentially innervate parvalbumin-immunoreactive interneurons in the granule cell layer of the rat dentate gyrus. *Neuroreport* 11: 3219–3225, 2000.

Blumcke I, Suter B, Behle K, Kuhn R, Schramm J, Elger CE, Wiestler OD. Loss of hilar mossy cells in Ammon's horn sclerosis. *Epilepsia* 41, *Suppl.* 6: S174–S180, 2000.

Boss BD, Peterson GM, Cowan WM. On the number of neurons in the dentate gyrus of the rat. *Brain Res* 338: 144–150, 1985.

Buckmaster PS, Dudek FE. Network properties of the dentate gyrus in epileptic rats with hilar neuron loss and granule cell axon reorganization. *J Neurophysiol* 77: 2685–2696, 1997.

Buckmaster PS, Dudek FE. In vivo intracellular analysis of granule cell axon reorganization in epileptic rats. *J Neurophysiol* 81: 712–721, 1999.

Buckmaster PS, Jongen-Relo AL. Highly specific neuron loss preserves lateral inhibitory circuits in the dentate gyrus of kainate-induced epileptic rats. *J Neurosci* 19: 9519–9529, 1999.

Buckmaster PS, Schwartzkroin PA. Hippocampal mossy cell function: a speculative view. *Hippocampus* 4: 393–402, 1994.

Buckmaster PS, Strowbridge BW, Kunkel DD, Schmiege DL, Schwartzkroin PA. Mossy cell axonal projections to the dentate gyrus molecular layer in the rat hippocampal slice. *Hippocampus* 2: 349–362, 1992.

Buckmaster PS, Wenzel HJ, Kunkel DD, Schwartzkroin PA. Axon arbors and synaptic connections of hippocampal mossy cells in the rat in vivo. *J Comp Neurol* 366: 270–292, 1996.

Buckmaster PS, Yamawaki R, Zhang GF. Axon arbors and synaptic connections of a vulnerable population of interneurons in the dentate gyrus in vivo. *J Comp Neurol* 445: 360–373, 2002a.

Buckmaster PS, Zhang GF, Yamawaki R. Axon sprouting in a model of temporal lobe epilepsy creates a predominantly excitatory feedback circuit. *J Neurosci* 22: 6650–6658, 2002b.

Buzsáki G, Geisler C, Henze DA, Wang XJ. Interneuron diversity series: circuit complexity and axon wiring economy of cortical interneurons. *Trends Neurosci* 27: 186–193, 2004.

Cavazos JE, Das I, Sutula TP. Neuronal loss induced in limbic pathways by kindling: evidence for induction of hippocampal sclerosis by repeated brief seizures. *J Neurosci* 14: 3106–3121, 1994.

Cavazos JE, Sutula TP. Progressive neuronal loss induced by kindling: a possible mechanism for mossy fiber synaptic reorganization and hippocampal sclerosis. *Brain Res* 527: 1–6, 1990.

Ceranik K, Bender R, Geiger JRP, Monyer H, Jonas P, Frotscher M, Lubke J. A novel type of GABAergic interneuron connecting the input and the output regions of the hippocampus. *J Neurosci* 17: 5380–5394, 1997.

Claiborne BJ, Amaral DG, Cowan WM. Quantitative, three-dimensional analysis of granule cell dendrites in the rat dentate gyrus. *J Comp Neurol* 302: 206–219, 1990.

Deller T. The anatomical organization of the rat fascia dentata: new aspects of laminar organization as revealed by anterograde tracing with Phaseolus vulgaris-leucoagglutinin (PHAL). *Anat Embryol (Berl)* 197: 89–103, 1998.

Deller T, Frotscher M, Nitsch R. Morphological evidence for the sprouting of inhibitory commissural fibers in response to the lesion of the excitatory entorhinal input to the rat dentate gyrus. *J Neurosci* 15: 6868–6878, 1995a.

Deller T, Nitsch R, Frotscher M. Associational and commissural afferents of parvalbumin-immunoreactive neurons in the rat hippocampus: a combined immunocytochemical and PHA-L study. *J Comp Neurol* 350: 612–622, 1994.

Deller T, Nitsch R, Frotscher M. Phaseolus vulgaris-leucoagglutinin tracing of commissural fibers to the rat dentate gyrus: evidence for a previously unknown commissural projection to the outer molecular layer. *J Comp Neurol* 352: 55–68, 1995b.

Esclapez M, Houser CR. Up-regulation of GAD65 and GAD67 in remaining hippocampal GABA neurons in a model of temporal lobe epilepsy. *J Comp Neurol* 412: 488–505, 1999.

Eubank S, Guclu H, Kumar VS, Marathe MV, Srinivasan A, Toroczkai Z, Wang N. Modelling disease outbreaks in realistic urban social networks. *Nature* 429: 180–184, 2004.

Foldy C, Aradi I, Howard A, Soltesz I. Diversity beyond variance: modulation of firing rates and network coherence by GABAergic subpopulations. *Eur J Neurosci* 19: 119–130, 2004.

Freund TF, Buzsáki G. Interneurons of the hippocampus. *Hippocampus* 6: 347–470, 1996.

Fricke R, Cowan WM. An autoradiographic study of the commissural and ipsilateral hippocampo-dentate projections in the adult rat. *J Comp Neurol* 181: 253–269, 1978.

Frotscher M, Seress L, Schwerdtfeger WK, Buhl E. The mossy cells of the fascia dentata: a comparative study of their fine structure and synaptic connections in rodents and primates. *J Comp Neurol* 312: 145–163, 1991.

Gaarskjaer FB. Organization of mossy fiber system of rat studied in extended hippocampi. 1. Terminal area related to number of granule and pyramidal cells. *J Comp Neurol* 178: 49–71, 1978.

Gabriel S, Njunting M, Pomper JK, Merschhemke M, Sanabria ERG, Eilers A, Kivi A, Zeller M, Meencke H-J, Cavalheiro EA, Heinemann U, Lehmann T-N. Stimulus and potassium-induced epileptiform activity in the human dentate gyrus from patients with and without hippocampal sclerosis. *J Neurosci* 24: 10416–10430, 2004.

Geiger JRP, Lubke J, Roth A, Frotscher M, Jonas P. Submillisecond AMPA receptor-mediated signaling at a principal neuron-interneuron synapse. *Neuron* 18: 1009–1023, 1997.

Gorter JA, van Vliet EA, Aronica E, Lopes da Silva FH. Progression of spontaneous seizures after status epilepticus is associated with mossy fibre sprouting and extensive bilateral loss of hilar parvalbumin and somatostatin-immunoreactive neurons. *Eur J Neurosci* 13: 657–669, 2001.

Gulyás AI, Hajos N, Freund TF. Interneurons containing calretinin are specialized to control other interneurons in the rat hippocampus. *J Neurosci* 16: 3397–3411, 1996.

Gulyás AI, Miettinen R, Jacobowitz DM, Freund TF. Calretinin is present in nonpyramidal cells of the rat hippocampus. 1. A new type of neuron specifically associated with the mossy fiber system. *Neuroscience* 48: 1–27, 1992.

Halasy K, Somogyi P. Subdivisions in the multiple GABAergic innervation of granule cells in the dentate gyrus of the rat hippocampus. *Eur J Neurosci* 5: 411–429, 1993.

Han ZS, Buhl EH, Lorinczi Z, Somogyi P. A high-degree of spatial selectivity in the axonal and dendritic domains of physiologically identified local-circuit neurons in the dentate gyrus of the rat hippocampus. *Eur J Neurosci* 5: 395–410, 1993.

Hines ML, Carnevale NT. The NEURON simulation environment. *Neural Comput* 9: 1179–1209, 1997.

Jeong H, Tombor B, Albert R, Oltvai ZN, Barabási AL. The large-scale organization of metabolic networks. *Nature* 407: 651–654, 2000.

Katona I, Acsády L, Freund TF. Postsynaptic targets of somatostatin-immunoreactive interneurons in the rat hippocampus. *Neuroscience* 88: 37–55, 1999.

Lago-Fernandez LF, Huerta R, Corbacho F, Siguenza JA. Fast response and temporal coherent oscillations in small-world networks. *Phys Rev Lett* 84: 2758–2761, 2000.

Leite JP, Babb TL, Pretorius JK, Kuhlman PA, Yeoman KM, Mathern GW. Neuron loss, mossy fiber sprouting, and interictal spikes after intrahippocampal kainate in developing rats. *Epilepsy Res* 26: 219–231, 1996.

Li C, Chen G. Stability of a neural network model with small-world connections. *Phys Rev E Stat Nonlin Soft Matter Phys* 68: 052901, 2003.

Li XG, Somogyi P, Tepper JM, Buzsáki G. Axonal and dendritic arborization of an intracellularly labeled chandelier cell in the CA1 region of rat hippocampus. *Exp Brain Res* 90: 519–525, 1992.

Lin M, Chen T. Self-organized criticality in a simple model of neurons based on small-world networks. *Phys Rev E Stat Nonlin Soft Matter Phys* 71: 016133, 2005.

Longo B, Covolan L, Chadi G, Mello LE. Sprouting of mossy fibers and the vacating of postsynaptic targets in the inner molecular layer of the dentate gyrus. *Exp Neurol* 181: 57–67, 2003.

Lowenstein DH, Thomas MJ, Smith DH, McIntosh TK. Selective vulnerability of dentate hilar neurons following traumatic brain injury: a potential mechanistic link between head trauma and disorders of the hippocampus. *J Neurosci* 12: 4846–4853, 1992.

Lubke J, Frotscher M, Spruston N. Specialized electrophysiological properties of anatomically identified neurons in the hilar region of the rat fascia dentata. *J Neurophysiol* 79: 1518–1534, 1998.

Margerison JH, Corsellis JA. Epilepsy and the temporal lobes. A clinical, electroencephalographic and neuropathological study of the brain in epilepsy, with particular reference to the temporal lobes. *Brain* 89: 499–530, 1966.

Masuda N, Aihara K. Global and local synchrony of coupled neurons in small-world networks. *Biol Cybern* 90: 302–309, 2004.

Mathern GW, Babb TL, Leite JP, Pretorius K, Yeoman KM, Kuhlman PA. The pathogenic and progressive features of chronic human hippocampal epilepsy. *Epilepsy Res* 26: 151–161, 1996.

Mathern GW, Bertram EH 3rd, Babb TL, Pretorius JK, Kuhlman PA, Spradlin S, Mendoza D. In contrast to kindled seizures, the frequency of spontaneous epilepsy in the limbic status model correlates with greater aberrant fascia dentata excitatory and inhibitory axon sprouting, and increased staining for N-methyl-D-aspartate, AMPA and GABA(A) receptors. *Neuroscience* 77: 1003–1019, 1997.

Milo R, Shen-Orr S, Itzkovitz S, Kashtan N, Chklovskii D, Alon U. Network motifs: simple building blocks of complex networks. *Science* 298: 824–827, 2002.

Nadler JV. The recurrent mossy fiber pathway of the epileptic brain. *Neurochem Res* 28: 1649–1658, 2003.

Nadler JV, Jiao Y. Mossy fiber sprouting correlates with loss of GluR2-immunoreactive hilar neurons. Program No. 566.521. San Diego, CA: Society for Neuroscience, 2004.

Netoff TI, Clewley R, Arno S, Keck T, White JA. Epilepsy in small-world networks. *J Neurosci* 24: 8075–8083, 2004.

Nomura T, Fukuda T, Aika Y, Heizmann CW, Emson PC, Kobayashi T, Kosaka T. Distribution of nonprincipal neurons in the rat hippocampus, with special reference to their dorsoventral difference. *Brain Res* 751: 64–80, 1997a.

Nomura T, Fukuda T, Aika Y, Heizmann CW, Emson PC, Kobayashi T, Kosaka T. Laminar distribution of non-principal neurons in the rat hippocampus, with special reference to their compositional difference among layers. *Brain Res* 764: 197–204, 1997b.

Patton PE, Mcnaughton B. Connection matrix of the hippocampal-formation. 1. The dentate gyrus. *Hippocampus* 5: 245–286, 1995.

Percha B, Dzakpasu R, Zochowski M, Parent J. Transition from local to global phase synchrony in small world neural network and its possible implications for epilepsy. *Phys Rev E Stat Nonlin Soft Matter Phys* 72: 031909, 2005.

Rafiq A, Zhang YF, DeLorenzo RJ, Coulter DA. Long-duration self-sustained epileptiform activity in the hippocampal-parahippocampal slice: a model of status epilepticus. *J Neurophysiol* 74: 2028–2042, 1995.

Ratzliff AH, Howard AL, Santhakumar V, Osapay I, Soltesz I. Rapid deletion of mossy cells does not result in a hyperexcitable dentate gyrus: implications for epileptogenesis. *J Neurosci* 24: 2259–2269, 2004.

Ratzliff AH, Santhakumar V, Howard A, Soltesz I. Mossy cells in epilepsy: rigor mortis or vigor mortis? *Trends Neurosci* 25: 140–144, 2002.

Reigl M, Alon U, Chklovskii DB. Search for computational modules in the C. elegans brain. *BMC Biol* 2: 25, 2004.

Ribak CE, Seress L, Amaral DG. The development, ultrastructure and synaptic connections of the mossy cells of the dentate gyrus. *J Neurocytol* 14: 835–857, 1985.

Roxin A, Riecke H, Solla SA. Self-sustained activity in a small-world network of excitable neurons. *Phys Rev Lett* 92: 198101, 2004.

Santhakumar V, Aradi I, Soltesz I. Role of mossy fiber sprouting and mossy cell loss in hyperexcitability: a network model of the dentate gyrus incorporating cell types and axonal topography. *J Neurophysiol* 93: 437–453, 2005.

Santhakumar V, Ratzliff AD, Jeng J, Toth Z, Soltesz I. Long-term hyperexcitability in the hippocampus after experimental head trauma. *Ann Neurol* 50: 708–717, 2001.

Scharfman HE. Dentate hilar cells with dendrites in the molecular layer have lower thresholds for synaptic activation by perforant path than granule cells. *J Neurosci* 11: 1660–1673, 1991.

Seress L, Ribak CE. Direct commissural connections to the basket cells of the hippocampal dentate gyrus: anatomical evidence for feed-forward inhibition. *J Neurocytol* 13: 215–225, 1984.

Shefi O, Golding I, Segev R, Ben-Jacob E, Ayali A. Morphological characterization of in vitro neuronal networks. *Phys Rev E Stat Nonlin Soft Matter Phys* 66: 021905, 2002.

Sik A, Penttonen M, Buzsáki G. Interneurons in the hippocampal dentate gyrus: an in vivo intracellular study. *Eur J Neurosci* 9: 573–588, 1997.

Sik A, Ylinen A, Penttonen M, Buzsáki G. Inhibitory CA1-CA3-hilar region feedback in the hippocampus. *Science* 265: 1722–1724, 1994.

Soltesz I. *Diversity in the Neuronal Machine—Order and Variability in Interneuronal Microcircuits*. New York: Oxford Univ. Press, 2006.

Song S, Sjostrom PJ, Reigl M, Nelson S, Chklovskii DB. Highly nonrandom features of synaptic connectivity in local cortical circuits. *PLoS Biol* 3: e68, 2005.

Soriano E, Nitsch R, Frotscher M. Axo-axonic chandelier cells in the rat fascia dentata: Golgi-electron microscopy and immunocytochemical studies. *J Comp Neurol* 293: 1–25, 1990.

Sporns O, Kotter R. Motifs in brain networks. *PLoS Biol* 2: e369, 2004.

Sporns O, Zwi JD. The small world of the cerebral cortex. *Neuroinformatics* 2: 145–162, 2004.

Staley KJ, Otis TS, Mody I. Membrane properties of dentate gyrus granule cells: comparison of sharp microelectrode and whole-cell recordings. *J Neurophysiol* 67: 1346–1358, 1992.

Stephan KE, Hilgetag CC, Burns GA, O'Neill MA, Young MP, Kotter R. Computational analysis of functional connectivity between areas of primate cerebral cortex. *Philos Trans R Soc Lond B Biol Sci* 355: 111–126, 2000.

Sutula TP, Hagen J, Pitkanen A. Do epileptic seizures damage the brain? *Curr Opin Neurol* 16: 189–195, 2003.

Toth Z, Hollrigel GS, Gorcs T, Soltesz I. Instantaneous perturbation of dentate interneuronal networks by a pressure wave-transient delivered to the neocortex. *J Neurosci* 17: 8106–8117, 1997.

Traub RD, Contreras D, Cunningham MO, Murray H, LeBeau FE, Roopun A, Bibbig A, Wilent WB, Higley MJ, Whittington MA. Single-column thalamocortical network model exhibiting gamma oscillations, sleep spindles, and epileptogenic bursts. *J Neurophysiol* 93: 2194–2232, 2005a.

Traub RD, Pais I, Bibbig A, Lebeau FE, Buhl EH, Garner H, Monyer H, Whittington MA. Transient depression of excitatory synapses on interneurons contributes to epileptiform bursts during gamma oscillations in the mouse hippocampal slice. *J Neurophysiol* 94: 1225–1235, 2005b.

van Vliet EA, Aronica E, Tolner EA, Lopes da Silva FH, Gorter JA. Progression of temporal lobe epilepsy in the rat is associated with immunocytochemical changes in inhibitory interneurons in specific regions of the hippocampal formation. *Exp Neurol* 187: 367–379, 2004.

Watts DJ, Strogatz SH. Collective dynamics of "small-world" networks. *Nature* 393: 440–442, 1998.

Wenzel HJ, Buckmaster PS, Anderson NL, Wenzel ME, Schwartzkroin PA. Ultrastructural localization of neurotransmitter immunoreactivity in mossy cell axons and their synaptic targets in the rat dentate gyrus. *Hippocampus* 7: 559–570, 1997.

West MJ. Stereological studies of the hippocampus—a comparison of the hippocampal subdivisions of diverse species including hedgehogs, laboratory rodents, wild mice and men. *Prog Brain Res* 83: 13–36, 1990.

West MJ, Danscher G, Gydesen H. A determination of the volumes of the layers of the rat hippocampal region. *Cell Tissue Res* 188: 345–359, 1978.

White JA, Chow CC, Ritt J, Soto-Treviño C, Kopell N. Synchronization and oscillatory dynamics in heterogeneous, mutually inhibited neurons. *J Comput Neurosci* 5: 5–16, 1998.

Woodson W, Nitecka L, Benari Y. Organization of the GABAergic system in the rat hippocampal-formation—a quantitative immunocytochemical study. *J Comp Neurol* 280: 254–271, 1989.

Yoshimura Y, Callaway EM. Fine-scale specificity of cortical networks depends on inhibitory cell type and connectivity. *Nat Neurosci* 8: 1552–1559, 2005.

Yoshimura Y, Dantzker JL, Callaway EM. Excitatory cortical neurons form fine-scale functional networks. *Nature* 433: 868–873, 2005.

Zappone CA, Sloviter RS. Commissurally projecting inhibitory interneurons of the rat hippocampal dentate gyrus: a colocalization study of neuronal markers and the retrograde tracer Fluoro-gold. *J Comp Neurol* 441: 324–344, 2001.

Zappone CA, Sloviter RS. Translamellar disinhibition in the rat hippocampal dentate gyrus after seizure-induced degeneration of vulnerable hilar neurons. *J Neurosci* 24: 853–864, 2004.

Internetwork and intranetwork communications during bursting dynamics: Applications to seizure prediction

S. Feldt,[1,*] H. Osterhage,[2,3] F. Mormann,[2,4] K. Lehnertz,[2,3,5] and M. Żochowski[1,6]
[1]*Department of Physics, University of Michigan, Ann Arbor, Michigan 48109, USA*
[2]*Department of Epileptology, University of Bonn, Bonn, Germany*
[3]*Helmholtz-Institute for Radiation and Nuclear Physics, University of Bonn, Bonn, Germany*
[4]*California Institute of Technology, Division of Biology, 216-76, Pasadena, CA 91125, USA*
[5]*Interdisciplinary Center for Complex Systems, University of Bonn, Bonn, Germany*
[6]*Biophysics Research Division, University of Michigan, Ann Arbor, Michigan 48109, USA*
(Received 9 March 2007; revised manuscript received 23 May 2007; published 20 August 2007)

We use a simple dynamical model of two interacting networks of integrate-and-fire neurons to explain a seemingly paradoxical result observed in epileptic patients indicating that the level of phase synchrony declines below normal levels during the state preceding seizures (preictal state). We model the transition from the seizure free interval (interictal state) to the seizure (ictal state) as a slow increase in the mean depolarization of neurons in a network corresponding to the epileptic focus. We show that the transition from the interictal to preictal and then to the ictal state may be divided into separate dynamical regimes: the formation of slow oscillatory activity due to resonance between the two interacting networks observed during the interictal period, structureless activity during the preictal period when the two networks have different properties, and bursting dynamics driven by the network corresponding to the epileptic focus. Based on this result, we hypothesize that the beginning of the preictal period marks the beginning of the transition of the epileptic network from normal activity toward seizing.

DOI: 10.1103/PhysRevE.76.021920 PACS number(s): 87.18.Hf, 87.18.Sn, 05.45.Xt

I. INTRODUCTION

Epilepsy, one of the most common neurological disorders, is characterized by the sudden onset of recurrent seizures due to a hypersynchronous firing of populations of neurons. Due to the debilitating nature of seizures and the fact that approximately 1% of the world population suffers from epilepsy, much research has investigated the dynamics of the onset of seizures with the hopes of developing methods of seizure prediction [1]. One of the most common types of epilepsy is focal epilepsy in which seizures originate from a circumscribed region within the brain. Since only about 2/3 of epilepsy patients will respond to medication, surgery to remove the focal region is another option for treatment [2]. In order to locate the focus, clinicians rely on information from electroencephalogram (EEG) recordings combined with various imaging techniques. The availability of EEG data from these patients has allowed researchers to study the dynamics of the EEG signal before and during a seizure in hopes of better understanding the seizure generating process with the ultimate goal of predicting seizures.

Through the analysis of EEG recordings, it has recently been shown that one can identify a preictal period before the onset of a seizure during which various properties of the EEG time series differ from those during interictal (activity between seizures) and ictal (seizure) periods [3]. Attempts have been made to characterize this preictal period using, among others, the largest Lyapunov exponent [4], correlation density [5], correlation dimension [6,7], and dynamical similarity measures [8–10]. Other recent approaches utilize measures of phase synchrony which determines the degree of phase locking between two oscillatory signals. Although the concept of phase synchronization has long been known [11], it is only recently that it has been applied to nonlinear time series analysis [12] and biological data in the analysis of Parkinson patients [13], the cardiovascular and respiratory systems [14], the calcium oscillations of epileptic cultures of astrocytes [15,16], and in EEG recordings [17–20].

Measures of phase and lag synchronization show a rather unexpected effect: A significant decrease in synchronization between certain EEG channels during the preictal period. The patterning of channels that exhibit this drop is quite complicated and is not necessarily dependent upon spatial structure. It has been hypothesized that this is due to the fact that the spatial and functional structure of the brain do not overlap [19]. Specifically, structures that are far in terms of Euclidian distance may have strong functional links, while neighboring regions may be functionally independent. This leads one to believe that the drop in synchronization occurs in weakly connected, functionally different regions of the brain. Thus while the cause of this decrease is unknown, it has been hypothesized [17,19] that the recordings are performed in separate regions of synchronized activity where one site has become involved in the synchronous activity associated with the epileptic focus and onset of the seizure, while the other site has yet to become enveloped in this activity.

Testing this hypothesis experimentally as well as understanding its dynamical underpinnings is difficult since the EEG records the activity from a population of neurons, and while EEG recordings give important information about neural activity, the recorded signal cannot be directly linked to the underlying dynamics of the brain. We thus turn to a mod-

*sarahfel@umich.edu

eling approach to gain further insight into the possible mechanisms for the increased synchrony observed during interictal periods as well as the drop in synchrony during the preictal period.

We study a computational model in which two coupled networks of integrate-and-fire neurons model separate EEG recording sites. We choose one network to be associated with the seizure generating region (epileptic focus) and slowly drive this pathological network into a bursting (seizing) state by increasing the excitability of the neurons within that network over time. This method of transition into a seizure is chosen to mimic a class of cellular mechanisms thought to lead to a seizure [21]. A model of this type allows for analysis of the levels of synchronization over the total population of the networks (similar to using intracranial EEG) as well as at the level of the individual neurons.

We observe changes within the collective dynamics of the pathological network as the neurons transition from the globally asynchronous firing state which we consider to represent normal neural dynamics into the bursting state of a seizure. If the collective dynamics of the networks share gross dynamical properties (i.e., the same excitability), the networks will enter a resonance state. This leads to an amplification of the intrinsic oscillatory rhythm and increased levels of locking between collective signals of the networks. However, as the network corresponding to the epileptic focus begins its transition into the seizing state (but before the network begins to burst), the networks stop resonating, resulting in an elimination of the oscillatory patterning and a subsequent drop in phase synchrony that marks the beginning of the preictal period. During this time, the neurons of the pathological network continue to fire asynchronously but begin to increasingly lock their frequencies. Once the pathological network reaches the bursting state, it begins to drive the other network into a bursting state and we again see the high levels of synchronization characteristic of the ictal period.

We thus postulate that the preictal period marks the beginning of the transition from normal neural dynamics into bursting dynamics, which is characterized by the steady increase and locking of neuronal frequencies that eventually leads to bursting. This transition in the "focal" network is accompanied by an initial lack of a similar transition in the "normal" network, which causes the divergence of intrinsic network properties and a drop in the phase synchrony between the two networks.

II. METHODS

A. Model

The system studied in the paper consists of two interconnected small-world networks (SWNs) of integrate-and-fire neurons. Each network consists of 225 neurons situated on a two-dimensional (2D) square lattice with a lattice constant of $a=1$ and periodic boundary conditions. Neurons are initially locally connected to neighbors within a radius of $k=2$. The connections are then rewired with a probability of $p=0.3$, consistent with the Watts-Strogatz small-world (SW) model [22]. The small-world architecture has been shown to produce self-sustained activity [23], increase the network's ability to synchronize [24,25], and has previously been used for models of epileptic behavior [26–28].

We introduce connections between the two networks by selecting a fraction $f=0.5$ of the neurons in each network to send synaptic current to randomly chosen m neurons in the other network. Unless stated otherwise, $m=15$. Connecting the networks in this manner causes the neurons in one network to receive, on average, seven random connections from the other network, representing the average activity of that network.

The dynamics of each neuron are governed by

$$\tau_m \frac{dV_i}{dt} = -\alpha_i V_i(t) + \sum_{j\in\delta} J_{ij}(t) + B\sum_{k\in\gamma} J_{ik}(t) + \xi_i(t) + E, \quad (1)$$

where $\tau_m=20$ ms, α_i is the leakage coefficient which is uniformly distributed in $[1,1.1]$, δ represents the intranetwork connections, γ represents the internetwork connections of the ith neuron, and we sum over the incoming synaptic current J. B is the coupling parameter between the networks. For the simulations, we used $B=0.4$ unless otherwise noted. The noise variable for each neuron $\xi_i(t)$ is uniformly distributed in $[0,0.5]$ and E is the excitability parameter which is constant for each neuron in a given network, but is allowed to vary between the networks. The neural excitability determines the amount of synaptic input needed to cause the neuron to fire and acts as a control parameter between the asynchronous firing of neurons within a network and bursting behavior where the population of neurons fires collectively. We use this parameter to induce bursting in one network by slowly raising its value over time, bringing the network from a nonbursting state into a bursting state. The level of excitability at which the network transitions into the bursting state is referred to as the bursting threshold. We will denote the two networks as $N1$ and $N2$ with respective excitability parameters E_1 and E_2.

Equation (1) was integrated using Euler's method and a neuron was said to fire an action potential when the membrane potential V reached a threshold value of 1. At this point, the neuron emits a spike of synaptic current that is sent to the neurons to which it is connected. For this reason we use the term "spike" to refer to the firing of a neuron. The incoming synaptic current to the ith neuron from the jth neuron is given by

$$J_{ij}(t) = A\left[\exp\left(-\frac{t-t_j}{\tau_s}\right) - \exp\left(-\frac{t-t_j}{\tau_f}\right)\right], \quad (2)$$

where t_j denotes the last time at which the jth neuron spiked, $\tau_s=0.2$ ms is the slow time constant, and $\tau_f=0.02$ ms is the fast time constant. These two time constants determine the spike shape and are chosen to approximate a biological action potential [29]. The parameter $A=1.8$ sets the amplitude of the spike. After firing, the membrane potential is reset to 0, and the neuron enters a refractory period of 8 ms under which it does not integrate incoming current. Moreover, when out of the refractory period, a neuron only integrates synaptic current if the total value is above a threshold level of 0.4. Each network has an intranetwork synaptic delay of

0.6 ms and unless stated otherwise, the internetwork delay is 0.8 ms. These two constants define the spatial extent and the distance between the two networks.

For comparison with EEG recordings, we consider here the total current signal of each network which we define to be the sum of all synaptic currents of the neurons within the network at each point in time, as this tells us the collective activity of a population of neurons. We can then look at measures of phase and lag synchrony between the total current signals of our networks while varying their relative properties and compare the results to those obtained from EEG recordings of epileptic patients. Our model also allows us to monitor the firings of the individual neurons within the network and to study how the synchronization of the individual neurons leads to the observed signal. This allows for insight into the mechanisms behind the synchronization of the two networks on the neuronal level which is difficult to obtain from actual EEG recordings.

B. Mean phase coherence

We first examine the mean phase coherence in our system which is a measure of phase synchrony. Phase synchrony refers to the state where the phases of two oscillators become locked while their amplitudes remain uncorrelated [30]. This generally occurs in systems of weakly coupled, nonidentical oscillators. We consider the brain to be an example of such systems, as a first order approximation, since each neuron is different, and the total number of synapses a given neuron has is small compared to the total number of neurons in the brain. The general definition of phase locking in noisy oscillators is

$$\Delta\phi_{1,2} = |k\phi_1 - l\phi_2| \cong \text{const}, \tag{3}$$

where ϕ denotes the phase of the oscillators and k and l are integers (here we use $k=l=1$). The mean phase coherence examines the angular distribution of the difference in phase between two oscillators and is defined [17] as

$$R = \left| \frac{1}{N} \sum_{j=0}^{N-1} e^{i\Delta\phi_{1,2}(j\Delta t)} \right|, \tag{4}$$

where N denotes the number of samples in a discrete time series and $1/\Delta t$ is the sampling rate. This definition restricts $R \in [0,1]$ and phase locking occurs for $R=1$ while $R=0$ implies unsynchronized signals.

To calculate R for our simulations, we used a moving window technique in accordance with [18] with $k=l=1$. The time series of the collective signal was divided into a series of windows composed of 4096 points or 819.2 ms with an overlap of 20%. First, the data in each window were demeaned (the mean value of the signal was subtracted, eliminating any dc component of the signal), and a Hanning window was applied. We then used the Hilbert transform [31] to define the analytic signal and calculate the instantaneous phase of the signal.

The Hilbert transform of a signal $s(t)$ is given by

$$\tilde{s}(t) = \frac{1}{\pi} P.V. \int_{-\infty}^{\infty} \frac{s(\tau)}{t-\tau} d\tau \tag{5}$$

(where P.V. denotes the Cauchy principal value) and the analytic signal is then defined as

$$\zeta(t) = s(t) + i\tilde{s}(t). \tag{6}$$

From this, we can uniquely define the instantaneous phase of our signal as

$$\phi(t) = \arctan\left(\frac{\tilde{s}(t)}{s(t)}\right). \tag{7}$$

Finally, 10% of the signal was discarded at both ends to minimize the edge effects caused by applying the Hilbert transform to a finite signal. The resulting phases were used to calculate the phase difference between signals and the mean phase coherence.

C. Maximum linear cross correlation

We also examine the lag synchronization of the total current signal. Lag synchronization refers to the case when the state variables of two signals are the same but offset by a constant time lag [32]. A measure of lag synchronization between two signals $s_{1,2}(t)$ at a time lag τ is the normalized cross correlation given by

$$\hat{C}(s_1,s_2)(\tau) = \left| \frac{C(s_1,s_2)(\tau)}{\sqrt{C(s_1,s_1)(0)C(s_2,s_2)(0)}} \right|, \tag{8}$$

where C is the linear cross correlation function,

$$C(s_1,s_2)(\tau) = \int_{-\infty}^{\infty} s_1(t+\tau)s_2(t)dt. \tag{9}$$

In order to measure the lag synchronization of our system, we look at the maximum linear cross correlation [18] defined as

$$C_{\max} = \max_{\tau}\{\hat{C}(s_1,s_2)(\tau)\}. \tag{10}$$

As with the case of the mean phase coherence, $C_{\max} \in [0,1]$, and $C_{\max}=1$ implies complete lag synchronization while $C_{\max}=0$ for unsynchronized signals. We use the moving window technique described above to calculate $C_{\max}$ over each window.

III. RESULTS

We observe three different types of behavior in the total current signal of the modeled network as seen in Fig. 1. In an uncoupled system, the network will undergo random firing for low values of E as seen in Fig. 1(a). As the value of E is increased and the mean firing rates of the neurons increase, the network enters an oscillating stage where the total current signal undergoes oscillatory modulation as in Fig. 1(b). When E is increased further, the network reaches the bursting threshold where the neurons begin to fire synchronously, and the network enters the bursting stage of Fig. 1(c).

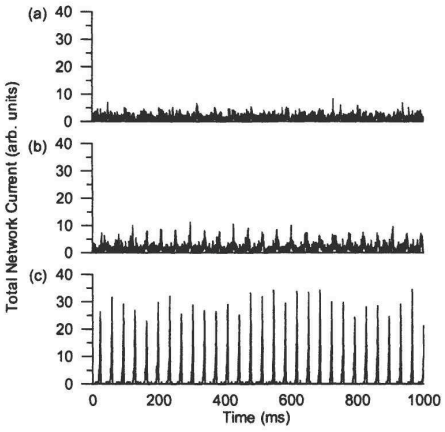

FIG. 1. Examples of the different types of behavior of the collective current trace of a single, uncoupled network. (a) Random firing behavior seen below the bursting threshold, $E=0.85$. (b) Fast oscillatory modulation just before the transition to bursting, $E=0.95$. (c) Bursting behavior observed above the bursting threshold, $E=1.1$.

These results are consistent with the findings of [26], who studied single 1D SWNs and induced bursting behavior by adding additional long range connections to the network while holding the excitability of the neurons constant. Here, we hold the topology constant and induce the transition to bursting by increasing the excitability of the neurons to mimic the transition from interictal to ictal dynamics. It has been shown [33] that slices from the CA3 region of the hippocampus exhibit population bursts when the mean firing rate of the neurons within a driver site is increased above a threshold level. It has been hypothesized that bursting behavior within a neural network is thus the result of the increase in the mean firing rate of the neurons within a given region above some frequency threshold. This is precisely what we observe when increasing the excitability parameter due to the link between the excitability parameter and the firing rate of the neurons. In Fig. 2(a), we show this relationship between the average firing rate of five neurons and the excitability parameter. As we raise the excitability of the network, the neurons begin to fire more rapidly and the network enters a bursting state. As a result, there is also an increase in the mean current output by the network [Fig. 2(b)].

In a coupled network system, the excitability of $N2$ is held constant at $E_2=0.8$, representing a local network which is not a part of the epileptic focus. Conversely, $N1$ represents a local network that is part of the epileptic focus, and we step up the excitability of this network from $E_1=0.75$ to $E_1=1.1$ to obtain the transition to bursting, seizurelike dynamics. In Fig. 3 we show the mean phase coherence R and the maximum linear cross correlation C_{max} plotted as a function of the difference in excitability between the networks, $\Delta E=E_1-E_2$, averaged over 100 simulations. The average values of R and C_{max} were calculated for each simulation by iterating for

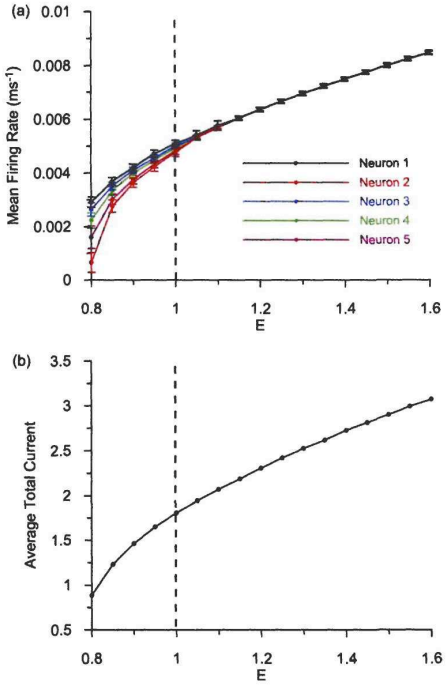

FIG. 2. (Color online) (a) Relationship between the excitability parameter of a single network and the average firing rate of five different neurons within the network. Increasing the excitability of the network causes the neurons to fire more rapidly and to synchronize. (b) The average total current in a single network as a function of the excitability. As the excitability is increased, the total synaptic current in the network will rise. The dotted line denotes the bursting threshold.

10 s at each value of ΔE and disregarding a transient time of 4 s.

We focus on the three dynamical regimes, when: (A) both networks are well below bursting threshold and have the same properties (same excitability, $\Delta E=0$), (B) both networks are below bursting threshold and $\Delta E \neq 0$, and (C) the neural excitability of $N1$ is above the bursting threshold.

For low values of E, below the bursting threshold, when $E_1=E_2$, the total current signal of both networks remains asynchronous but exhibits slow oscillatory modulation as observed in a single network for relatively high network excitability. However, the oscillatory modulation observed here is due to the resonance drive of both networks through the internetwork coupling. We associate this regime with the interictal dynamics observed in the epileptic brain.

When the networks are below the bursting threshold but have significantly different properties such that $E_1 \neq E_2$, even though the total input from $N1$ to $N2$ increases significantly as E_1 is increased, both networks still may exhibit asynchronous dynamics and, furthermore, the slow oscillatory modu-

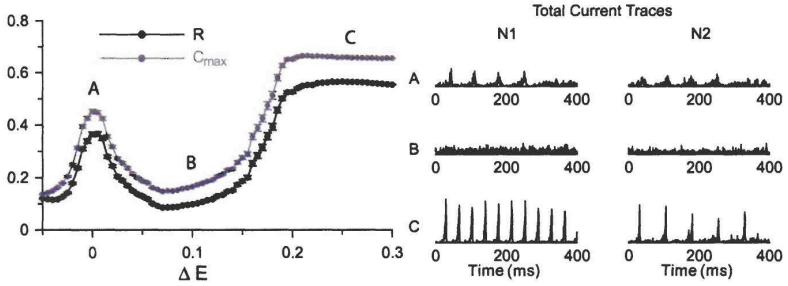

FIG. 3. Plots of the average phase coherence and maximum cross correlation coefficient as a function of the mismatch between the excitability parameters in the networks. Values were averaged over 100 simulations as described in the text. Sample current traces are shown for the different types of behavior seen during the resonance (A), random firing (B), and bursting regimes (C).

lation is abolished. We link this regime to the preictal state.

When $N1$ is above the bursting threshold, the bursting of that network will induce bursting behavior in $N2$. This driving interaction that occurs during the bursting regime represents the spread of bursting behavior throughout different regions of the brain during a seizure (the ictal state).

We thus observe a typical resonance curve centered on $\Delta E=0$ which is where we see the oscillatory behavior of the networks that gives rise to the higher levels of synchronization. As ΔE is further increased, the frequency response of the two networks becomes mismatched, the slow oscillatory modulation is abolished, and there is a drop in the synchronization. The measures of synchronization rise again for large values of ΔE, as this is the region where E_1 crosses the bursting threshold and the networks enter the bursting regime, with $N1$ driving the bursting in $N2$.

We then studied the role of the coupling and delay between the networks on the observable drop of phase synchrony during the preictal period. Figure 4(a) shows the average values of R and C_{max} for $\Delta E=0$ (upper lines) and $\Delta E=0.1$ (lower lines) calculated over 20 simulations in which the coupling parameter B was varied while the number of connections between the networks was held constant at $m=15$. As the coupling in the network increases, the level of synchrony at the resonance increases and for high levels of coupling, the synchrony during the parameter mismatch increases as well. We calculated the differences, $\Delta R=R(\Delta E=0)-R(\Delta E=0.1)$ and $\Delta C_{max}=C_{max}(\Delta E=0)-C_{max}(\Delta E=0.1)$ in Fig. 4(b). The peak in this curve is due to the interplay between the level of synchrony at resonance and the spread in the range of oscillations as the coupling is increased. We see that the difference between the synchrony at resonance

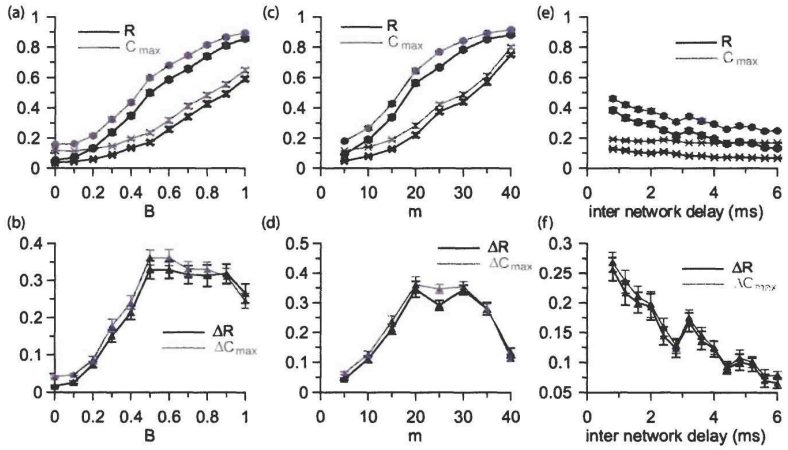

FIG. 4. (a, c, e) Average synchronization as a function of the coupling parameters during two regimes: $\Delta E=0$—upper lines, and $\Delta E=0.1$—lower lines. (b, d, f) Difference between the level of synchronization between the two regimes. (a) and (b) Calculated as a function B, with $m=15$. (c) and (d) Calculated as a function of the number of connections between networks m with $B=0.4$. (e) and (f) Calculated as a function of internetwork synaptic delay with $B=0.4$ and $m=15$ with a constant intranetwork delay of 0.6 ms.

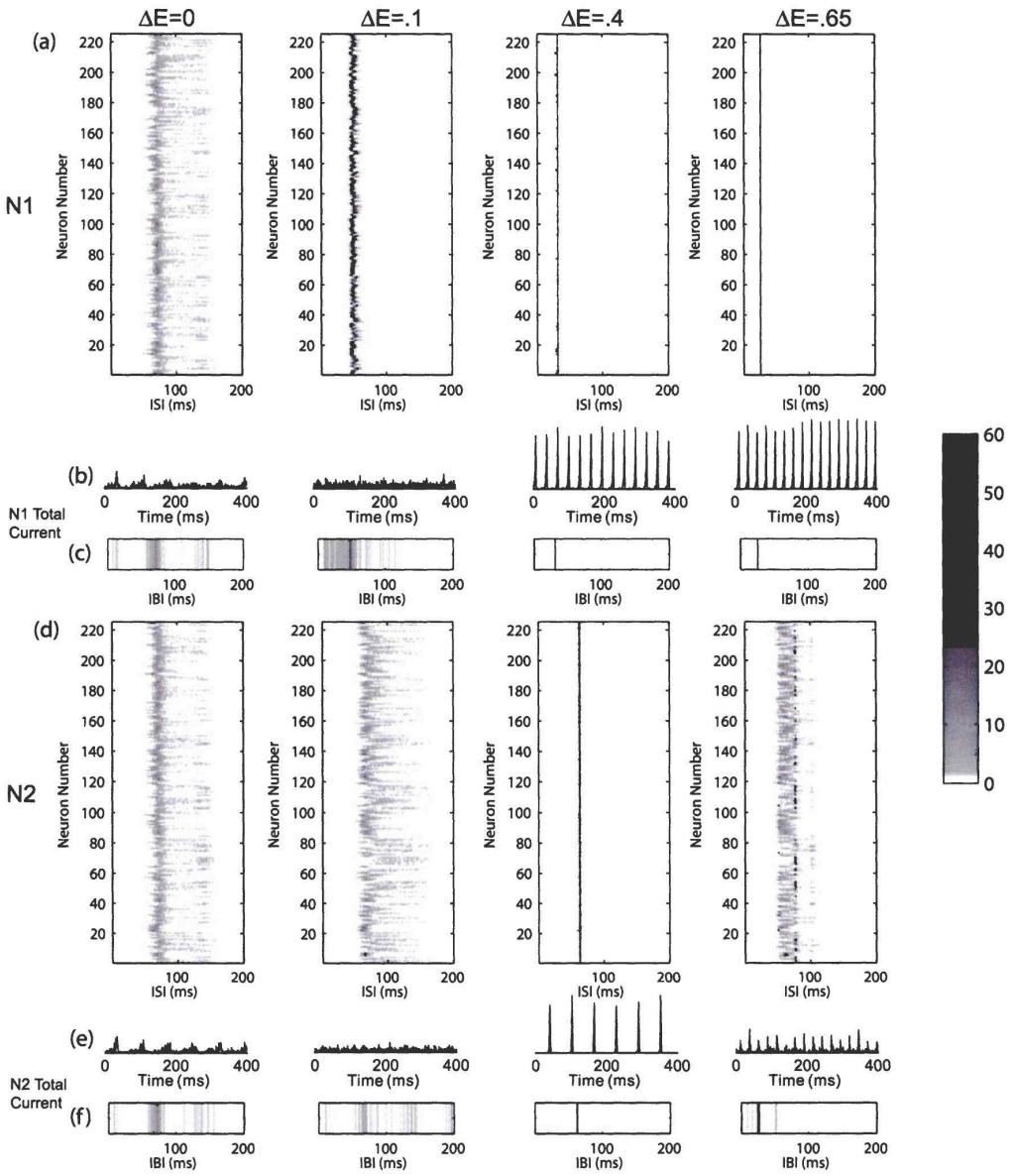

FIG. 5. Panels (a)–(c) show the analysis for *N*1, panels (d)–(f) show the analysis for *N*2. (a) and (d) Interspike interval (ISI) histograms for each neuron shown for four levels of excitability mismatch. (b) and (e) Samples of corresponding collective signals. (c) and (f) Interburst interval (IBI) histograms of the collective signal during the same intervals as in (a) and (c). Histograms were created by running a peak detection program on the collective signal to determine population spikes. Note that the ISI and IBI histograms do not necessarily correspond, indicating that the phase of the neuron plays a large role in the behavior of the network as a whole.

and away from resonance remains high over a large range of coupling parameters. A similar effect was observed when we varied the number of connections m between the networks and kept the internetwork coupling strength constant at $B=0.4$ [Figs. 4(c) and 4(d)]. For large m, we see a decrease in the difference between synchrony levels. This is to be expected since as we add more internetwork connections, we are effectively losing the distinction of having two separate networks. We study the effects of internetwork delays on the observed phenomenon in Figs. 4(e) and 4(f). Here we hold the coupling parameters constant at $B=0.4$ and $m=15$. One can see that as the delay between the networks is increased, there is a decrease in the observed resonance peak. However, the behavior is observed over a significant range of delays indicating that the two interacting networks can be positioned relatively far apart.

In order to better understand the behavior of the networks in terms of the underlying neuronal dynamics, we examined the behavior of the individual neurons within each network. Figures 5(a) and 5(d) show histograms of the interspike intervals (ISIs) of the individual neurons within each network for four different values of ΔE in a system with $B=0.4$ and $m=15$. We also performed a peak detection to detect bursts in the total current signal of each network [Figs. 5(b) and 5(e)] to create histograms of the interburst intervals (IBIs). The peak detection was done by smoothing the signal over a window of 1.8 ms and a burst was said to occur when the smoothed signal increased above a threshold value of 3. These histograms of the networks' collective behavior are shown in Figs. 5(c) and 5(f). A bin size of 1 ms was used to create the histograms.

We first focus on the behavior of the network for values of E_1 below the bursting threshold. For the case of $\Delta E=0$, we see that the ISI histograms of neurons in each network as well as the IBIs of each network have a similar distribution. The networks are operating at the same frequency. We observe slow oscillatory modulation in the total activity of the networks and consequently increased phase synchronization between the networks. When $\Delta E=0.1$, we observe a different type of behavior. Although the individual neurons in $N1$ are firing at an approximately locked rate leading to the narrow ISI distribution, the total current signal of the network shows a broad IBI distribution indicating that the neural activity remains asynchronous, and the total current signal of the network undergoes occasional random, low activity bursts. The neurons in $N2$ show a virtually unchanged, wide distribution of ISI. The distribution of IBI is similar to that observed previously, but the slow oscillatory component in the total activity is no longer observed. Thus the asynchronous dynamics of the first network do not significantly alter the temporal dynamics of the second network. This is due to the fact that the neurons in $N2$ receive a current input from $N1$ which increases, but remains temporally unstructured.

When the value of E_1 is above the bursting threshold we observe different behavior. Both networks start to burst with evolving locking patterns. In the case of $\Delta E=0.4$, the ISI distributions of neurons in both $N1$ and $N2$ are highly peaked and the peaks correspond to those of the IBI distributions in the total activity of their respective networks, indicating that the neural populations within the networks are highly synchronized, and each network is now undergoing coherent bursting behavior. However, the value of ISI and IBI is different as the networks enter a 2:1 locking regime.

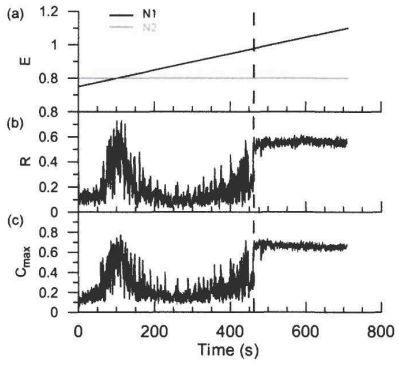

FIG. 6. Measures of synchronization. The vertical dashed line represents the bursting threshold. (a) Excitability parameters as a function of time. N1—black, N2—gray. (b) Phase coherence R as a function of time. (c) Maximum cross correlation coefficient C_{max} as a function of time. High levels of synchronization occur during the region of parameter matching and during bursting behavior, while other regions exhibit low levels of synchronization.

When E_1 is further increased ($\Delta E=0.65$), we observe a transition to another type of behavior. The neurons in $N1$ remain synchronized and the network bursts at a higher frequency due to the increase in the excitability. The neurons in $N2$ become unsynchronized and fire roughly at multiples of the period of the neurons in $N1$. This leads to relatively weaker bursting, as a limited numbers of neurons fire in each cycle, but 1:1 locking can be observed.

Thus even though the frequency of spiking and the average magnitude of the mean-field signal of $N1$ increases monotonically with changes of neuronal excitability, the slow oscillatory patterning in network activity observed when the networks have the same properties is initially abolished before the transition into bursting. This results in the drop of synchrony in the transitional period, before the onset of bursting. We thus hypothesize that the observed preictal drop in phase synchrony of the EEG is due to the abolition of resonant interaction between the two networks caused by changes in the frequency response of network that is associated with seizure generation. Therefore we postulate that the observed drop in synchrony is in fact an early signature of the pathological changes in the dynamics of the focus that eventually lead to seizure-type dynamics.

To demonstrate this transition from normal to pathological dynamics, we hold the excitability of $N2$ constant at $E_2=0.8$ and slowly increase the excitability of $N1$ from $E_1=0.75$ to $E_1=1.1$ as shown in Fig. 6. The progression of the changes in synchrony, driven by incremental changes in excitability of $N1$, mimics those observed in epileptic patients during transitions from interictal to preictal and preictal to ictal states.

In Fig. 7 we show, for comparison, the temporal course of the mean phase coherence R estimated from EEG time series

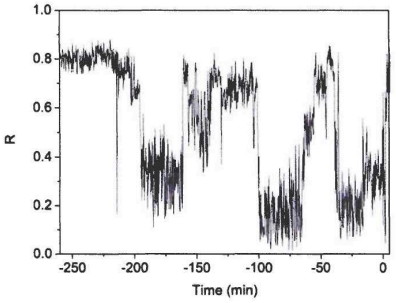

FIG. 7. Profile of the mean phase coherence R for a pair of intrahippocampal EEG recordings from a patient suffering from mesial temporal lobe epilepsy. Seizure onset is at $t=0$.

that were recorded intrahippocampally from a patient suffering from mesial temporal lobe epilepsy during the phase preceding an epileptic seizure. EEG signals were sampled at 260 Hz using a 12 bit analog-to-digital converter and filtered within a frequency band of 0.5–85 Hz. R values were calculated (see Sec. II B) using a moving-window technique with nonoverlapping segments of 15.8 s corresponding to 4096 data points. In contrast to our model simulations, in the experimental setting we do not have access to the actual excitabilities of the network dynamics assessed by the respective EEG recordings. Nevertheless, we might speculate that the time course of R, in general, reflects fluctuations of the excitabilities of the network. Interestingly, during the time frame −100–0 min the course of R and the fact that a seizure occurs is consistent with what we observed in our model when monotonically increasing the excitability of the "focal" network.

Thus here we define the preictal length to be the time it takes for the networks to transition from the resonance state into the bursting state and study the distribution of these lengths over multiple realizations of a given network (i.e., different instances of a network with the same global statistical properties). This can be seen in Fig. 8 for four runs on 12 different network realizations. The start of the preictal period was marked by the point at which the mean phase

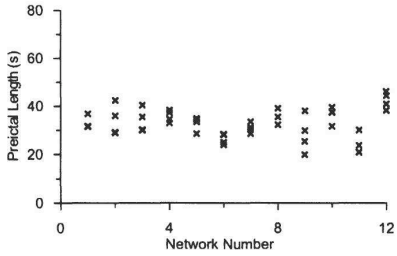

FIG. 8. Calculated preictal lengths for 12 different realizations of a network. Four simulations were run for each network realization and the preictal length was calculated as described in the text.

coherence dropped below one standard deviation of its average value during the resonance state, and the end of the preictal period was defined to be a point at which the networks first entered the bursting state. We see that although each realization displays the transition from resonance to bursting, the time course varies for different realizations. This variance in preictal lengths between patients has also been observed experimentally [18].

IV. DISCUSSION AND CONCLUSIONS

We have used a simple toy model of coupled networks to investigate the dynamical underpinnings of the drop in phase synchronization that is observed in epilepsy patients before a seizure. The observed regimes of high synchronization are the result of two types of interacting dynamics: a resonance interaction between the two networks when their properties are similar, and directional driving when the network associated with the focus drives the bursting in the other network.

We equate this resonance interaction between our networks to the normal dynamics of the brain during the interictal period and the directional driving to the propagation of the seizure during the ictal period. In between these two dynamical regions, we have an intermediate state which we equate to the preictal period where the dynamical properties of the interacting networks are mismatched, and the resonance interaction is abolished, while the directionally driven bursting is not yet present. While during both the resonance state and the driving state we see high levels of synchronization between the networks due to their similar dynamical properties, it is the mismatch of properties during the intermediate preictal state that leads to the observed decrease in the phase synchrony between the two networks.

We therefore compare the transition out of the resonance state and into the bursting state to the transition from normal neuronal dynamics to the pathological dynamics of a seizure. This implies that the observed drop in phase synchrony between certain EEG channels that defines the preictal period could be a result of the initial biological changes in the neurons associated with the focus and generation of the seizure that occur long before the system actually reaches the seizing state.

For this transition scenario to happen one has to assume that in the interictal period the focal and normal networks in the brain have similar gross dynamic properties so that they enter the oscillatory resonant state. There is experimental evidence from phase synchronization measures that interictal synchronization is high between electrodes placed within the same structure of the brain [17]. Such interactions are also observed between the focus and other brain regions during the interictal period [34]. Furthermore, it has become an accepted view in neuroscience that "the perpetual interactions among the multiple network oscillators keep cortical systems in a highly sensitive 'metastable' state and provide energy-efficient synchronizing mechanisms via weak links" [35].

Although we have used a very simple model to explore a possible explanation for the underlying dynamics governing

different areas of the brain before a seizure, our model shows the same behavior as observed in EEG recordings and has allowed us to make valuable insights at the neuronal level which cannot be done through the analysis of EEG recordings. We conclude that it is possible that the observed preictal period is a manifestation of initial biological neuronal changes that begin before the start of seizing behavior and encourage further experimental work to explore this hypothesis.

ACKNOWLEDGMENTS

S.F. was funded through the National Science Foundation. H.O. and K.L. acknowledge support from the Deutsche Forschungsgemeinschaft (Grant No. SFB-TR3 sub-project A2). F.M. acknowledges support from the European Community (6th Framework Programme, Marie Curie OIF 040445). M.Z. acknowledges support from NIBIB at NIH (Grant No. EB003583).

[1] F. Mormann, R. G. Andrzejak, C. E. Elger, and K. Lehnertz, Brain **130**, 314 (2007).
[2] J. Engel, *Surgical Treatment of Epilepsies* (Raven Press, New York, 1987).
[3] F. Mormann, T. Kreuz, C. Rieke, R. G. Andrzejak, A. Kraskov, P. David, C. E. Elger, and K. Lehnertz, Clin. Neurophysiol. **116**, 569 (2005).
[4] L. D. Iasemidis, J. C. Sackellares, H. P. Zaveri, and W. J. Williams, Brain Topogr. **2**, 187 (1990).
[5] J. Martinerie, C. Adam, M. Le Van Quyen, M. Baulac, S. Clemenceau, B. Renault, and F. J. Varela, Nat. Med. **4**, 1173 (1998).
[6] K. Lehnertz and C. E. Elger, Electroencephalogr. Clin. Neurophysiol. **95**, 108 (1995).
[7] C. E. Elger and K. Lehnertz, Eur. J. Neurosci. **10**, 786 (1998).
[8] M. Le Van Quyen, J. Martinerie, M. Baulac, and F. Varela, Neuroreport **10**, 2149 (1999).
[9] M. Le Van Quyen, J. Martinerie, V. Navarro, P. Boon, M. D'Have, C. Adam, B. Renault, F. Varela, and M. Baulac, Lancet **357**, 183 (2001).
[10] V. Navarro, J. Martinerie, M. Le Van Quyen, S. Clemenceau, C. Adam, M. Baulac, and F. Varela, Brain **125**, 640 (2002).
[11] C. Huygens, *Horologium Oscillatorum* (Apud F. Muget, Paris, 1673).
[12] M. G. Rosenblum, A. S. Pikovsky, and J. Kurths, Phys. Rev. Lett. **76**, 1804 (1996).
[13] P. Tass, M. G. Rosenblum, J. Weule, J. Kurths, A. Pikovsky, J. Volkmann, A. Schnitzler, and H. J. Freund, Phys. Rev. Lett. **81**, 3291 (1998).
[14] C. Schafer, M. G. Rosenblum, J. Kurths, and H. H. Abel, Nature (London) **392**, 239 (1998).
[15] G. Balazsi, A. Cornell-Bell, A. B. Neiman, and F. Moss, Phys. Rev. E **64**, 041912 (2001).
[16] G. Balazsi, A. H. Cornell-Bell, and F. Moss, Chaos **13**, 515 (2003).
[17] F. Mormann, K. Lehnertz, P. David, and C. E. Elger, Physica D **144**, 358 (2000).
[18] F. Mormann, R. G. Andrzejak, T. Kreuz, C. Rieke, P. David, C. E. Elger, and K. Lehnertz, Phys. Rev. E **67**, 021912 (2003).
[19] F. Mormann, T. Kreuz, R. G. Andrzejak, P. David, K. Lehnertz, and C. E. Elger, Epilepsy Res. **53**, 173 (2003).
[20] M. Le Van Quyen, J. Soss, V. Navarro, R. Robertson, M. Chavez, M. Baulac, and J. Martinerie, Clin. Neurophysiol. **116**, 559 (2005).
[21] J. A. Gorter, E. A. van Vliet, E. Aronica, and F. H. Lopes da Silva, Hippocampus **12**, 311 (2002).
[22] D. J. Watts and S. H. Strogatz, Nature (London) **393**, 440 (1998).
[23] A. Roxin, H. Riecke, and S. A. Solla, Phys. Rev. Lett. **92**, 198101 (2004).
[24] T. Nishikawa, A. E. Motter, Y. C. Lai, and F. C. Hoppensteadt, Phys. Rev. Lett. **91**, 014101 (2003).
[25] M. Barahona and L. M. Pecora, Phys. Rev. Lett. **89**, 054101 (2002).
[26] T. I. Netoff, R. Clewley, S. Arno, T. Keck, and J. A. White, J. Neurosci. **24**, 8075 (2004).
[27] B. Percha, R. Dzakpasu, M. Zochowski, and J. Parent, Phys. Rev. E **72**, 031909 (2005).
[28] B. H. Singer, M. Derchansky, P. L. Carlen, and M. Zochowski, Phys. Rev. E **73**, 021910 (2006).
[29] W. Gerstner and W. Kistler, *Spiking Neuron Models: Single Neurons, Populations, Plasticity* (Cambridge University Press, Cambridge, England, 2002).
[30] A. Pikovsky, M. Rosenblum, and J. Kurths, *Synchronization: A Universal Concept in Nonlinear Sciences, Cambridge Nonlinear Science Series* (University Press, Cambridge, England, 2001), Vol. 12.
[31] M. Rosenblum and J. Kurths, in *Nonlinear Analysis of Physiological Data*, edited by H. Kantz, J. Kurths, and G. Mayer-Kress (Springer, Berlin, 1998), pp. 91–99.
[32] M. G. Rosenblum, A. S. Pikovsky, and J. Kurths, Phys. Rev. Lett. **78**, 4193 (1997).
[33] L. M. de la Prida, G. Huberfeld, I. Cohen, and R. Miles, Neuron **49**, 131 (2006).
[34] M. Le Van Quyen, J. Martinerie, C. Adam, and F. Varela, Physica D **127**, 250 (1999).
[35] G. Buzsaki, *Rhythms of the Brain* (Oxford University Press, New York, 2006).